The Atomic Structure of the Clean and Adsorbate Covered Ir(110) Surface

Dissertation
zur Erlangung des Grades eines
Doktors der Naturwissenschaften

von
Jens Kuntze

vorgelegt dem
Fachbereich Physik
der Universität Osnabrück

Oktober 1999

Contents

List of Figures

1 Introduction

1.1 General Remarks

Without going into details, it is evident that surface phenomena are of ever increasing importance in today's technical applications, just by looking at the miniaturization in the semiconductor electronic's industry or at the wide field of heterogeneous catalysis. With regard to automotive exhaust control, or the reduction of environmental pollution in large-scale fabrication of chemicals in general, the necessity of designing surface chemical reactions in a suitable way has become obvious during the last decade, and catchwords like the green-house effect have drawn the public's attention to these topics. Besides these practical (and urgent) considerations, lots of questions are still at the level of fundamental or basic research, and the detailed processes occuring on a catalyst surface are often unknown. Even so apparently simple questions as the structure of clean single crystal surfaces are by no means completely answered, yet. Regarding the complexity of catalytic processes used in the chemical industry, science is still at the very beginning of understanding the elementary steps of such reactions. Some of the complications are that industrial catalytic reactions are run under sometimes high pressures and temperatures, and the catalyst usually is in the form of dispersed polycrystalline particles on a support of some other material. Experiments in surface science are, however, usually carried out under very low pressures ($\leq 10^{-7}$ mbar) and on well defined single crystal surfaces with virtually no impurities and an as high as possible structural perfection. Despite these so-called pressure and material gaps, much can be learned from the 'idealized' experiments, since they provide the only way to disentangle the elementary steps in the sometimes very complex reactions. As shown by a recent example [1], a 'surface science approach' can result in improved catalysts.

Going from the simplest system towards growing complexity, studies on model catalysts often start out with the structure of the clean catalysator surface under ultra-high vacuum conditions, and monitor possible changes of this structure during the adsorption of reactants. Using low-index single crystal surfaces is the simplest starting point, since such surfaces can be prepared with a high degree of perfection, both in terms of geometric structure (steps, kinks, vacancies) and chemical purity (typical contaminations are ≤ 0.01 ML; ML = monolayer, the number of atoms per surface unit cell of the unreconstructed surface). Since it is known that adsorption and reaction phenomena often start at steps and kinks, the next degree of complexity may be explored by using vicinal or stepped surfaces instead of flat ones. Giving up chemical purity adds another degree of freedom, which may be in the form of bimetallic catalysts, the presence of other adsorbed species which may promote or poison a given reaction, and of course the coadsorption of the two (or more) possible reactants itself. Studying adsorption, coadsorption, and reactions under more realistic pressure conditions (atmospheric pressure or above) and finally using polycrystalline catalysts, possibly dispersed on a high-surface area support, define the last steps towards industrial conditions.

1.2 Aim and Scope of the Present Work

In this work, the clean surface structure, adsorbate overlayers and adsorbate induced reconstructions and deconstructions, and finally coadsorption phenomena are studied on the (110) surface of iridium. Ir(110) was chosen because the structure of the clean surface has been under debate for a long time, and experimental data are still scarce. Furthermore, iridium is used as a catalyst for several chemical reactions, among them the oxidation of CO [2, 3, 4] (for a review of catalytic reactions on Ir surfaces, see [5]). The structure of the clean surface is addressed in chapter 6.

After the characterization of the Ir(110) reconstruction, it is interesting to explore possible adsorption induced changes in the substrate configuration and the structure of the corresponding adsorbate layers. This is demonstrated by two examples, the adsorption of oxygen and sulfur. The dissociative chemisorption of O_2 is a fundamental step in several catalytic oxidation reactions, and has to date not been investigated by scanning tunneling microscopy (STM) on Ir(110). The experiments concerning oxygen adsorption can be found in chapter 7.

Sulfur was chosen as a second adsorbate, since it is a well known catalytic poison [6], and its adsorption on iridium surfaces was not previously analyzed in great detail. Especially for sulfur on Ir(110), the overlayer structure at saturation coverage has to date not been investigated at all, and for subsaturation coverages only one quantitative study by low-energy electron (LEED) analysis exists [7]. The results concerning the Ir(110)-S system are summarized in chapter 8.

Knowing the structures of the pure adsorbate layers of oxygen and sulfur, the coadsorption of both elements is naturally the next step. Coadsorption experiments of O and S on iridium surfaces are not reported in the literature, and so it is interesting to study the interactions on the atomic scale by STM. Since sulfur oxidation is reported for other metal surfaces, it should be investigated if a similar reaction also occurs on Ir(110). The coadsorption experiments are detailed in chapter 9.

For each system, a short summary of previous experimental work concerning the Ir(110) surface is given in a first section of the respective chapter. In the subsequent sections, the results of the present work are reported and discussed. A comprehensive summary is given at the end of this thesis (chapter 10). The thesis starts out with an outline of the general experimental setup and standard sample preparation techniques (chapter 2), and the following chapters describe the experimental methods used in this work.

2 Experimental Setup

In this chapter, the general setup of the system used in this work will be briefly described. A description of the principal theoretical background and some experimental details of each method will be described in the following chapters. A brief account on standard sample preparation procedures will be given in some depth at the end of this chapter, mainly as a practical guide for experimentalists who are new to these methods.

2.1 The UHV System

The experiments were performed in an Omicron standard ultra-high vacuum (UHV) system [8] with a base pressure in the 10^{-11} mbar range. UHV is needed to ensure a clean or controlled sample surface during the experiments, and some of the applied techniques require UHV for operation.

The system consists of three separate chambers (fast-entry, preparation, and analysis chamber), sealed from each other by full metal gate valves, in which sample preparation and investigation is carried out. A photograph and schematical representation of the system is given in Fig. 2.1. Vacuum is generated by two turbomolecular pumps, combined with two roughing pumps, two ion-getter pumps and two titanium sublimation pumps. The sample is usually prepared in the preparation chamber by standard methods, i.e., sputtering and annealing (see below). After preparation, the sample is transferred to the analysis chamber for investigation with the several available techniques. The system affords a scanning tunneling microscope (STM, see section 3), low-energy electron diffraction (LEED, see section 4), and Auger-electron spectroscopy (AES, see section 5) as standard tools. With the electron-gun used for AES, it is also possible to acquire RHEED (reflection of high-energy electrons and diffraction) pattern on the LEED screen, and a quadrupole mass spectrometer (QUAD) can be used for residual gas analysis (leak testing) or to check the purity of adsorbate gases. For a detailed description of the UHV system and the connected pumps the interested reader may refer to one of the earlier theses [9, 10, 11], or to one of the corresponding manuals [8, 12, 13, 14, 15].

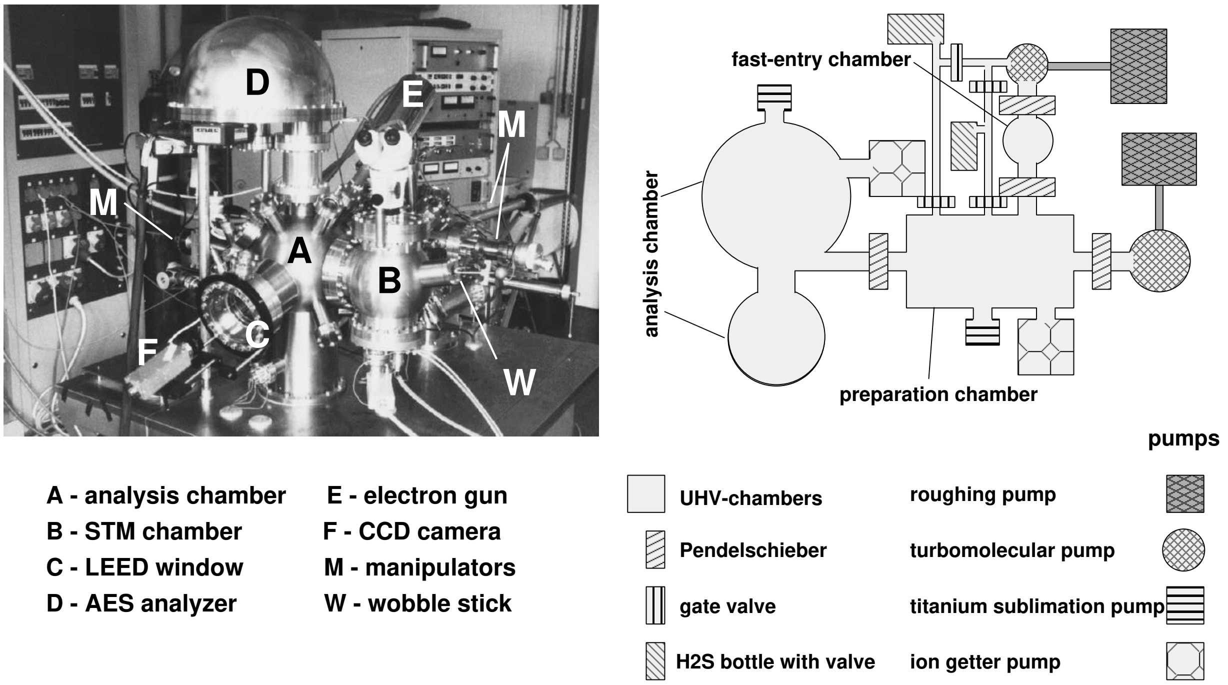

(a) (b)

Figure 2.1: Photo (a) and schematic drawing (b) of the UHV system. The preparation and fast-entry chambers are hidden behind the STM chamber in (a). The ion getter pumps are situated under the mounting platform. In (b) also the H_2S gas inlet is depicted.

2.2 Sample Preparation

The samples are usually cleaned by standard methods as sputter etching with 500 eV Ar^+ ions (sample current approx. $0.5\mu A/cm^2$) and subsequent annealing to remove the sputter damage and desorb implanted Ar. Repeated sputter-anneal cycles are performed until the sample is clean in AES and exhibits sharp LEED beams. For a new sample the initial cleaning procedure may take several weeks up to months, depending on the level of bulk impurities and on the affinity to oxidation. Once the sample is clean, a short sputter-anneal treatment before each measurement (or once per day) is sufficient to obtain good results. Under UHV conditions the sample stays clean for several hours, if is not too reactive (like, for example, Fe and Al, which contaminate more easily).

Traces of residual carbon contaminations may be removed by annealing the sample at approx. 600 K in an O_2-atmosphere of 10^{-8}–10^{-6} mbar for several minutes. Prolonged oxygen treatments at high temperatures should be avoided if possible, since oxygen is known to enhance the segregation of bulk impurities like silicon [16, 17].

For the same reason, avoiding segregation, the annealing times should be kept as short as possible and the temperatures as low as possible. An estimate is one third of the melting temperature (in K). At this temperature, surface diffusion is usually sufficiently large to allow the smoothing of a surface, while bulk diffusion can still be considered as slow.

The final stages of the preparation can only be judged by the quality of the STM image, i.e. whether or not there are disordered clusters or protrusions that apparently do not correspond to the bulk material (although STM cannot directly reveal the chemical nature of the imaged atoms), since the sensitivity limit for AES is at approx. 1 at %, which may still be regarded as insufficient for STM. Furthermore the impurity AES signals may overlap with substrate peaks so that it is not always easy to judge cleanliness from AES alone (this problem has been demonstrated in detail for the case of impurities on Pt [18]). Also a sharp LEED pattern does not imply that the surface is clean, since some impurities may induce reconstructions or form overlayer structures which can give nice pattern that are not typical for the clean surface. A sharp pattern only reveals that the domains are sufficiently large and well ordered, whatever their nature may be. But usually it is clear from other experiments what LEED pattern is to be expected, and an overlayer structure or reconstruction due to impurities can easily be recognized. Strictly speaking, only the combination of all methods allows to determine the surface cleanliness, i.e. if the surface is clean in the AES, shows a sharp LEED pattern typical for the clean surface, and exhibits large terraces in the STM with no 'suspicious' clusters or protrusions.

If possible bulk impurities segregate to the surface at elevated temperatures, it may be helpful to sputter the sample during annealing. This can also be used to obtain larger terraces, since the enhanced surface diffusion at sufficiently high temperatures leads to a layer-by-layer removal rather than the formation of threedimensional voids, which is the usual situation for room-temperature sputtering. The dependency of the sputter damage on temperature has been demonstrated in the experiments of Michely and Comsa [19].

For sputtering, usually cycles of a few minutes are sufficient if only surface impurities should be removed, provided that the current density of the ion flux is sufficiently high (of the order of some hundred nA/cm^2). The time t needed for the removal of one monolayer can be estimated via the following equation:

$$t = \frac{ne}{S j_p} \tag{2.1}$$

where n is the number density of target atoms per m^2 in the monolayer, e the electron charge, S the sputter yield (number of sputtered target atoms per ion), and j_p the primary ion current density. An important variable is of course the sputter yield S, which is a function of the ion energy, the masses and atomic numbers of ion and target, the surface binding energy, the atomic density of the target, the angle of incidence of the sputtering ions and even the charge state of the projectile [20]. This quantity can vary over several orders of magnitude and to determine the optimal sputter parameters it is best to refer to tabulated values. With Au atoms, for example, the sputter yield for 500 eV Ar^+ ions at normal incidence is 1.38 [21], and so a close-packed Au(111) monolayer ($n = 2.8 \times 10^{19}\mathrm{m}^{-2}$) is eroded in about 10 minutes for a current density of 0.5 μA/cm^2. Lighter elements, e.g. impurities like S, C or O, are removed at an even faster rate, so that 15–20 minutes of sputtering time should generally suffice if no thick adsorbed layers have to be removed. Longer sputter times just lead to a rougher surface that must be smoothed by subsequent annealing, hence short and frequent sputter/anneal cycles are to be preferred for cleaning the sample. For further reading, sample cleaning procedures are reviewed in [22].

2.2.1 Gas Adsorption

The influence of adsorbates on the surface structure is one of the main concerns of this work (chapter 8,7,9). All adsorbates are deposited from gas phase simply by admitting the gases to the preparation chamber via a leak valve (backfilling). The total pressure during gas adsorption was usually in the 10^{-8} mbar range, depending on the desired exposure. If surface changes during the adsorption should be monitored in situ, the gate valve between the preparation and the analysis chamber was opened and the gases were admitted to the analysis chamber. This was not done for the very corrosive H_2S gas, however, which was only admitted to the preparation chamber. The adsorbate gases were of research purity (Messer-Griesheim: 99.998 vol % for O_2, 98 vol % for H_2S). The H_2S was admitted via a separate gas line that was only used for this purpose, whereas the other gases were admitted through the line connected to the sputter gun. All lines were immediately pumped out after the adsorption to avoid corrosion. This is especially important for the H_2S gas, which requires special caution because of its toxicity. Thorough ventilation of the lab has to be assured when working with this gas, and a second experimentalist should be present in case of an accident (this, of course, should be obeyed in all experimental work). The H_2S line must be cleaned by flooding the line with N_2 gas at higher pressure (2.5 bar) several times before pumping out, in order to remove all traces of H_2S. The detailed procedure is described in [11].

3 Scanning Tunneling Microscopy (STM)

3.1 The Basic Principle of the STM

The basic principle of the STM is very simple: A small voltage (few mV to several V) is applied between a sharp tip and a metal or semiconductor surface, and if the distance between the tip and the surface is sufficiently small (typically several Å), electrons can tunnel between the two electrodes resulting in a current of a few nA, as is schematically depicted in Fig. 3.1. This can be roughly described by the tunneling of a plane wave (or a wavepacket, to be more exact) through a finite potential barrier, as it is treated in all elementary textbooks on quantum mechanics, e.g. [23]. The important point is that the transmission probability for such a barrier, and thus the tunneling current, decays exponentially with the width of the barrier, i.e. the tunneling gap or tip-sample distance. One finds

$$I \propto e^{-2\kappa z}; \qquad \kappa = \frac{\sqrt{2m_e(V_0 - E)}}{\hbar}, \tag{3.1}$$

where I is the tunneling current, m_e and E are the the mass and energy of the tunneling electron, respectively, V_0 is the height of the barrier and z its width. If one assumes for $V_0 - E$ the workfunction for a typical metal (5 eV), then a change in the tip-sample separation of only one Å results in a change of the tunneling current by one order of magnitude. It is clear that this current can be used as an extremely sensitive measure for the tip-sample distance. If the tip can be moved by a piezo scanner in all three dimensions, a "map" of the surface can be obtained by scanning the tip over the sample while adjusting the height by means of a feedback loop so that the tunneling current is held constant. In this so-called Constant Current Mode (CCM) a greyscale image can then be processed by a computer that represents the voltages applied to the piezos at each given point over the scanned region. As a first-order approximation, this map of piezo voltages can, if properly calibrated, be regarded as a topographical image of the surface. Of course there are many exceptions where this assumption is not strictly valid, but as a general rule this can be applied to all metal surfaces. A typical exception would be the presence of several chemical species on the surface with different local workfunctions. The changes in workfunction would cause a height-adjustment of the tip over the respective regions and thus give the impression of topographical changes, when in reality the observed contrast is of chemical (or electronic) origin.

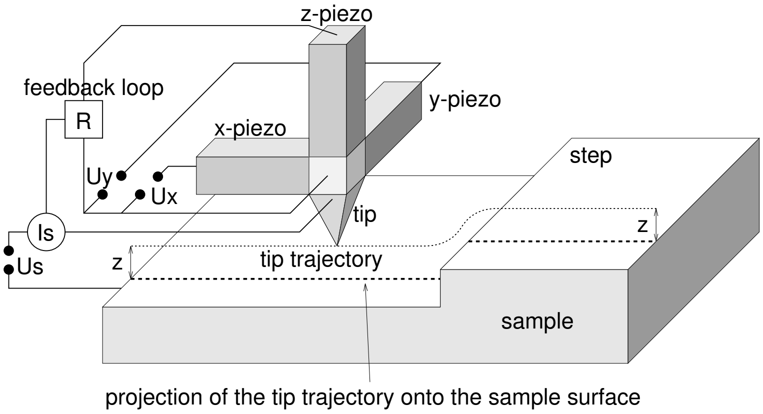

Figure 3.1: Basic STM setup. A tip is moved over the surface by a piezo scanner while a feedback loop adjusts the voltages for the z-piezo in order to keep the tunnel current constant.

It is immediately apparent that the movement of the tip has to be controlled on the sub-Å scale which calls for a very effective vibrational damping. In fact the difficulties in realizing such a setup where considered to be so large that Binnig and Rohrer were told what they were trying should "not have worked in principle" [24]. Nowadays commercially available STMs use eddy-current damping of the STM-platform (see Fig. 3.4) or just rely on a very small and compact design with high mechanical resonance frequencies with no further vibrational isolation except a rubber support.

Another major challenge is the coarse approach of the sample towards the tip, i.e. bringing it from a millimeter to a few Å distance without "crashing" the tip into the surface. But also this and all the other technical difficulties have been overcome and the design of a modern STM is now comparatively simple when looking at the first versions of Binnig and Rohrer [25]. For a review of the technical details concerning STM operation and also theoretical aspects and examples of studied systems the reader may refer to one of the several books dealing with these topics [26, 27, 28].

3.2 STM Theory

To model the tunneling process properly, one needs a correct description of the potential in the tunnel-gap region as well as the correct electronic states of both the sample and the tip and the wavefunction of the tunneling electrons in the region of the gap. In practical situations, at least the tip configuration is usually unknown and the stated problem cannot be solved. Furthermore there may be strong interactions between the tip and the sample and therefore the problem can then not be described by a perturbative theory. However, under the condition of small tunneling currents and voltages it is applicable, which has been done in the approach by Tersoff and Hamann [29, 30]. They used the 'perturbativetransfer Hamiltonian' formalism by BARDEEN [31] in which the interaction between the two tunneling electrodes can be neglected and the tunnel current is described as follows:

$$I = \frac{2\pi e}{\hbar} \sum_{\mu,\nu} \{f(E_\mu)[1 - f(E_\nu)] - f(E_\mu)[1 - f(E_\mu)]\} |M_{\mu\nu}|^2 \delta(E_\nu + V_t - E_\mu) \qquad (3.2)$$

Here $|M_{\mu\nu}|$ is the tunnel matrix element between the two Eigenstates Ψ_{mu}, Ψ_ν of the tip and the sample, respectively, and E_μ, E_ν are the corresponding Eigenenergies. The applied voltage is V_t. The delta function ensures energy conversion or elastic tunneling, and $f(E)$ is the Fermi-Dirac function. For sufficiently low temperatures (room temperature or below) and small tunneling voltages (a few mV) equation 3.2 can be further simplified to

$$I = \frac{2\pi e^2 V_t}{\hbar} \sum_{\mu,\nu} |M_{\mu\nu}|^2 \delta(E_\nu - E_F) \delta(E_{mu} - E_F). \qquad (3.3)$$

The tunnel matrix element is given by:

$$M_{\mu\nu} = \frac{\hbar^2}{2m} \int d\mathbf{S} \bullet (\Psi_\mu^* \nabla \Psi_\nu - \Psi_\nu \nabla \Psi_\mu^*), \qquad (3.4)$$

where m is the electron mass and the integral is over any surface which lies entirely within the barrier region. For a spherical tip with radius R the tip wave functions can be described by s-waves, and one yields

$$I \propto \sum_\nu |\Psi_\nu(\mathbf{r_t})|^2 \delta(E_\mu - E_F) \equiv \rho(\mathbf{r_t}, E_F). \qquad (3.5)$$

Here $\mathbf{r_t}$ represents the position of the tip origin, and $\rho(\mathbf{r_t}, E_F)$ is the local density of states (LDOS) at the Fermi level evaluated at this position. Within the Tersoff-Hamann model an STM image acquired in the constant-current mode can be interpreted as a contour map of constant LDOS at E_F of the surface, and thus represents only sample properties. On metal surfaces the charge distribution at the Fermi level can further be approximated by the total charge density [32], and therefore contours of constant LDOS at E_F resemble contours of constant total DOS, which is topography [28]. However, for semiconductors or non-metallic adsorbates on metal surfaces the contours of constant LDOS at the Fermi level can differ significantly from the total charge distribution, and an interpretation of STM images as topographic maps is in those cases not appropriate. The imaging of adsorbates will be described in more detail in section 3.3.

It must be noted that the Tersoff-Hamann approach does not explain the atomic corrugations observed on clean metal surfaces. Due to the delocalized nature of the electrons, the expected corrugations in the LDOS at E_F are very small, of the order of some pm only. Already at a distance of only 3 Å above the surface, which is even smaller than the usual gap-widths used in STM, no measurable corrugation in the total charge density was predicted by theory [33]. However, STM can achieve atomic resolution on such surfaces, and furthermore the observed corrugations can be quite high, e.g. 0.5–0.8 Å for Al(111)

[34]. The corrugations can therefore not be caused by the variation of the LDOS alone, but must be due to some kind of tip-sample interaction which is not taken into account in the Tersoff-Hamman scheme. The influence of such tip-sample interactions at low gap resistances of ≈ 1 MΩ or less has been demonstrated by CLARKE *et al.* [35], who found a deviation from the exponential relationship between corrugation and tip-sample separation (or gap resistance). At low gap resistances, the corrugation reached a plateau and even fell slightly for very close tip-sample approach. A rising corrugation would be expected instead. The authors could explain the deviation by adhesive forces between the atom at the tip apex and the surface, which lead to a movement of the apex atom during scanning, lowering the observed corrugation. In a sense, only the apex atom adjusts itself instead of a displacement of the whole tip.

There are more elaborate theories of STM, e.g. CHEN has taken into account the influence of additional tip states [36, 37] and TSUKADA and co-workers have studied the effect of the geometric and electronic structure of the tip on STM images [38, 39, 40]. Scattering approaches have been developed by DOYEN and co-workers [41, 42] and SAUTET *et al.* [43, 44] to account for tip-sample interactions. For these further aspects of STM theory the reader may refer to [27].

3.2.1 Scanning Tunneling Spectroscopy - STS

According to the different parameters V_t, I, and z there exist three differnt combinations where always one parameter is kept fixed, namely

$$I(V_t)_{z=const}, I(z)_{V_t=const}, \text{ and } V_t(z)_{I=const} \tag{3.6}$$

As can be seen from equation 3.1, $I(z)$ or $U(z)$ spectroscopy gives the apparent barrier height $V_0 - E = \bar{\Phi}$:

$$\bar{\Phi} = \frac{\hbar^2}{8m_e}\left(\frac{\Delta ln(I/I_0)}{\Delta z}\right)^2 = \frac{\hbar^2}{8m_e}\left(\frac{\Delta ln(V/V_0)}{\Delta z}\right)^2 \tag{3.7}$$

The apparent barrier height is usually smaller than the work function of the substrate due to image potential effects of the tip [26], and can even be near zero at very small gap widths [45]. Nevertheless it can give a good relative measure for the change in (local) workfunction, e.g., for partly adsorbate covered surfaces.

By varying the tunneling voltage and measuring the current $I(V_t)$ while keeping the distance z fixed by deactivating the feedback loop for a certain time, it is in principle possible to gain information about the electronic structure of the surface. As is depicted in Fig. 3.2, tunneling is allowed in an energy window $\Delta E = \mathrm{e} \times V_t$, and by varying the voltage this window can be "sweeped" along the DOS of tip and sample. On the left side of Fig. 3.2 the situation belongs to tunneling from the filled states of the sample into the empty states of the tip, which is the case for negative bias voltages (with the tip grounded, as is the case in the present study). For positive bias voltages, the electrons tunnel from the tip to the sample, and the unoccupied states of the latter are probed. The length of the arrows indicates that the highest lying states always contribute strongest to the tunneling current, which is due to the energy dependence of the tunneling probability [46, 47, 28]. This makes spectroscopy of adsorbed atoms difficult, since their states usually lie well below E_F [47].

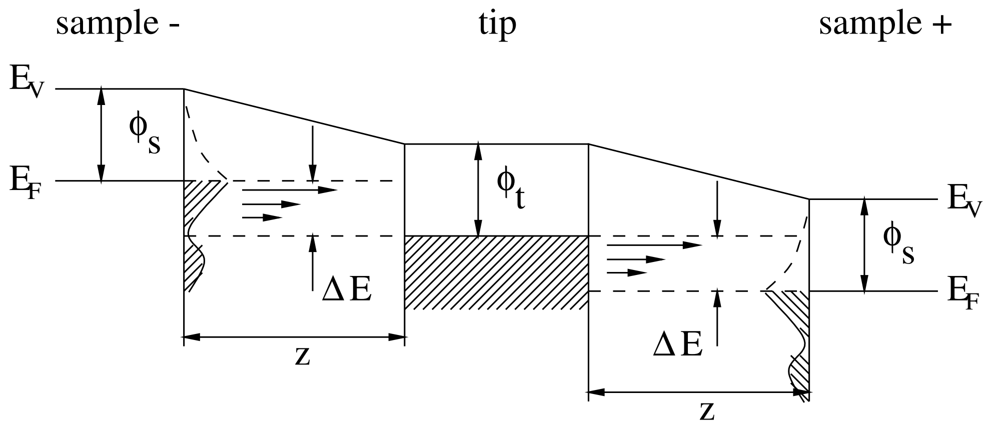

Figure 3.2: Schematical representation of the tunneling between two metal electrodes. The left (right) junction corresponds to negative (positive) bias voltages [tunneling into the tip (sample)]. Only electronic states in the energy window ΔE can contribute to the tunneling current. The arrows indicate that the states near the top of ΔE contribute strongest, since they feel the lowest barrier height. Φ_s, Φ_t: work function of sample and tip, respectively. E_F: Fermi level, E_V: Vacuum level, z: gap width. After [47].

To extract the electronic structure out of such $I(V)$ curves is not straightforward, since usually electronic states of both the tip and the sample give rise to features in these curves [32, 47]. If the electronic structure of the tip is unknown, which is usually the case in real experiments, an attribution of peaks in the spectroscopic curves to the sample properties is ambiguous, and great care has to be taken when doing so. By using a blunt tip, however, no sharp features in the electronic structure of the tip are expected, and the tunneling is dominated by the sample states [32]. The disadvantage is of course, that high spatial resolution with a blunt tip is not possible, and the spectroscopy of single atoms therefore remains a challenge.

3.3 The Imaging of Adsorbates in the STM

It was stated above (section 3.2) that for metal surfaces the STM images generally can be interpreted as topographic maps. This is not so when chemically different adsorbates are present on the surface. This issue has been addressed by several authors, especially by Lang [48, 32, 49, 50] and Sautet *et al.* [43, 44, 51, 52, 53, 54, 55].

The interaction between the sample and the adsorbate will change the metal LDOS at the position of the adsorbed atom and thus it becomes visible in the STM. But that does not necessarily imply that the apparent height of the adsorbate corresponds to the actual one. Lang has calculated the change in LDOS of a jellium metal surface by several adsorbed atoms (He, C, O, Na, S) and the corresponding apparent height of these atoms.

In his studies, the tunneling occurs between two planar metal electrodes, on one of which a Na atom was adsorbed to model the tip, and on the sample electrode several chemically different atoms were adsorbed. The change in LDOS at the Fermi level induced by the adsorbate, i.e. whether it adds or depletes the LDOS, determines how the atom is imaged by STM (either as a 'bump' or as a 'hole'). As a result, Na and S are imaged as protrusions, while He, C and O are imaged as depressions [47, 32, 50].

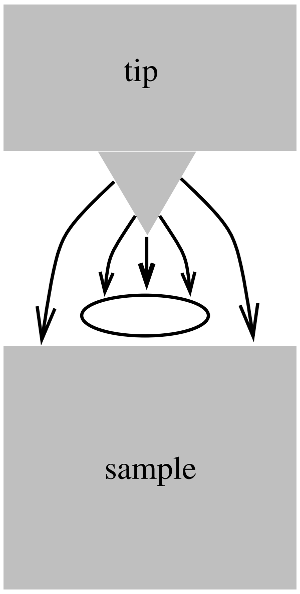

Figure 3.3: Tunneling through an adsorbate. The total tunnel current is an interference of a 'through-adsorbate' and a 'through-surface' contribution (after [54]).

Qualitatively the same result was found by Sautet *et al.* [54], but the modeling of the tip and the surface is more sophisticated and much more information can be gained by this approach. Based on a description of the tunneling process as a scattering phenomenon, the 'electron scattering quantum chemical (ESQC)' approach [43], not only the appearance of single, chemically different adsorbates can be calculated, but also the influence of the chemical nature and configuration of the tip can be taken into account. It was argued that the method allows to extract the binding site and to a certain degree even the bond length and substrate relaxations from experimental STM images [51, 55]. Recently, this method has been used to identify chemically different adsorbates on Pd(111) by their respective cross sections in STM [56]. Also the adsorption site of CO on Pt(111) could be assigned by comparison of simulated and measured STM images [53, 57]. For dense overlayers like the p(2×2)-S structure on Re(0001), interference effects between tunneling electrons emerging from different adsorbate atoms can even lead to a contrast inversion, and assuming a dimer or trimer configuration at the tip apex can lead to several peculiar image 'artifacts' which are quite often encountered in the experiment [44, 51]. It has to be noted that for less dense overlayers or single adatoms no dependence of the tunneling image on the nature or configuration of the tip atoms were found. Very briefly, the approach used in the ESQC calculations for the imaging of single adatoms can be outlined as follows: The tunneling current is divided into two contributions ('through-surface' and 'through-adsorbate' [54]), as is schematically depicted in Fig. 3.3. The 'through-surface' part describes the direct interaction between the surface atoms and the tip and gives the tunnel current for the clean surface when the tip is far from the adsorbate, while the current is slightly different in the vicinity of the adatom. The 'through-adsorbate' channel includes the interaction of the tip and the adsorbate and includes also the adsorbate-surface coupling. Generally, the through-adsorbate contribution generates a bump, whereas the through-surface contribution in most cases generates a depression, at least in the case of strong adsorbate-surface interactions. These two contributions may differ in amplitude by some orders of magnitude, and furthermore the total signal is not merely a superposition of the two parts, but rather an interference. Thus for small electronegative adatoms like O, the total signal is a 0.35 Å deep depression, whereas it is a 0.8 Å high bump for the larger S atoms (for a tunnel voltage of 10 mV and a tunnel current of 1 nA; it must be mentioned that for high tunneling currents the contrast may be different, as was observed for oxygen on Al(111), where the O atoms were imaged as protrusions [58]). This example also indicates that it is not simply the electronegativity which determines the STM images, but the combination with polarizability or orbital size of the adatom. Qualitatively, large and electropositive atoms yield a bump, and small and electronegative atoms give a depression. Along a row in the periodic table, the correlation with electronegativity is good, i.e. the more electropositive atoms cause higher 'through-adsorbate' currents and therefore are imaged more as a bump than a depression, whereas between rows the situation may be different: C and S have comparable electronegativities, but give different STM images [54].

In conclusion, the appearance of adsorbates in STM images depend on various factors and an qualitative image interpretation in the 'bump=atom' sense can be wrong. Adsorbates may be imaged as depressions, and for dense overlayers the shape and chemical nature of the tip can lead to a situation where the regions between the atoms rather than the atoms themselves are imaged as depressions. However, imaging a surface with different tips (geometrically and chemically) and at different tunneling parameters allows to extract valuable information regarding the binding sites and bond lengths and, to a certain degree, even substrate relaxations from STM images. In one study, even a reliability factor for STM has been defined to describe the agreement of calculated and measured STM images [52], in analogy to the r-factors used in low-energy electron diffraction (LEED) (see section 4). However, since the atomic tip configuration is generally not under control of the experimentalist and measurement time is finite, this approach may be limited to only some rare cases where all parameters match favorably.

3.4 The STM Used in the Present Work

For the present studies we used a commercial Omicron STM-1 (Fig. 3.4) that uses the old tripod scanner setup instead of modern single tube versions. It is capable of very good atomic resolution (a sharp tip provided, see next section), but is restricted to image sizes of 4000 Å $\times$ 4000 Å and fairly slow scan rates. The acquisition of one image usually requires about 30–60 s, whereas (some) other STMs are capable of recording several images per second. For the reader interested in the technical details, the manuals [12, 59, 60] or some of the earlier thesis works are recommended [9, 10, 11], where the hard- and software is described in some depth.

3.4.1 The Preparation of STM Tips

It is clear that atomic resolution requires a very sharp tip with only one or a few atom(s) at the apex. To date there is no method to achieve this goal in a controlled, deliberate manner, and it is questionable if this would ever be the case. This, of course, is one of the major drawbacks of STM, in that it subjects the experimenter to chance and fortune.

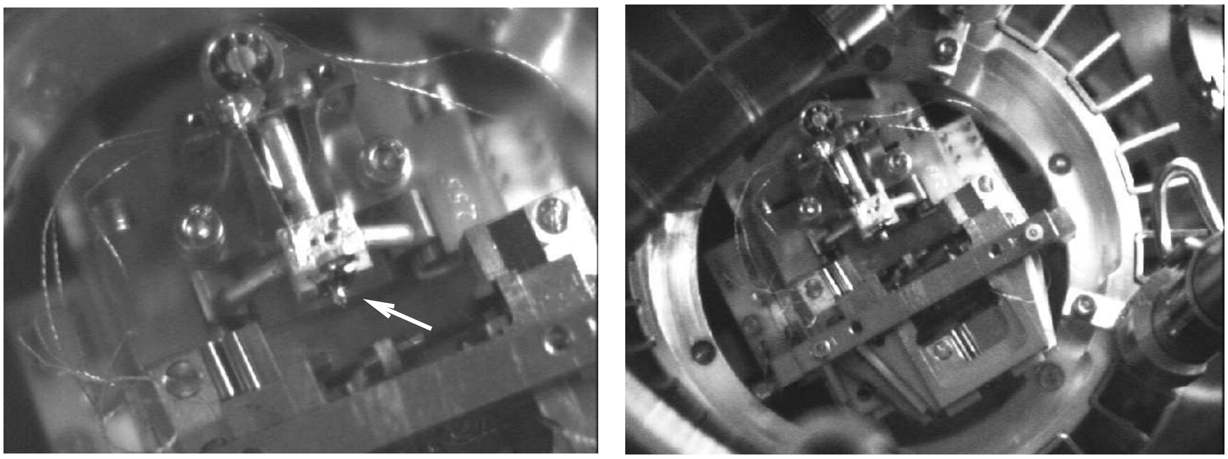

(a) (b)

Figure 3.4: The Omicron STM-1 used in the present work. The tip [marked by an arrow in (a)] is mounted on a tripod scanner. The whole platform, seen in (b), is surrounded by permanent magnets which induce a current in the plates of the copper-ring and thus movements of the platform are reduced (eddy-current damping). The sample, when inserted, is facing the tip.

But as the numerous publications with good or at least sufficient resolution shows, this drawback is not as severe as it may seem. It just takes time.

How is a tip produced? Most of the STM tips are electrochemically etched, using a wire of the tip material (mostly tungsten) as the anode. The electrodes are placed in a solution of KOH (2n) and a dc current of approximately 25 mA and a voltage in the range of 10–25 V is applied. The etching process is fastest at the interface of the liquid, with the result that the part of the anode that dips into the solution becomes too heavy after a while, and the wire tears at the thinnest point. In that instance, when the lower part of the wire falls down, the voltage is switched off immediately by an electronic circuit, and the upper part of the wire is retracted. The cutoff time is 500 ns to prevent further etching of the upper part, which then would become blunt. Of course a tip is not atomically sharp after this procedure, but rather consists of many small "minitips" generated by the tear-off. Hopefully one of those minitips protrudes above the others, and it is that tip that will carry the tunneling current. For further details concerning the etching process and the optimum parameters the reader may refer to [61].

The tips produced in the described manner (an example is given in Fig. 3.5) are then inserted into special holders and transferred to the vacuum, where they are sputtered to remove the oxide layer that has formed during the etching. The subsequent preparation is done during the data acquisition, and consists mainly of voltage pulses up to 10 V which are applied for several ms during scanning, and deliberately "crashing" the tip into the sample a few Å.

It is clear from the above that a tip is by no means ideal and may exhibit several minitips that carry the tunneling current over different parts of the sample, so that the resulting image is a superposition of several scans, each produced by a different tip. This is

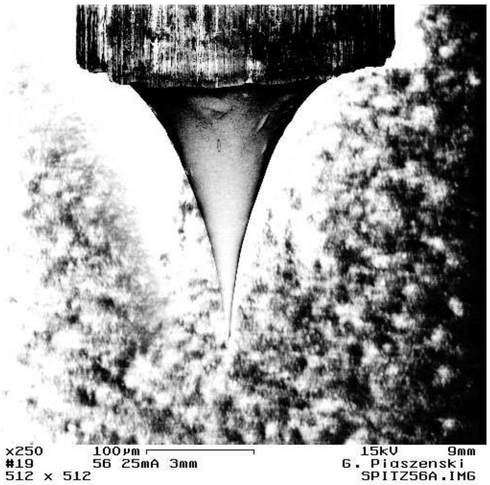

Figure 3.5: SEM (scanning electron microscope) image of an STM tip. The “minitips” that carry the tunneling current are at the outermost apex of the tip (the minitips or not seen in SEM images due to the limited resolution of the instrument).

most often the case if the surface is quite rough and the chance for other minitips to become closest to the surface is higher. STM images must then be interpreted with great care, since they may not reflect the real sample topography anymore. Usually, for reasonably flat surfaces, such multiple tip effects can be easily recognized, since step edges appear doubled or tripled and step heights do not correspond to expected values. This has to be kept in mind when looking at STM images.

4 Low-Energy Electron Diffraction (LEED)

The diffraction of low-energy electrons by single crystal surfaces was discovered by Davisson and Germer in 1927 [62]. Their results confirmed De Broglie's postulate [63] that particles can be described by wave packets and therefore should exhibit diffraction phenomena. In the following, the principle of LEED will be described very briefly, for an in-depth treatment of the subject the reader may refer to e.g. [64, 65].

In a LEED experiment a monoenergetic electron beam impinges on a sample surface and is diffracted by it. A schematic experimental setup is depicted in Fig. 4.1. If the surface atoms in the coherence zone of the electron beam are well ordered, a diffraction pattern can be observed on a screen in front of the surface. The symmetry of this pattern reflects the symmetry of the periodic arrangements on the surface, and the intensity variation of different 'spots' (or beams) in the pattern with primary beam energy can yield quite accurate information on the position and chemical nature of the scattering atoms. Due to the short inelastic mean free path (see section 5.1) of low-energy electrons in solids only atoms located within the first 3–5 atomic layers contribute to the diffracted intensity, which is the reason for the surface sensitivity of the method.

The Ewald construction shown in Fig. 4.1 visualizes the interdependence of the several variables in real space and reciprocal space. A construction of similar triangles allows to determine the vectors of the surface unit cell via the following equation:

$$\frac{t}{R} = \frac{|\mathbf{a_i^*}|}{|\mathbf{k_0}|} \quad \overset{\mathbf{a_i a_j = 2\pi\delta_{ij}}}{\Longrightarrow} \quad |\mathbf{a_i}| = \frac{\lambda R}{t\sin(\angle(\mathbf{a_i}, \mathbf{a_j}))}, \tag{4.1}$$

where $a_{i,j}$ are the lattice vectors of the surface unit cell, $\mathbf{a^*_{i,j}}$ are the corresponding reciprocal lattice vectors, R is the radius of the LEED screen, $|\mathbf{k_0}|$ is the k-vector of the primary electrons, and t is the separation of the diffracted beams on the screen.

The electron wavelength is given by

$$\lambda(\text{Å}) = \sqrt{\frac{150.4}{E(eV)}}. \tag{4.2}$$

As can be seen in the figure, a higher primary electron energy (larger k_0) corresponds to a larger Ewald sphere. Consequently, more rods of the reciprocal space intersect the sphere, which means that more beams are visible on the screen. The diffracted beams move

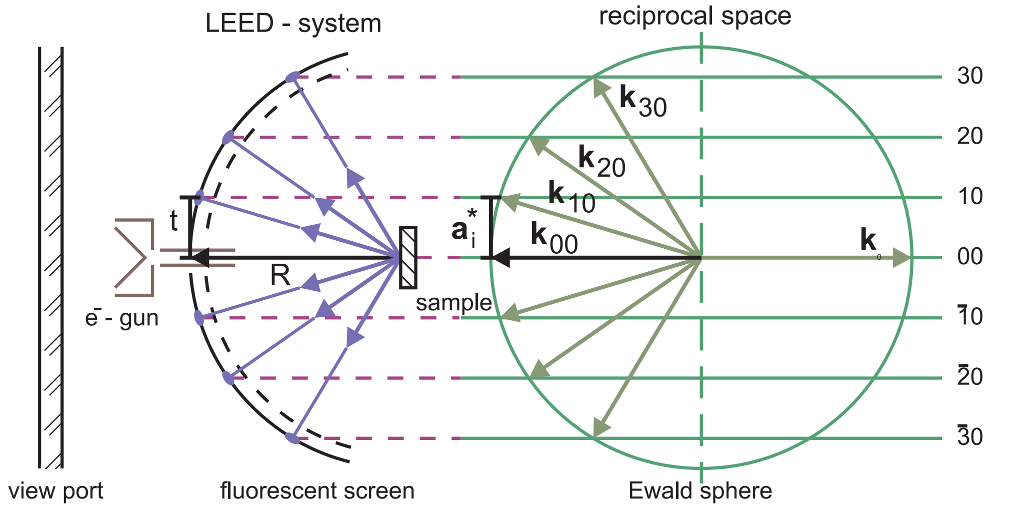

Figure 4.1: Schematic LEED setup (left) and corresponding Ewald construction in the reciprocal space (right), after [66].

towards the (0,0) beam or specular spot if the energy is increased, and move away from the specular spot if the energy is decreased. If facets are present on the surface, several specular spots can be present on the screen and the pattern can become quite complex, since for each facet the diffracted beams move towards their respective specular spot.

All statements based on the Ewald construction, i.e. concerning the *position* of the diffracted beams on the screen use no approximations and are valid also in the framework of more sophisticated theories, which describe the variation of the *intensity* of the beams with varying energy. This implies that not all beams are always visible, even if their position lies within the screen area. At certain energies the intensity of some beams may be zero, or they may be systematically absent at all energies due to equivalent scatterers within the unit cell.

It must also kept in mind when interpreting a given LEED pattern that this pattern corresponds to the average structure(s) present within the area that is hit by the electrons (the total diffracted intensity is a summation over all coherence zones in this area), and the local structure can be much more complicated than the LEED pattern suggests. Due to the averaging, LEED is quite insensitive to local disorder (which shows up only as an enhanced background intensity or a streakiness of the beams) and some structures that are present in only small domains may not be seen in the LEED pattern, especially if the diffracted electrons from these domains do not scatter in phase. Although average domain sizes can be revealed by spot-profile analysis (SPALEED) [66], the local structure is often not accessible by the method. Non-averaging techniques such as STM are better suited for this purpose, and in fact these two techniques are often used complementary.

Although in the present work no dynamical LEED calculations [I(V) analysis] have been performed, some remarks may be allowed concerning the accuracy and the limitations of such calculations. What is done in an I(V) analysis can roughly be described as a 'trial and error' approach to the structure evaluation. A structure is proposed (or guessed), the resulting I(V) profiles are calculated taking into account multiple scattering effects and the result is compared with the experimental curves. If the agreement is acceptable, a refinement is made by varying the atom positions in this model structure by a small amount, of the order of 0.05–0.1 Å (in the last refinement step even smaller). In the past this has been a very tedious procedure, especially if the model structure involves many parameters. With modern numerical techniques like tensor LEED [67], where the refinement procedure is automated, complex structures can be resolved much faster and with higher precision, provided that the model structure is 'not far from the truth', i.e. if the atom positions in the model differ by not more than approx. 0.2 Å from the 'true' coordinates.

An inherent problem remains the judgement whether or not a given set of calculated I(V) curves is better than another. If the deviations are large, e.g. for overlayer structures involving different bonding sites, the decision which model is the best one can often be made by the naked eye. But if more subtle changes like bond lengths are concerned, usually a numeric measure is used to compare the calculated and the experimental curves. These measures are the so-called reliability factors or r-factors, of which several exist, the most prominent and widely used one being the Pendry r-factor or R_P [68].

One of the advantages of the R_P factor is that it provides an estimate for the error bars corresponding to the best-fit parameters via its variance:

$$\Delta R = R_{min}(8V_{0i}/\Delta E)^{1/2}, \tag{4.3}$$

where R_{min} is the overall Pendry r-factor achieved with the best fit, V_{0i} is the imaginary part of the inner potential (which describes the damping of the electron waves inside the crystal), and ΔE is the total energy range (the sum of the energy ranges of all measured I(V) curves of non-equivalent beams). Thus a data set of 2000 eV energy range and a minimum R_P=0.2 would give a variance $\Delta R \approx 0.028$ (assuming $V_{0i} = 5$ eV as a typical value). That means that variations in the atom coordinates leading to r-factor deviations less than 0.028 from the optimum r-factor can be regarded as insignificant.

As a rule of thumb, these insignificant variations are approximately 0.03–0.05 Å for coordinates perpendicular to the surface and 'good' fits (R_P around 0.2). With a very good adjustment and a very effective magnetic shielding even better agreement may be obtained. The sensitivity to the in-plane coordinates is usually a bit lower, and error bars may approach 0.1 Å. What can be learned from equation 4.3 is that r-factor variations in the third digit can be regarded as insignificant in any case. Even with a superb r-factor of 0.1 and a very large data set of 4000 eV one would still obtain $\Delta R = 0.01$ as the limit for significant variations. Although this estimation should not be taken to the extreme, it shows what can be expected from an I(V) analysis. As a lower limit, model structures whose Pendry r-factors differ by only 0.01 or less can be regarded as 'equally good'.

Finally, it may be noted that more than one r-factor should be used in the calculations, since different r-factors are sensitive to different features in the I(V) curves, and a best-fit structure may not be reliable when based on one r-factor alone (details on this topic can be found in [64]).

4.1 Overlayer Notation by Wood

If a surface is covered by an adsorbate whose surface unit cell is different from that of the substrate, a superstructure is seen in the LEED pattern. This is also the case for reconstructions, where the first of the first few atomic layers of a surface differ from the bulk planes. Whereas an unreconstructed surface is, by definition, a (1×1) structure, reconstructions or overlayers can give rise to several superstructures like (1×2), (2×2), c(2×4), ($\sqrt{3}\times\sqrt{3}$) R30° etc. The notation used here (and troughout this work, whenever appropriate) is the one introduced by Wood [69]. A structure is denoted in the general form

$$p(n \times m)R\Phi^\circ \;\text{ or }\; c(n \times m)R\Phi^\circ \tag{4.4}$$

depending on whether the unit cell is primitive (p) or centered (c). The numbers n and m are scale factors which describe the relation of the adsorbate unit cell to the substrate unit cell, i.e.

$$|\mathbf{b_1}| = n|\mathbf{a_1}|;\; |\mathbf{b_2}| = m|\mathbf{a_2}| \tag{4.5}$$

where $\mathbf{b_1}, \mathbf{b_2}$ are the vectors of the overlayer unit cell, and $\mathbf{a_1}, \mathbf{a_2}$ are the vectors of the (unreconstructed) substrate unit cell. The angle Φ indicates a rotation of the overlayer unit cell with respect to the substrate unit cell. If the angle is zero, $R\Phi^\circ$ is omitted (i.e., $R0^\circ$ is not written). Note that Wood's notation can only be used if the angle between the unit vectors of the overlayer and the substrate is the same. If this is not the case, the more general matrix notation applies, which we will not consider here, since it is not used in this text. The interested reader may refer to one of the textbooks on LEED, e.g. [64].

A final remark concerning the sequence of the notation may be allowed. Although no strict definition exists, the number n usually refers to the *shorter* of the unit cell vectors (in real space). So the missing-row structure of the Ir(110) surface (see chapter 8) is denoted (1×2), not (2×1), although the latter is also found in the literature. This convention is used throughout this text.

4.2 Experimental Setup for LEED

For the LEED experiments a 4-grid LEED optics (SPECTALEED [13]) is used, as is depicted in Fig. 4.2. The electron gun produces a monoenergetic electron beam (0–1000 eV) which is focussed on the sample by several lenses. The sample and grid 1 are grounded so that the diffracted electrons can travel along straight lines between the sample and the screen. The whole optics is surrounded by μ-metal for magnetic shielding. To grids 2 and 3 a negative potential is applied (suppressor) so that only elastically reflected electrons can pass. Grid 4 is grounded to reduce the influence of the screen voltage (a few kilovolts to render the diffraction beams visible) on the supressor grids.

The pattern is viewed from the side of the electron gun, so that the (0,0) beam is shadowed at normal incidence. Due to an irreversible misalignment of the sample manipulator, the normal incidence condition can only approximately be satisfied, which sometimes results in a non-degeneracy of otherwise symmetrical beams. But since no I(V) measurements are performed with this instrument, this is of minor importance. The LEED screen is retractable, allowing better sample manipulation in the analysis chamber when the optics is not in use. Patterns are recorded with a simple CCD ('charge coupled device') camera and stored on a computer. Since the signal-to-noise characteristics of the used camera is poor, an averaging of usually 10–20 images is used to enhance contrast. But still the quality of the recorded images is unfortunately not quite comparable to the pattern seen by the naked eye.

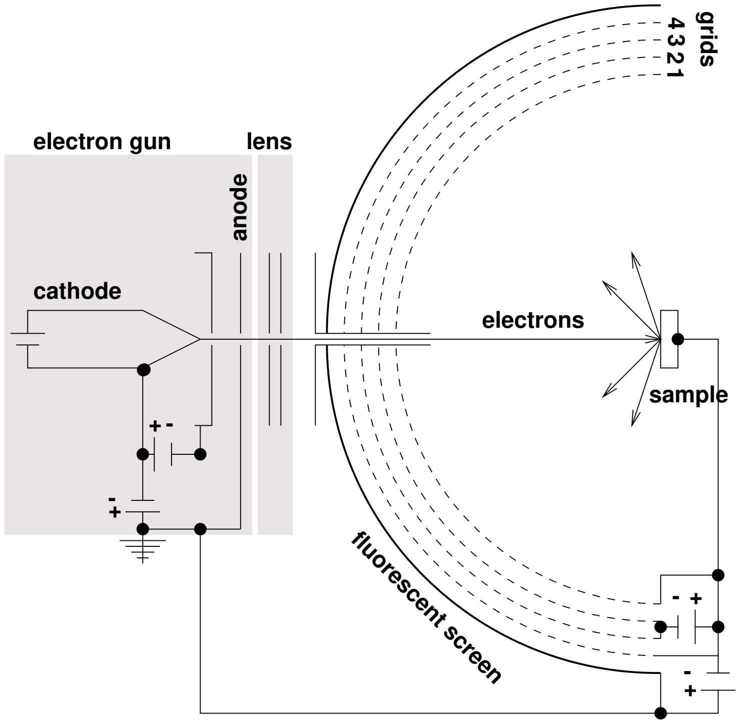

Figure 4.2: Schematical representation of a 4-grid LEED optics (after [11]).

5 Chemical Surface Analysis by Auger Electron Spectroscopy (AES)

Neither STM nor LEED can provide detailed chemical information. Although both methods are sensitive to the chemical nature of atoms, an easy and unambiguous assignment cannot be made in general. The standard tool to gather information about the chemistry of surfaces is electron spectroscopy, where the surface is hit by either a high-energy electron beam or by photons in the soft X-ray regime, and the excited atoms can be identified by electrons of characteristic energy that are emitted in the deexcitation process.

Both X-rays and energetic electrons (usually 3–10 keV) excite a core level electron to the vacuum level, and this initial vacancy is filled by an electron from a higher level. The excess energy is either removed by a photon (photoelectric effect) or by a second electron (Auger effect [70]) of suitable kinetic energy. In X-ray photoelectron spectroscopy (XPS) the directly emitted core level electrons are detected, and the kinetic energy of these electrons allows an identification of the corresponding core level, which in turn is characteristic for the chemical nature of the emitting atom. It is clear that the kinetic energy of these electrons depends on the energy of the exciting radiation.

In Auger electron spectroscopy (AES), the Auger electrons are detected (due to the high energy of the primary beam the directly emitted electrons have much higher kinetic energies than in XPS and are not detected below 2000 eV kinetic energy), whose kinetic energy again is a fingerprint of the emitting atom, as will be described below. The kinetic energies of Auger electrons are usually in the range of 30–2000 eV and due to the short inelastic mean free path (IMFP) of only a few Å for electrons of this energy, electron spectroscopy is surface sensitive.

For the light elements (up to $Z \approx 30$) [71], the Auger process is the dominating deexcitation mechanism which can be described as follows: A core level electron (e.g., a K-shell electron) is excited to the vacuum level by the high-energy primary electrons, and the initial vacancy is filled by electrons from the same or higher atomic levels (e.g. from the L-shell). The excess energy of the deexcitation electron is transferred to another electron, which is then emitted. The resulting energy balance for a KL_1L_1 process is (compare Fig. 5.1:

$$E_{KL_1L_2} = E_K - E_{L_1} - E^*_{L_1}, \tag{5.1}$$

where $E_{KL_1L_2}$ is the kinetic energy of the emitted Auger electron, E_K is the binding energy of the electron in the K-shell (the initial vacancy), E_{L_1} the binding energy of an electron in the L_1 subshell, and $E^*_{L_1}$ the binding energy in the L_1 shell when an electron in the same shell is already missing. To accurately calculate $E^*_{L_1}$, the complete electronic configuration of the atom has to be taken into account, since the missing electrons lead to a change in binding energies for the remaining ones. If $E^*_{L_1}$ is simply approximated by the energy E_{L_1} of the unperturbed atom, the resulting kinetic energy for the Auger electron would be too large. The use of correction terms is necessary to obtain a good agreement with the experiment [20].

As can be seen from equation 5.1, the kinetic energy of the Auger electrons is independent of the primary beam energy, provided that it is high enough to ionize an atom core level. But the primary beam energy *does* influence the transition matrix elements between the involved atomic levels and thus has an effect on the intensity of the observed transition.

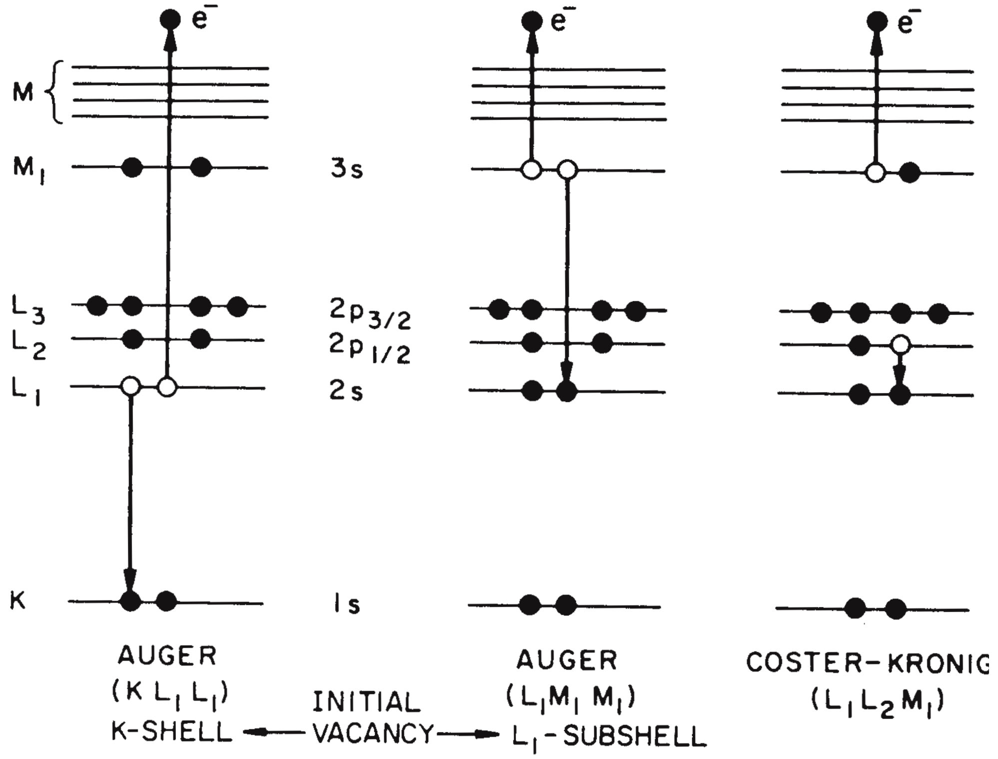

Figure 5.1: Schematic representation of the Auger process. On the left the usual X-ray notation is given, in the middle the corresponding spectroscopic terms are noted. A KLL (left) and a LMM (middle) transition are depicted. In a Coster-Kronig process (right) the initial L_1 hole is filled by an electron of the same shell but different subshell, L_2 (from [20]).

The transitions in which the initial vacancy and one of the final vacancies lie in the same shell (but different subshell) are called Coster-Kronig transitions. These are very fast, and thus reduce the intensity of the normal Auger processes. In the experimental praxis the usual approach is to compare a measured spectrum with a set of standard spectra, which either have been recorded in the same lab using elemental standards, or to refer to published reference spectra [72, 73]. The use of standard spectra that have been measured with the same experimental setup has the advantage that instrumental factors are immediately included, but this procedure is tedious since it requires to measure spectra for each element of interest.

In most cases, however, tabulated spectra in the literature are used for comparison. If only the identification of peaks is required, this method is well suited, but it can lead to inaccurate results when it comes to a quantitative evaluation of the spectra. This is especially important when the reference spectra have been measured with a different type of analyzer than used in the own lab. The relative intensity of the transitions, the so-called sensitivity factors, may be different in such cases due to the different transmission functions of the analyzers.

5.1 Quantitative Spectra Analysis

As already mentioned, several difficulties arise when a quantitative analysis of AE spectra is required. If no elemental standard spectra measured with the same apparatus are available, tabulated spectra must be used for comparison. Provided that the tabulated sensitivity factors can be assumed to be the same for the analyzer in the own lab, several approaches exist to calculate the atomic concentration of a given element (e.g. an adsorbate or a component of an alloy).

If the elemental components are homogeneously distributed in the sample, the concentration C_A of element A is approximately given by

$$C_A = \frac{I_A/S_A}{\sum_i I_i/S_i}, \tag{5.2}$$

where I_i and S_i are the intensity and sensitivity factor of the transition corresponding to element i, respectively. For historic reasons, the sensitivity factors correspond to the peak-to-peak amplitudes of the differentiated dN(E)/dE signals. Today's analyzers often acquire direct N(E) spectra, which are subsequentially differentiated by numerical procedures. A differentiation and smoothing algorithm that is widely used in the analysis of Auger spectra is the one developed by Savitzky and Golay [74], which was especially designed to maintain peak positions and heights in the smoothing procedure. If not mentioned otherwise, the spectra shown in this work have been smoothed and differentiated using a Savitzky-Golay filter with a 4 eV window, to be consistent with the spectra published in [73].

Strictly speaking, equation 5.2 is appropriate only for transitions of the same energy. Due to the energy dependence of the IMFP (see below) the sample volume that contributes to the signal will be different for different transitions. Therefore, the relative intensities of the different transitions will be influenced. But since the mean-free path varies only slowly with energy, the corrections are negligible if the peaks are not too far apart.

Another approximation that underlies equation 5.2 is the assumption that only primary beam electrons can excite the sample atoms. This is not true since energetic back-scattered electrons also contribute to the ionization. The actual ionization is therefore higher, which is described by a backscattering factor R [75]:

$$R = 1 + \frac{I_B}{I_P} \tag{5.3}$$

where I_B, I_P are the Auger intensities excited by primary and backscattered electrons, respectively. The backscattering factor is a function of the energy E of the Auger transition of interest, energy E_p and angle (with respect to the surface normal) of the primary beam, and the atomic number Z of the backscattering material. Several numerical parametrizations for the evaluation of R exist, the one by Ichimura *et al.* [76], which is applicable also for low energies, is given below:

$$\begin{aligned} R &= 1 + (4.35 - 3.93Z^{0.1})(E_p/E)^{-0.25} + 4.85Z^{0.1} - 5.45 && (5.4) \\ R &= 1 + (2.00 - 2.14Z^{0.1})(E_p/E)^{-0.30} + 3.01Z^{0.1} - 3.05 && (5.5) \end{aligned}$$

for a primary beam normal to the surface or at 45°, respectively. If backscattering is taken into account, the so-called matrix factors F_{AB} (for a binary alloy) in equation 5.2 becomes

$$\begin{aligned} \frac{C_A}{C_B} &= F^A_{AB}\frac{I_A/S_A}{I_B/S_B} && (5.6) \\ F^A_{AB}(C_A \to 0) &= \left[\frac{\lambda_A(E_A)R_A(E_A)}{\lambda_B(E_A)R_B(E_A)}\right]\left(\frac{a_B}{a_A}\right)^3 && (5.7) \\ F^A_{AB}(C_A \to 1) &= \left[\frac{\lambda_A(E_B)R_A(E_B)}{\lambda_B(E_B)R_B(E_B)}\right]\left(\frac{a_B}{a_A}\right)^3 && (5.8) \end{aligned}$$

where $R_{A,B}(E_{A,B})$ are the backscattering factors for electrons of the energy E_A or E_B in a matrix of atoms A or B, respectively, $\lambda_{A,B}$ are the IMFPs in material A or B, and $a_{A,B}$ are the atomic sizes for elements A, B.

For the IMFP, again several 'universal formulae' exist, perhaps the most prominent being the one of Seah and Dench [77]

$$\lambda_M = 0.41 a_M^{1.5} E_M^{0.5}. \tag{5.9}$$

However, the IMFPs calculated by equation 5.9 deviate up to 30% from the experimental values and represent a major source of inaccuracy. The formula by Seah and Dench is only a fit to the experimental data available at that time (1979), and more sophisticated approaches are available today (e.g. the so-called TPP-2 parametrization of Tanuma *et al.* [78]). But still, the IMFPs calculated using such formulae may deviate significantly from the experimental data (if available), and the values have to be taken with care. A critical and historical review of such predictive formulae has been published by Powell [79].

If the elements in the sample are not homogeneously distributed, equations 5.2 and 5.6–5.8 are no longer applicable. It is an inherent problem of electron spectroscopy that the elemental depth distribution is usually unknown. For XPS, the distribution function can be obtained via an analysis of the inelastic background [80]. For AES, however, reliable procedures do not exist to date, since the problem is more involved because not only the emitted electrons may be inelastically scattered on their way to the surface, but also the primary electron distribution is unknown.

A special case where the elemental depth-distribution is known is the analysis of adsorbates on a surface, provided that no intermixing between adsorbate and substrate occurs. For a thin film of thickness a_A of an adsorbate A at a submonolayer coverage $\theta_A < 1$ on a substrate B the following equation holds [81]:

$$\frac{\theta_A[1-\exp(-a_A/\lambda_A(E_A)\cos\phi)]}{1-\theta_A[1-\exp(-a_A/\lambda_A(E_B)\cos\phi)]} = \left[\frac{R_A(E_A)}{R_B(E_A)}\right]\frac{I_A/S_A}{I_B/S_B} \tag{5.10}$$

where ϕ is the angle of emission with respect to the surface normal. For small coverages and large IMFPs (high transition energies), this simplifies to:

$$\theta_A = Q_{AB}\frac{I_A/S_A}{I_B/S_B} \tag{5.11}$$

$$Q_{AB} = \left[\frac{\lambda_A(E_A)cos\phi}{a_A}\right]\left[\frac{R_A(E_A)}{R_B(E_A)}\right] \tag{5.12}$$

The IMFP in equations 5.10, 5.12 may either be calculated using one of the predictive formulae (e.g. equation 5.9) or by referring to tabulated values [82]. For further information on the quantification of AES (and the difficulties arising when trying to do so), the reader may refer to [83].

5.2 Experimental Setup for AES

For the AES measurements of the present work the sample is irradiated by a primary beam of several keV (STAIB electron source [14]) at an angle of 50° to the surface normal, as depicted in Fig. 5.2. The Auger electrons are detected in normal emission with a Physical Electronics (Mod. 10-360) Concentric Hemispherical Analyzer (CHA) [15] and a single channel detector. The analyzer is used in the Fixed Retard Ratio (FRR) mode. If not stated otherwise, a step size of 1.0 eV and an acquisition time of 20 ms per step are used in the measurements. Primary beam energy is 5 keV, and for each spectrum 200 sweeps are averaged to obtain an acceptable signal-to-noise ratio and to diminish effects of an instable primary beam current (the electron gun produces a stable emission only after a very long 'warmup' time of more than one hour, and spectra recorded during this warmup require sufficient averaging).

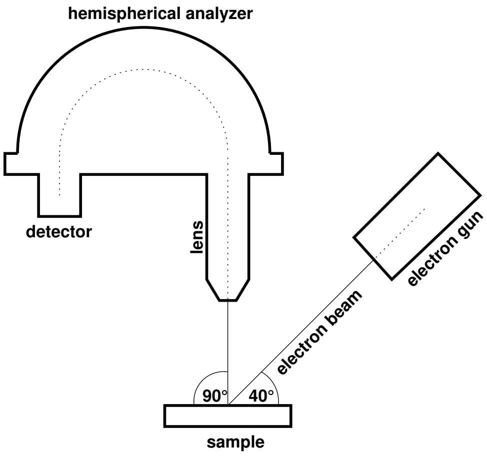

Figure 5.2: Schematic AES setup.

6 The Structure of the Clean Ir(110) Surface

6.1 Previous Work

The Ir(110) surface has been studied by numerous authors [2, 84, 85, 86, 87, 88, 89], and it was among the first metal surfaces that were found to exhibit surface reconstructions.

The first experiments were done in 1973 by Christmann and Ertl [2], who observed a (1×2) LEED pattern. In several dynamical LEED I(V) analyses by Chan and coworkers [90, 91, 92, 84] different models for the (1×2) structure were tested and best agreement was found for the missing-row reconstruction with multi-layer relaxations that was also reported for the (1×2) structures of Pt(110) [93] and Au(110) [94]. The missing-row model and the best-fit parameters are shown in Fig. 8.2 and table 8.1.

In 1989, Hetterich and Heiland proposed a different model for the Ir(110) surface, based on ion scattering experiments [85]. They could not reproduce the (1×2) LEED pattern for the clean surface, but rather found a 'streaked' (1×3) pattern instead. Furthermore, the ion-scattering data were clearly not in agreement with the proposed (1×2) model, but indicated a structure of (1×3) missing-row type with two missing first layer rows and one missing row in the second layer. Further ion scattering experiments by Bu *et al.* refined their results and found best agreement for a mixed (1×3) and (1×1) structure [95]. The (1×2) structure was indeed suggested to be caused by slight Si contaminations [96], which may have been overlooked in the early experiments.

However, despite the experimental effort, the structure of the clean surface remained controversial until in 1991 an STM study of Koch *et al.* revealed the stabilization via (331) minifacets (this structure will be described in detail in the following section). Their results were corroborated by Avrin and Merill with He atom diffraction [88] and our own work [89], and are starting to replace the old notion still found in some modern reviews [97] that the (110) surfaces of Ir, Pt, and Au are all (1×2) missing-row reconstructed. Because this has been stated since 1979 [90], the 'new' insight may take some time to become commonplace, and indeed careful reviews are already found which do not repeat the old findings anymore [47]. Although there is no longer a debate concerning the structure of Ir(110), the structure still awaits careful theoretical work to reveal its driving forces.

6.2 Results of the Present Work: The (331) Faceted Surface

After sputtering and annealing to 1000 K, the AE spectrum shows no significant amounts of impurities (Fig. 6.2). The surface exhibits a 'streaked' LEED pattern with split spots at some energies, whereas at other energies the spots appear sharp and resemble a (1×3) symmetry. A sequence of LEED pattern at different energies is shown in Fig. 6.3. The complex movement of the spots, which seem to merge and split again at different energies, indicates diffraction from a surface with extended facets. The specular spots of the facets lie outside of the screen, but can be seen in the middle of it after changing the angle of incidence from 'normal' [with respect to the (110) surface] to off-normal. Due to the rotational axes of the manipulator this can only be accomplished after azimuthally rotating the sample by 90°. The tilt angle (in [001] direction) needed to have normal incidence on the facets is then approximately ±13°. The corresponding facets are therefore planes tilted by this angle against the (110) plane, as depicted in Fig. 6.1. This is in good agreement with the model proposed by Koch *et al.* [87], who found a surface consisting of alternating (331) and $(33\bar{1})$ facets, as is schematically shown in Fig. 6.4(a). A (331) facet is tilted by 13.3° against the (110) plane, whereas a (111) facet is inclined by a much steeper angle of 35.3° [Fig. 6.4(b)].

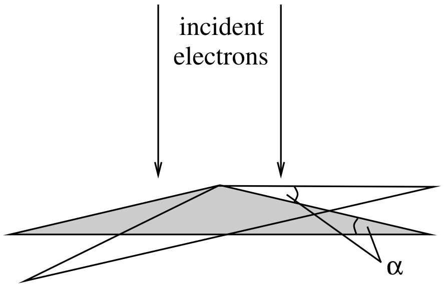

Figure 6.1: An electron beam impinges on a faceted surface. By tilting the sample, the beam can be brought to normal incidence with respect to the facets. The tilting angle is the same as the inclination angle of the facets with respect to the flat (macroscopic) surface.

STM images of the surface show a mesoscopically 'rippled' surface (Fig. 6.5, consisting of ridges of varying width. A single ridge is formed by a $(33\bar{1})$ and a (331) facet and a double row in a (1×1) spacing on top, as in the model of Fig. 6.4(a). The inclination angle of the facets seen by STM is 10–15° with respect to the average image plane, also in good agreement with the proposed model. It must be noted that the experimental values may be subject to some error, since the subtraction of a reference plane is difficult: Only the double rows on top of the facets can be used, and the slope subtraction from this tiny 'plane' may be flawed. However, a (111) facet that is expected for (1×2) or (1×3) missing-row structures would incline at a much steeper angle of 35.3°, which is clearly beyond experimental error. Furthermore, the sections across the ridges in (nearly) atomically resolved STM images show small 'bumps' at the sides of the facets, laterally separated by approx. 6 Å (Fig. 6.6), caused by the steps of the (331) facets. For the steep (111) facet, no such steps would be observed by STM, which is also known for different step types formed on Au(110)-(1×2) [98].

The width of the ridges is not strictly uniform, as seen in Fig. 6.5(a) and (b), which are of similar size. The reason may be that the system has not yet arrived at the thermodynamic equilibrium, in which it possibly would form ridges of a fixed width, or this 'disordered' configuration is indeed the structure of lower free energy because of the en-

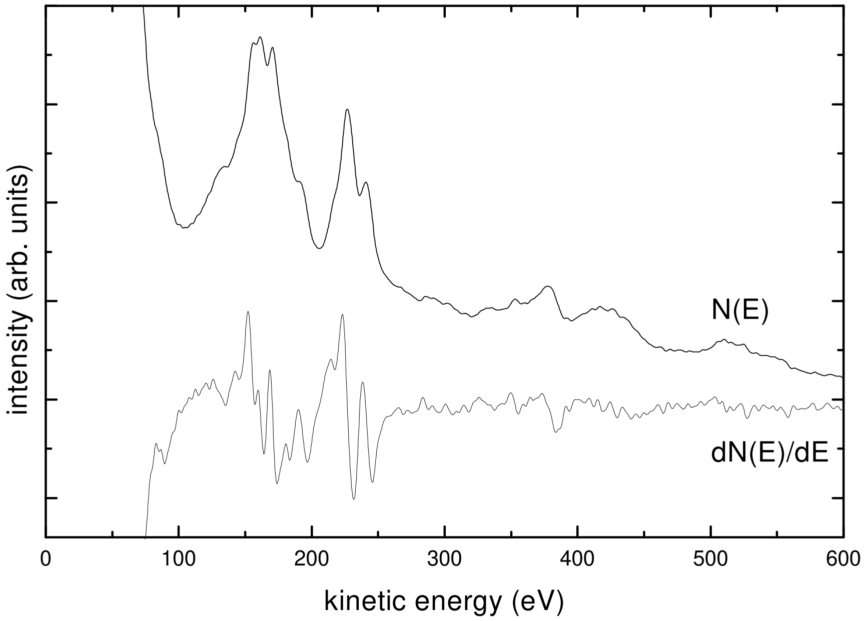

Figure 6.2: AE spectrum of the clean Ir(110) surface. In the upper part the direct N(E) spectrum is shown, below the differentiated dN(E)/dE spectrum is given.

hanced entropy. Some parts of the surface can be found which exhibit a rather uniform spacing of approximately 40 Å between the ridges, and generally the maximum widths observed are of the order of the one seen in Fig. 6.5(b), which is about 120 Å. Apparently, an upper limit for the facet size exists (which is reasonable, since the effective surface becomes larger for extended facets, which can thus be expected to be energetically unfavorable beyond a certain size), and on average the width of the ridges is approximately 40 Å. The annealing temperatures had no significant influence on the width distribution, only the length of the ridges in $[\bar{1}10]$ increases with increasing temperature. It may be noted that on some parts of the surface a long-wavelength superstructure could be observed in the largest images [Fig. 6.5(a)], which may be a large-scale periodic hill and valley structure as observed on Pt(110) [99] (see below). However, due to the limited scan size of 4000 Å of our STM, the presence of such a long-range superstructure on extended parts of the surface cannot be verified in the present experiments.

The observed width distribution is in agreement with the findings of Koch *et al.* who reported 30–100 Å [100], but is significantly larger than the average separation of 18 Å between two neighboring ridges, observed by Avrin and Merrill with He diffraction analysis [88]. This may be due to the different preparation procedures used by these authors, who did not clean the surface by sputtering/annealing cycles, but used mostly flashing to high temperatures and oxygen treatments. The AE spectra shown in [88] show no significant amounts of contaminants, so impurities may not be the cause for the difference, but rather the annealing temperature and time. Furthermore, information regarding the terrace widths in He atom diffraction requires a careful measurement of the widths of the diffracted beams as a function of several parameters, which has not been done

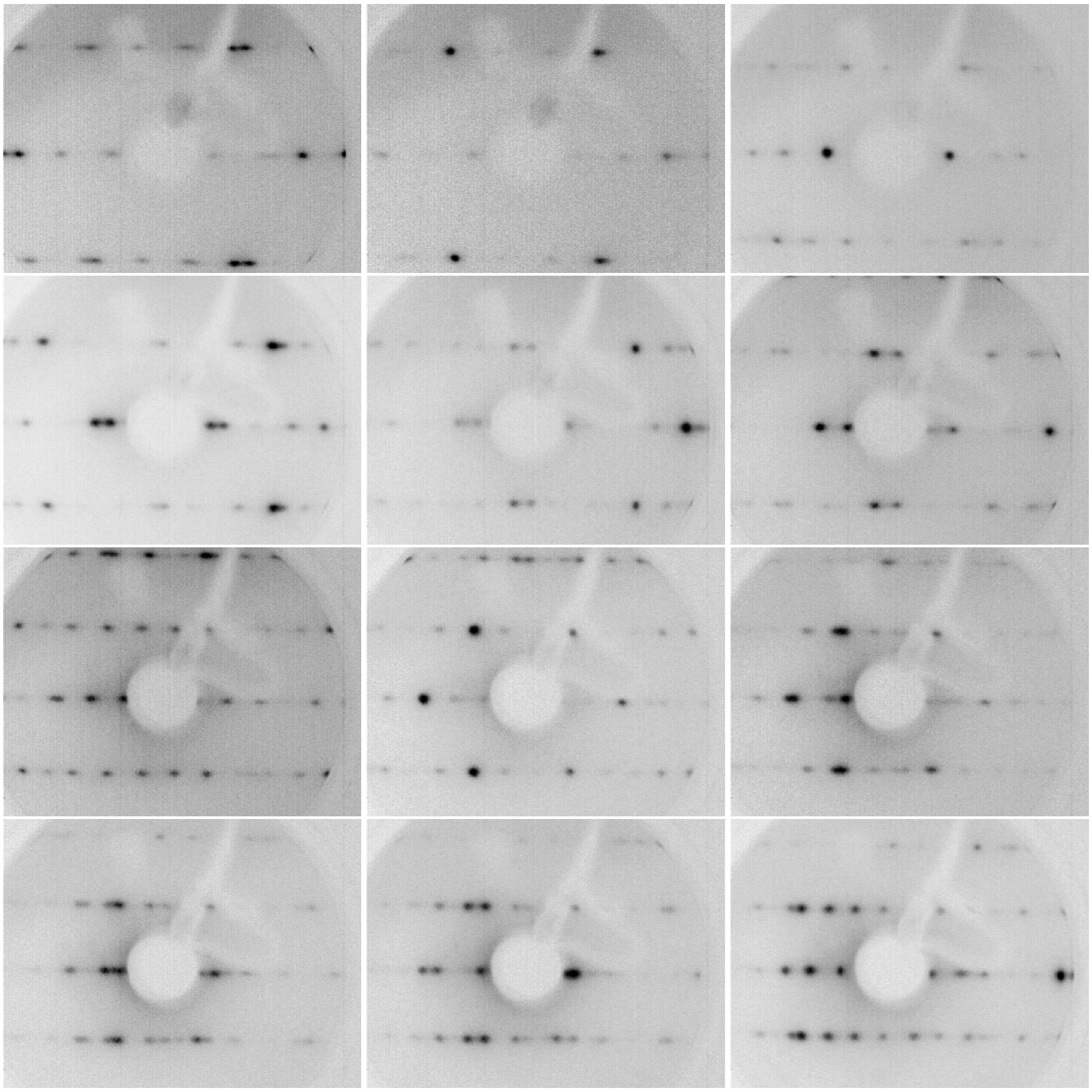

Figure 6.3: LEED pattern of the clean Ir(110) surface. Electron energies are (from left to right and top to bottom) 90, 96, 137, 156, 168, 178, 197, 208, 218, 228, 238, 258 eV. Due to an irreversible tilt of the manipulator head, the left and right sides of the images are not equivalent (slightly off-normal incidence). The complex movement of the diffracted beams gives rise to spot 'splitting' at certain energies (compare the bright spots at both sides of the electron gun in the center at 137 eV and 156 eV, respectively).

in the analysis in [88]. The quoted value of 18 Å was obtained for the broadest diffraction beams and hence may rather be regarded as a lower limit for the average separation.

As can be seen in Fig. 6.6(a), atomic resolution along the rows in $[\bar{1}10]$ direction is not always achieved. In fact, the situation shown in the figure is typical, and it turned

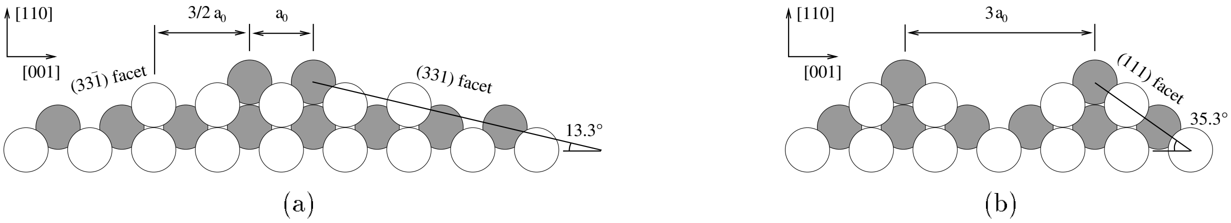

Figure 6.4: Schematical ball models for proposed structures of Ir(110). (a) Faceted structure, note the double row on top. The (331) facets are inclined by 13.3° against the (110) plane. (b) (1×3) missing-row structure with (111) facets, which form a steeper angle of 35.3° with the (110) plane.

out to be extremely difficult to obtain atomic resolution along the close-packed direction. Nevertheless, it can be achieved [Fig. 6.6(b)]. To exclude image artifacts due to periodic vibrations of the tip, it was assured that the features scale and rotate according to the atomic structures when varying the scan size or direction. This would not be the case for features caused by vibrations, which in general do not scale and rotate together with the atomic structure. Speaking of artifacts, it may be mentioned that double or multiple tip images are frequently observed on this comparably rough surface, which makes the acquisition of large-scale images as Fig. 6.5 difficult.

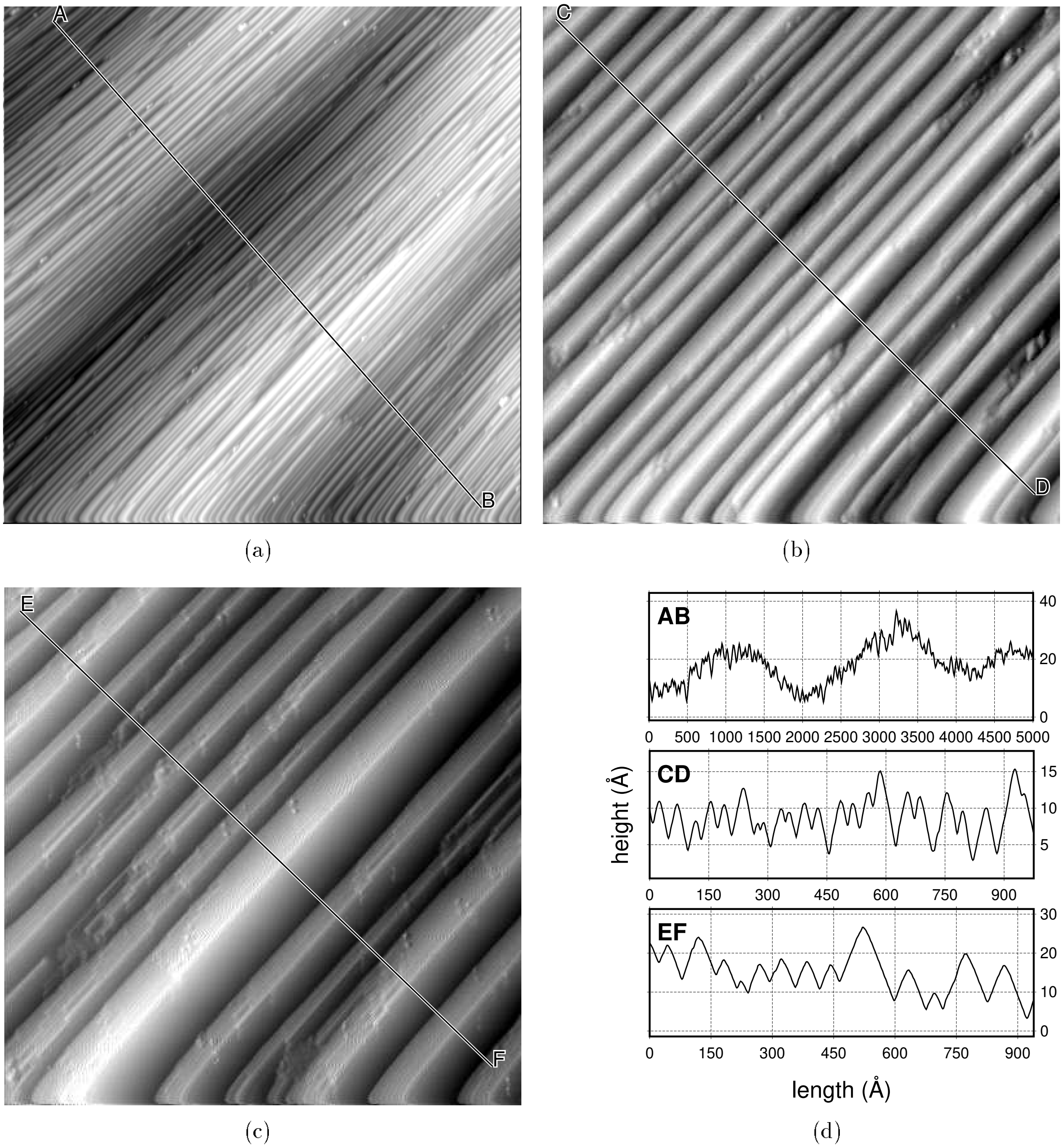

Figure 6.5: Overview STM images of the clean Ir(110) surface. Sections along the indicated lines are shown in (d). In (a) a large-scale 'waviness' can be observed (compare section). The distribution is not uniform, as seen by comparison of (b) and (c), which show an area of similar size. The average width in the section of image (b) is approx. 44 Å, whereas in (c) it is approx. 70 Å. The large ridge in (c) has a width of about 120 Å. Tunneling parameters are U_t=0.9 V, I_t=1 nA for all images, sizes are (4000 Å)^2 for (a), and (770 Å)^2 for (b) and (c).

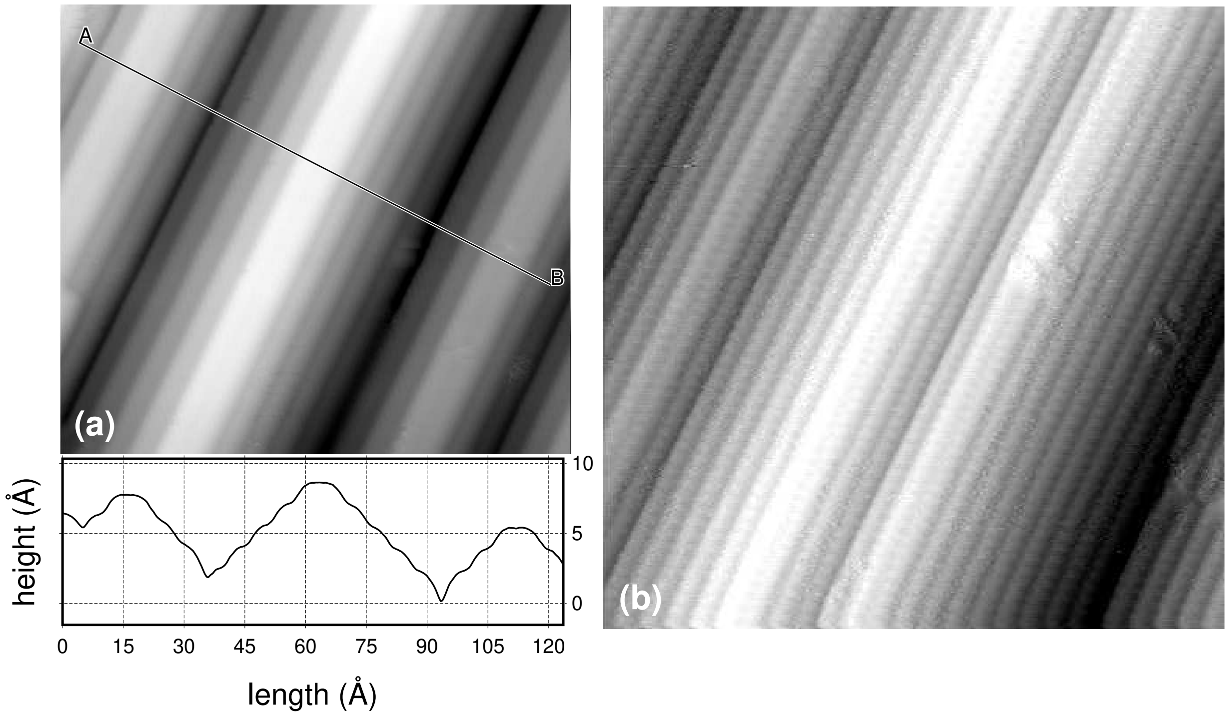

Figure 6.6: Atomically resolved STM images of the clean Ir(110) surface. (a) Typical image with no resolution along the close packed [$\bar{1}$10] rows. The 'bumps' at the sides of the facets seen in the section are approx. 6 Å apart. This and the inclination angle of 15° is consistent with the model shown in Fig. 6.4(a). In (b) also the rows are atomically resolved. Tunneling parameters U_t=-50 mV, I_t=3 nA (a) and U_t=20 mV,I_t=1 nA (b), image sizes (120×105 Å)^2 and (160Å)^2 for (a) and (b), respectively. Both images are slightly differentiated to enhance contrast.

6.2.1 Origin of the Faceted Structure, Comparison with Pt(110) and Au(110)

To date the origin of the faceted reconstruction is not known. In fact the surface behaves completely different than the (110) surfaces of neighboring elements in the periodic system, Pt and Au. Both Au(110) and Pt(110) exhibit a (1×2) missing-row reconstruction (see Fig. 8.2), in which every other close packed [$\bar{1}$10] row of the first layer is missing. One of the driving forces for the reconstruction of Au and Pt is the formation of energetically favorable (111) microfacets, whereas steps of (331) type were shown to be unfavorable [101]. In fact even larger missing-row structures like (1×3) [Fig. 6.4(b)] were predicted to be, in essence, energetically degenerate within the framework of the calculations [102]. So far, however, experimental evidence suggests that (1×3) missing-row structures of Au(110) and Pt(110) are stabilized by small amounts of alkali metals [103, 104, 105, 106] and do not form spontaneously on the clean surfaces. Larger missing-row structures than (1×3) with extended (111) facets have not been observed so far. A reason why (1×n) structures with $n > 3$ are not found may be that the effective surface in such cases would become too large due to the extended facets.

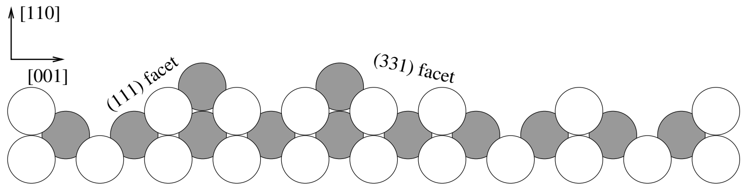

Figure 6.7: Model of a (1×2) missing-row reconstructed (110) surface with a small island of the same reconstruction. If no domain boundaries are present, the two steps in [001] direction are of a different type.

Despite the only marginal energetic difference for the (111) and (331) type steps, the latter is almost completely avoided in the case of Au(110) and Pt(110). On Pt(110), the so-called fish-scale pattern is a mesoscopic structure whose formation is mainly driven by the small energetic differences between the two step types [107, 108, 109]. The same structure has also been observed on Au(110) surfaces, and (331) steps were only occasionally observed [104, 98]. This is surprising, since for a (1×2) reconstructed island on a (1×2) reconstructed terrace, one step at the island edge *must* be a (331) step if no domain boundaries in the terrace or the island are present (Fig. 6.7). But it seems to be energetically favorable to form such boundaries rather than accepting a (331) step. The fish-scale pattern develops when mass transport is high enough to build further islands, each of them 'hiding' a domain boundary in the terrace underneath, so that (331) steps are completely avoided.

With regard to the 'efforts' that Pt(110) and Au(110) 'undertake' to avoid (331) steps, it is indeed surprising that on Ir(110) it is the only step type that is observed. It may be argued that for Ir(110) the situation could be reversed, i.e. the (331) steps are energetically more favorable than (111) facets, which could then be the driving force for the observed faceting. So far, however, such calculations are not available for iridium, and one can only speculate.

Only recently a large-scale periodic hill and valley structure, also called corrugated iron structure, was reported for Pt(110) [99]. Although the driving forces of that structure are still under debate [99, 110, 111, 112], surface stress is believed to play a key role. It may be speculated that the same holds for the Ir(110) surface, and that the mesoscopic rippling is not just due to a (possible) energetic preference for (331) steps, but also driven by stress relaxation. The mere resemblance of the corrugated iron structure on Pt(110) and the rippled structure of Ir(110), however, is a too simplistic argument to justify this assumption, since there are striking differences between the two structures. The most obvious is the wavelength of the superstructure. While on platinum a mesoscopic 'rippling' with a period of 1480 Å is observed, the average distance between two ridges on Ir(110) is only about 40 Å, as shown above. A second difference is the nature of the ridges itself: While on Ir(110) extended (331) facets with a fixed step-step distance are formed, this distance is not fixed for Pt(110), but exhibits a broad distribution [112], i.e. no facets are formed. Last but not least, Pt(110) is missing-row reconstructed while Ir(110) is not, which also makes a comparison of the mesoscopic structures questionable. Furthermore, before speculating about a possible common origin for the two mesoscopic structures, it must be investigated if an additional large-scale periodic superstructure is absent on Ir(110) or not. As mentioned above, sections across large images show a hill and valley structure with a period of approx. 2000 Å [Fig. 6.5(a)]. However, STM images of much larger scale than possible with the instrument used in this study have to be taken to clarify this point.

In general, without referring to a mesoscopic superstructure of any form, stress relaxation is one of the important factors in determining surface structure [113, 114, 115, 116, 117, 118, 119]. The origin of surface stress can be visualized as follows: At a surface, the atoms have a lower coordination than those in the bulk, and thus are located at a lower charge density than they would be in the bulk. This situation is unfavorable and the atoms rearrange towards regions of higher charge density, i.e. they relax inwards. However, due to the electrostatic repulsion between the atoms of the first and second layer, the relaxation cannot fully restore the bulk charge density, in other words: The inward displacements are too small to fully relax the structure. The charge density at the position of the relaxed surface plane is still lower than the bulk value, and the only way to increase the charge density further would be to shorten the in-plane atomic bonds. Since the surface atoms are forced to stay in registry with their bulk neighbors (i.e., the in-plane contraction is not allowed or is insufficient), the surface plane is under tensile stress. It may be noted that indeed cases are found where such in-plane bond contractions occur, lowering the tensile stress [120].

Recently, in an *ab initio* study by FILIPPETTI and FIORENTINI the (1×2) missing-row model was compared with the unreconstructed surface for Ir(110) [118] [unfortunately, the (331) faceted model was not considered, although this reconstruction was first reported several years before the theoretical study]. The (1×2) reconstructed surface was found to be energetically favorable compared to the unreconstructed surface, although the surface stress for the reconstructed structure was even higher. Calculations concerning the (331) faceted model are thus highly desirable to eventually close the case of the Ir(110) reconstruction.

7 The Adsorption of Oxygen on Ir(110)

7.1 Previous Work

The structure of chemisorbed oxygen on the Ir(110) surface has been studied by a number of authors, e.g. [2, 121, 122, 123, 95, 124, 125, 126, 100].

Several oxygen-induced structures were reported in those studies, namely (1×1) (all studies), c(2×2) (all studies), p(2×2) [2, 121], (3×2) [121], and (1×4) [121]. The latter two have only been observed in one study, and no quantitative evaluation was given. The (1×4) structure was obtained after annealing at 1200 K in an oxygen atmosphere, or alternatively, after heating an oxygen precovered surface to 700–1200 K for a few minutes. The (1×4) structure was attributed to an oxide layer similar to oxides reported on Pt (for a review see [16]). But as for Pt, it can be argued that this oxide layer may be attributed to oxidized impurities such as Si, which was found to be present in the Pt "oxides" [16, 17]. This is also suggested by the findings of HETTERICH, who could obtain a (1×4) LEED pattern only after oxidation of a Si-contaminated sample [125]. Furthermore, BU *et al.* could not reproduce the (1×4) structure in their experiments [95]. In the present work, none of the Si-related structures has been observed at any stage of the sample preparation.

The (3×2) pattern was also observed after heating the crystal near 1000 K in an oxygen atmosphere [121], but the LEED pattern indicated a high degree of disorder and no structural model was proposed.

The p(2×2) pattern developed after exposing the (1×2) reconstructed Ir(110) surface to oxygen at room temperature, sometimes followed by a mild annealing at 370 K in vacuum [2, 121]. It was associated with dissociatively adsorbed oxygen (a molecularly chemisorbed oxygen species was observed only up to 100 K), and a structural model was proposed with oxygen atoms over short-bridge sites on the $[\bar{1}10]$-rows of an unreconstructed substrate [121]. However, no quantitative study of this structure is available. The p(2×2)-O structure has also been observed in the present work, but only during coadsorption with sulfur (see section 9).

The most reproducible structures reported by almost all authors are the (1×1) and the c(2×2) configurations. Quantitative studies have shown that the (1×1) structure corresponds to a metastable, unreconstructed Ir(110) surface stabilized by small amounts of dissociatively chemisorbed oxygen [122, 86, 95, 126, 100]. The first interlayer spacing is contracted by 7.5% according to a LEED I(V) study [122]. The preparation procedure reported by all authors is annealing in an oxygen atmosphere, only the annealing temperatures differ somewhat. Further room-temperature exposure of this surface to oxygen results in an ordered c(2×2) pattern [123]. Alternatively, the sample can be cooled down in an O_2-atmosphere after annealing [2, 121, 124, 125] or annealed in a CO-atmosphere [2] to yield the c(2×2) pattern. The latter procedure was interpreted as due to dissociation of the adsorbed CO and the formation of a c(2×2)-O overlayer [2]. The structural model proposed by LEED I(V) measurements [123] shows oxygen atoms over short-bridge sites of the close-packed [$\bar{1}$10]-rows, as shown in Fig. 7.1. Increasing the oxygen exposure further, the c(2×2) periodicity is lost and a (1×1) LEED pattern is seen [123].

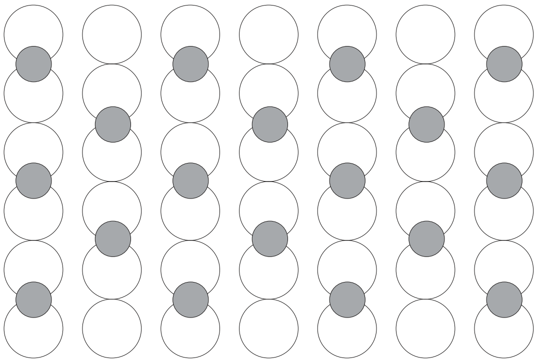

Figure 7.1: Model of the c(2×2)-O structure according to [123]. White circles correspond to Ir atoms (only the first layer is depicted). The oxygen atoms (dark) reside over the short-bridge sites of the close-packed rows, the oxygen coverage is 0.5 ML.

The interlayer spacing between the adsorbate layer and the first substrate layer was determined to 1.37±0.07 Å [123], resulting in an Ir-O bond length of 1.93±0.07 Å and an Ir-O-Ir bond angle of 90°. The topmost substrate interlayer spacing is contracted by 2±5 % compared to the bulk spacing.

7.2 Results of the Present Study

7.2.1 The Oxygen Stabilized Ir(110)-(1×1) Structure

The metastable, unreconstructed Ir(110)-(1×1) structure is reproducibly obtained after exposing the clean, faceted surface to 100 L of O_2 and subsequent annealing in vacuum at 900 K for 10–15 min. Alternatively, heating in an oxygen atmosphere (total pressure 10^{-8} mbar) at 900 K is used while monitoring the LEED pattern. The surface undergoes a change from the faceted to the unreconstructed arrangement within 3 min. The latter method, i.e. annealing in oxygen while observing the LEED pattern, proved to be more reproducible than annealing the oxygen precovered surface in vacuum, because the completion of the transformation is seen directly and the heating and oxygen exposure can be stopped accordingly. Annealing in vacuum after adsorption of oxygen has the disadvantage that in order to get large terrace sizes the annealing temperature has to be sufficiently high. At high temperatures, however, oxygen desorbs and the surface can reconstruct into the faceted structure again if the heating is continued beyond the point of complete desorption. Another disadvantage is the necessity to expose the surface to larger doses of oxygen prior to heating, and thus possible contaminations in the O_2 gas may accumulate. Fig. 7.2 shows the LEED pattern of the unreconstructed surface, the corresponding STM images are seen in Fig. 7.3.

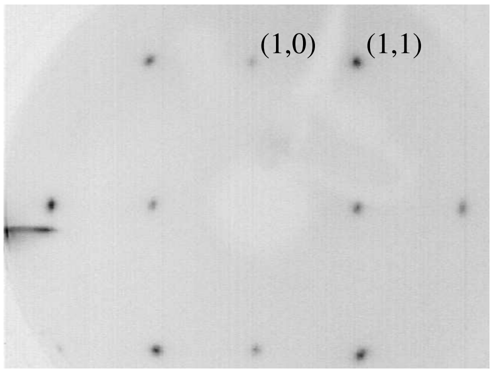

Figure 7.2: (1×1) LEED pattern of the unreconstructed Ir(110) surface, electron energy 89 eV. The dark spike at the left side is due to a defect in the LEED screen.

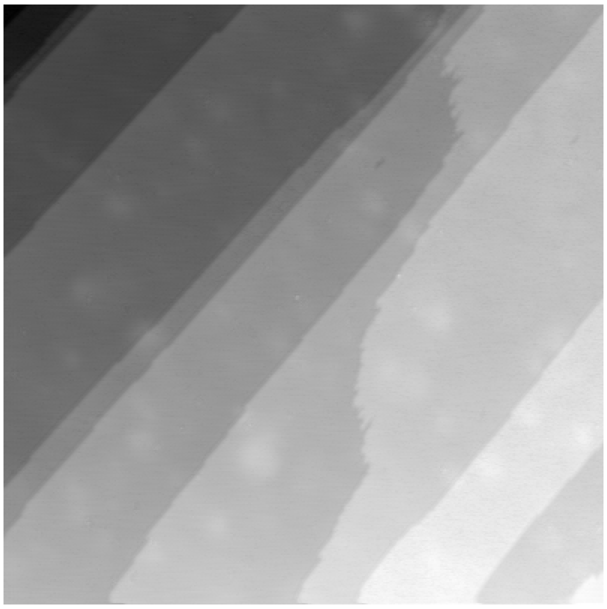

(a)

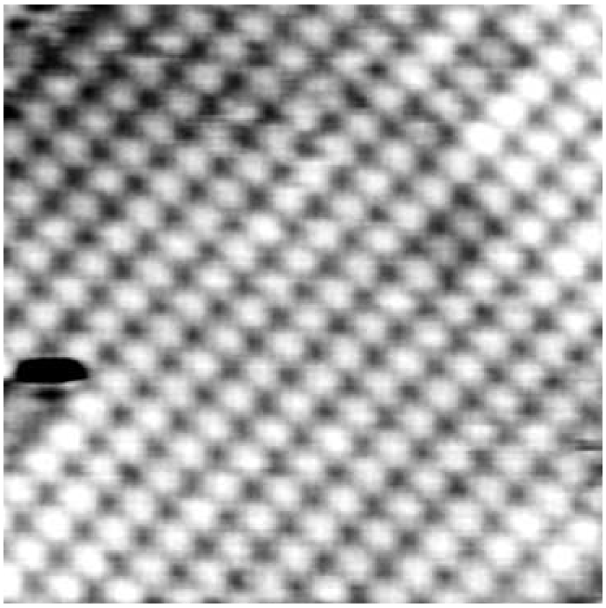

(b)

Figure 7.3: STM images of the Ir(110)-(1×1) surface. (a) (1200 Å)^2 overview showing large terraces instead of the hill and valley structure of the faceted surface (see Fig.6.5), U_t=-900 mV, I_t=0.5 nA. (b) Atomically resolved image, (45 Å)^2, U_t=-900 mV, I_t=1 nA.

As mentioned above, the (1×1) structure converts back to the faceted structure of the clean surface upon annealing and desorption of the oxygen. We find that prolonged annealing (60 min) at only approximately 520 K suffices to restore the facets, indicating a large mass transport even at this comparatively low temperature. At higher temperatures than 520 K the conversion is more rapid and the facet spots become sharper, presumably due to larger domains and better ordering. The oxygen desorption at comparably low temperatures as 520 K may be due to reaction with CO from the residual gas, since from flash-desorption experiments it is known that oxygen desorbs at approximately 900 K from Ir surfaces [121, 127].

As pointed out in the preceding section, we find no evidence for oxide formation under the present experimental conditions. An ordered oxide exhibiting a (1×4) LEED pattern was reported by Weinberg and co-workers, which also was associated with a streaked (1×1) pattern at subsaturation conditions and incomplete ordering [121]. The oxide was reported to contain 0.25 ML of oxygen at saturation, presumably incorporated into the first substrate layer. This oxide was stable up to 1300 K, whereas chemisorbed oxygen desorbs already at 900 K, as stated above. For comparison, the most stable bulk oxide IrO_2 decomposes at 500 K [128]. Since the authors of [121] apparently did not pay special attention to impurities other than C (at least they did not mention it explicitly), it is questionable if the reported "oxide" is indeed oxidized Ir or an oxide of impurities such as Si or Ca. It may be noted that small amounts of Si are especially difficult to detect in AE spectra of Ir, since the Si(92 eV) peak overlaps with the Ir(89 eV) peak. The same problem arises with Si impurities on Pt samples, and the reported Pt "oxides" could indeed be attributed to oxidized Si [16, 17]. The assumption that the reported Ir oxide may also be attributed to oxidized impurities is further strengthened by the observation of Hetterich, who could observe a (1×4) LEED pattern only after oxidizing a Si-contaminated Ir sample, which exhibited a (1×2) pattern prior to oxygen adsorption [125] (we recall that the (1×2) structure was correlated with Si impurities [96]). Similarly, Bu *et al.* have never observed a (1×4) pattern in their experiments [95], indicating the poor reproducibility of this structure.

7.2.2 The Ir(110)-c(2×2)-O Structure

Exposing the unreconstructed surface to further O_2 at room-temperature while monitoring the LEED pattern allows the preparation of a sharp, well ordered c(2×2) oxygen overlayer. Monitoring the LEED pattern during the process is crucial, since an excess amount of oxygen leads to a disordered overlayer with a (1×1) pattern and a high background. It may be noted that the overlayer is not stable for extended periods of time. After an overnight exposure to the residual gas only a (1×1) LEED pattern is left, very likely because the oxygen has reacted with residual CO to form CO_2, a reaction that is catalyzed by Ir [2].

A LEED pattern and STM image of the c(2×2) structure is shown in Fig. 7.4. Stable STM imaging could only be obtained for a complete overlayer or large domains of the structure. At subsaturation coverages [streaked (1/2,1/2) spots in the LEED pattern] the oxygen mobility apparently is too high to allow stable imaging at room temperature. A determination of the binding site is therefore not possible in this case, since for a closed overlayer the substrate is hidden, and below saturation the oxygen mobility is too high.

A way to determine the binding site even at a complete overlayer may be coadsorbing another species whose bonding geometry is known. Knowing the registry between the two adsorbates allows then to determine the binding site of the second adsorbate. Since the bonding geometry of oxygen is known from LEED without ambiguity and no other adsorbate structures on the unreconstructed Ir(110) surface are known, this is not attempted in this work.

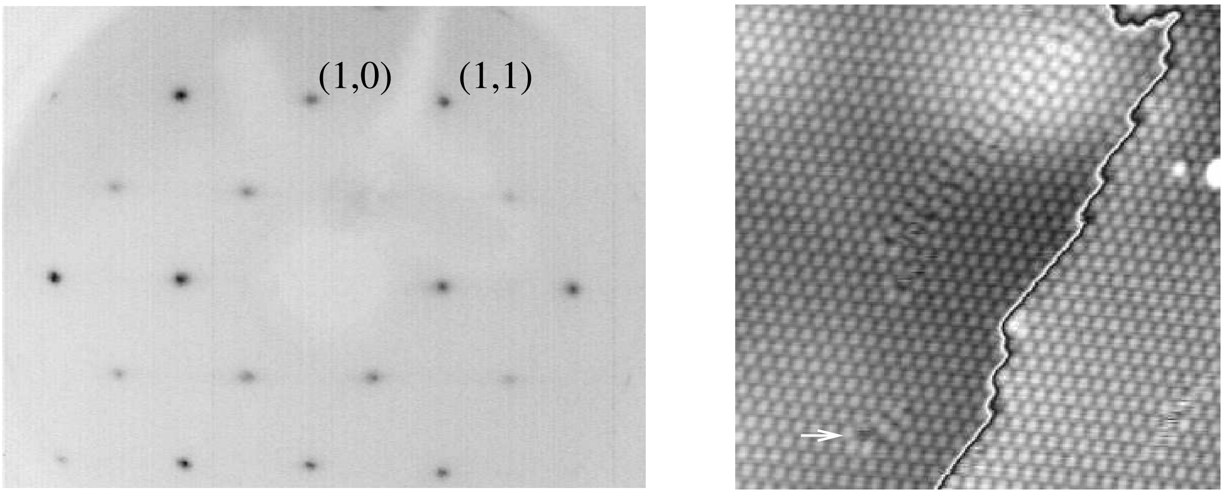

(a) (b)

Figure 7.4: (a) LEED pattern of the Ir(110)-c(2×2)-O structure, electron energy 96 eV. (b) Corresponding STM image, (143 Å)^2, U_t=0.9 V, I_t=2 nA. The oxygen atoms are imaged as protrusions, since defects (arrow) are missing protrusions rather than missing depressions. A monoatomic step with several kinks runs across the image. Two domain boundaries are seen on the lower terrace (left half of the image). Note that the grey scale has been adjusted to show the atomic corrugations of both terraces in similar colours.

According to theory, oxygen should be imaged as a depression in STM images [47, 56]. This has also been observed experimentally for oxygen on several faces of Cu, Ni, and Ag [129], as well as on Al(111) [58]. In the latter experiments a different contrast was observed at low tunneling resistances (around 1 MΩ), where a central protrusion appeared in the depression. At high resistances of $\geq$ 100 MΩ, oxygen was imaged as a depression only. For oxygen on the (110) surfaces of Ni and Cu, a tip-dependent contrast was observed [130]: With a clean tungsten tip the oxygen atoms were imaged as protrusions, whereas with an oxygen atom at the tip apex the substrate atoms were imaged as protrusions and the oxygen appeared as a depression. The STM images of that study were recorded at tunneling resistances of approx. 10 MΩ. A tunneling through some kind of chemical bond between the tip and the adsorbate atom was proposed as origin of the observed contrast, and the theoretical approaches relying on the Tersoff-Hamann theory were assumed to fail at the low resistances used because of the non-negligible tip-sample interactions.

Looking at Fig. 7.4(b), there is evidence that oxygen is imaged as a protrusion: A defect in the overlayer (see mark) can be identified as a missing protrusion, not a missing depression. Hence it follows that the protrusions represent the oxygen atoms and not the regions between them. Furthermore, the distances between the depressions do not correspond to the c(2×2) model, and the oxygen coverage would be 1.0 ML instead of 0.5 ML if the oxygen atoms would correspond to the depressions (each protrusion is surrounded by six depressions, hence there are twice as much depressions than protrusions per unit area). Oxygen atoms were routinely imaged as protrusions, and in fact no clear images could be obtained in which the contrast is reversed. Only some images showed depressions for the oxygen atoms, but those were not considered here because they exhibited double tip effects that make an interpretation difficult.

Since the tunneling resistance used in the present experiments is high (450 MΩ), strong tip-sample interactions can be discarded. Therefore, a chemical bond between the atom at the tip apex and the atoms of the adsorbate layer seems unlikely. Consequently, the reason for the observed contrast remains unclear without the aid of theoretical calculations. Note that interference effects may play an important role for a dense overlayer like the c(2×2) structure.

8 The Adsorption of Sulfur on Ir(110)

8.1 Previous Work

Contrary to sulfur adsorption on other metals [131, 132, 97, 133, 47] the adsorption of sulfur on iridium surfaces has scarcely been investigated. To date, only two LEED publications exist dealing with the structure of sulfur on Ir(110) [134, 7], and one LEED study by about the same authors addresses the structure of sulfur on Ir(111) [135]. At the time of those studies the Ir(110) surface was still considered as (1×2) missing-row reconstructed in the clean state, and it seemed surprising to the authors of [7] that apart from some minor relaxations no influence of sulfur on the structure of the substrate could be detected. When compared to oxygen, which lifts the reconstruction and leads to a bulk truncated (1×1) structure (see chapter 7), this was deemed inconsistent with the simple picture that electronegative adsorbates as oxygen and sulfur should lead to similar effects, namely the lifting of the substrate reconstruction. As will be shown below, this is not puzzling any more based on the results of this work, since small amounts of sulfur actually cause the reconstruction to a (1×2) missing-row configuration. Although this is certainly not a bulk truncated structure, a major influence of sulfur on the substrate reconstruction is obvious. In the following, the results of [134, 7] will be briefly reviewed before addressing the results of the present work.

As in most studies of sulfur adsorption (including the present work), sulfur was deposited on the surface via exposure to H_2S gas. The molecules adsorb dissociatively and H desorbs into the vacuum, as was judged by the LEED I(V) curves, that were identical right after adsorption at room temperature and after subsequent flashing to temperatures of 800–1200 K [134, 135]. Sulfur was not removed from the surface for annealing temperatures below 1600 K.

After low H_2S exposures of up to 4 L (1 L= 1 Langmuir = 1.33×10^{-6} mbar×sec) the LEED pattern showed a (2×2) structure with systematic beam extinctions, which point to a glide plane within the surface unit cell. This structure was stable up to at least 1200 K, and no changes in the I(V) curves were detected. The substrate beams [showing a (1×2) pattern] remained sharp throughout the adsorption, indicating no major structural changes. At higher exposures of 8 L–35 L a diffuse pattern was observed which gradually turned into a c(2×4) with higher background, which could be reduced by subsequent annealing to 950 K. Additional weak streaks were reported that were parallel to the [001] direction and located halfway between the beams in the [$\bar{1}$10] azimuth. However, no structural model for this pattern was developed. For the (2×2) pattern a model was proposed in a dynamical LEED study [7], which corresponds to structure 'A' shown in fig.8.1. In that figure also two other possible structures with a p2mg symmetry ('zig-zag' rows along $[\bar{1}10]$) are shown, consistent with the systematic extinctions of the [1/2(2n+1), 0] beams. In all models the sulfur atoms are located above threefold hollow sites, similar to the adsorption over fcc sites on Ir(111) [135].

The calculations clearly rule out the models 'B' and 'C', which means that sulfur adsorbs also on fcc sites of the (111) facets of the missing-row structure, formed by two first layer substrate atoms and one second layer substrate atom. A slight further improvement was achieved in the theory-experiment agreement by allowing the sulfur atoms to move toward the troughs of the missing rows, without breaking the mirror symmetry. In the final refinement the substrate was allowed to relax in deeper layers, with the adsorbate position held fixed.

The structural parameters of both the Ir(110)-(1×2) missing-row structure and the Ir(110)-(2×2)-2S system are summarized in table 8.1. For a visualization of the substrate relaxations see figure 8.2.

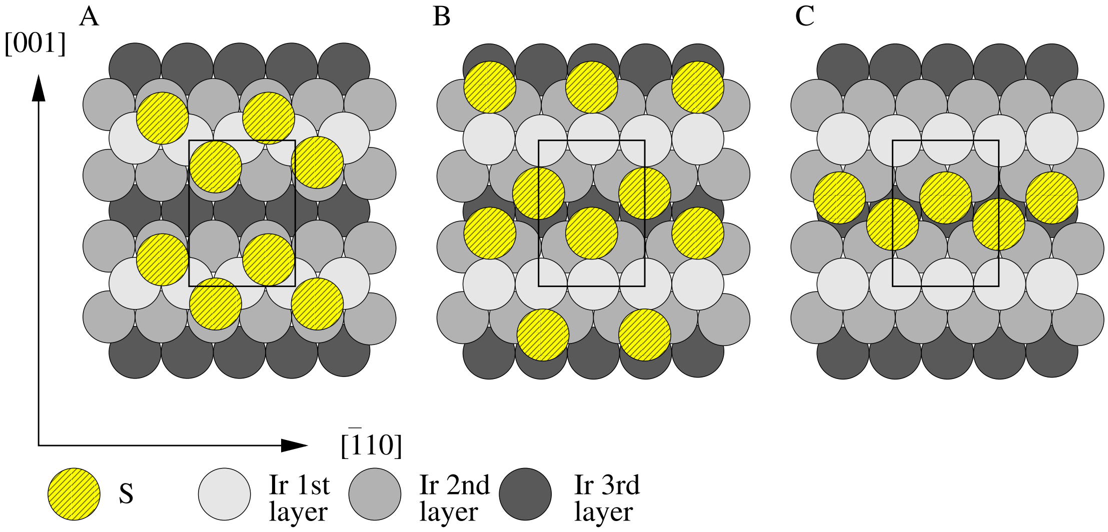

Figure 8.1: Three possible p2mg structures for sulfur adsorbed on Ir(110). The hatched circles correspond to sulfur atoms. A p(2×2) unit cell is indicated.

8.2 Results of the Present Work

8.2.1 Sulfur Induced Structures at Different Coverages

Starting from a clean, annealed Ir(110) surface sulfur is deposited on the sample via backfilling the preparation chamber with H_2S gas. Depending on the desired coverage, the total pressure in the chamber is adjusted in the 10^{-8}–10^{-7} mbar range, and the exposures

parameter	Ir(110)-(2×2)-2S	Ir(110)-(1×2)
d_{12} [Å]	1.3135 (-3.3%)	1.1908 (-12.3%)
d_{23} [Å]	1.3792 (+1.5%)	1.3158 (-3.1%)
d_{34} [Å]	1.3585 (bulk)	1.3951 (+2.7%)
Δy_2 [Å]	0.0	0.0656
Δz_3 [Å]	0.005	0.2294
x [Å]	1.3585	–
y [Å]	1.7230	–
z [Å]	0.9360	–
R_{ave}	0.2905	0.2468
R_P	0.6430	–

Table 8.1: Structural parameters of the (1×2) reconstructed "clean" Ir(110) surface [84] and the Ir(110)-(2×2)-2S structure [7]. The interlayer spacings correspond to center-of-mass planes (see fig.8.2). The values in parentheses give the relaxations with respect to the bulk structure. The parameters x, y, and z indicate the position of one sulfur atom with respect to the nearest Ir atom on the ridge (compare model 'A' in fig. 8.1). The direction of the x-axis is perpendicular to the surface, y is along [001] and z is parallel to the ridges, i.e. in [$\bar{1}$10]. The second sulfur atom in the unit cell is obtained through glide-plane symmetry. R_{ave} means an averaged r-factor [7], R_P is the Pendry r-factor.

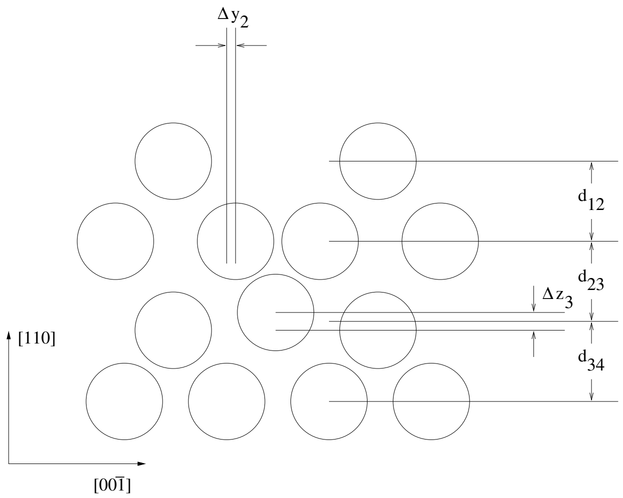

Figure 8.2: Schematical model of a (1×2)-missing-row reconstructed fcc(110) surface. For the parameters see table 8.1. Distances are not to scale. Note the pairing of the second layer atoms and the buckling in the third layer, where the atoms below the troughs of the missing rows move upwards.

are determined using the total pressure readings. At low coverages pressures in the low 10^{-8} mbar range are used, in order to keep exposures reproducible. The error in the exposure can be estimated via the slight change in pressure during the adsorption time, and is assumed to be not higher than ± 0.5 L for exposures below 5 L. For higher exposures higher total pressures are used, and the error may be larger, but this is of no importance since above 5 L only saturation coverages are investigated.

After sulfur adsorption, the surface usually is annealed at 900–1000 K for 10–15 minutes. Depending on the coverage, different LEED patterns are observed (Fig.8.3): After low exposures of approx. 2 L H_2S a (1×2) pattern is observed, additional 2 L lead to a p(2×2) pattern and at 10 L or more the observed symmetry is c(2×4). In the p(2×2) pattern the $[\frac{1}{2}(n+1), 0]$ beams are missing at all energies, which indicates a glide plane symmetry in agreement with the earlier reports [134, 7]. The c(2×4) pattern exhibits additional weak features halfway between the beams in $[\bar{1}10]$-azimuth, indicating a partially ordered structure with four times the nearest neighbor distance in this direction.

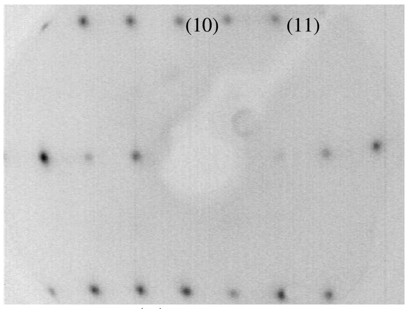

(a) 2 L H_2S

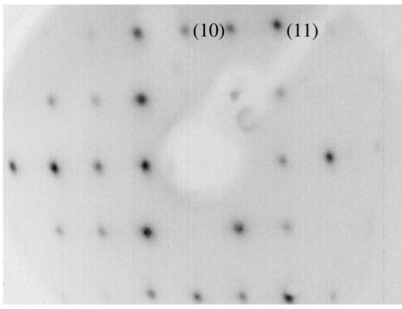

(b) 4 L H_2S

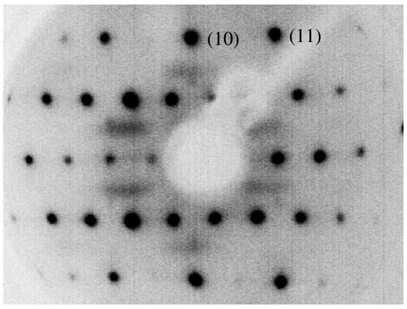

(c) 10 L H_2S

Figure 8.3: LEED pattern of the annealed S/Ir(110) surface at different coverages. (a) (1×2) pattern after low H_2S exposures, electron energy 72 eV. (b) p(2×2) pattern after 4 L exposure (75 eV). Note the missing (±1/2, 0) beams. (c) c(2×4) pattern at saturation coverage (89 eV). The contrast is enhanced to show the diffuse extra spots at 1/4 positions in the $[\bar{1}10]$ azimuth.

The STM reveals the local atomic arrangements of the different structures. After low exposures of approx. 2 L usually a somewhat "noisy" missing-row structure is seen [Fig.8.4(a)]. At some positions in the image single atoms are visible, but in general no atomic resolution along the $[\bar{1}10]$ rows is obtained, and the sulfur is hardly ever resolved. The noise is not present on clean parts of the surface, which exhibit a clearly resolved (1×2) missing-row structure of the substrate [Fig.8.4(b)]. In this respect it is interesting to note that the (1×2) reconstruction of Ir(110) is *not* accompanied by the fish-scale pattern, which was observed on the (1×2) reconstructed Pt(110) and Au(110) surfaces (see also section 6.2.1). The fish-scale pattern was formed on the latter in order to avoid (331) faceted steps, a step type that is, in contrast, *exclusively* formed on clean Ir(110). Indeed, also on the (1×2) reconstructed Ir(110) surface (331) steps are frequently observed, which indicates that there is no preference to form (111) faceted steps on this surface and hence no need to form the fish-scale pattern.

The noise in Fig.8.4(a) may be due to a high mobility of the adsorbate and/or the fact that the sulfur atoms have not yet coalesced to form larger islands (it is clearly not due to usual noise in the tunneling current, since it is restricted to the ridges of the missing-row structures in most images). This is a general problem in STM imaging of adsorbates at subsaturation coverages, and may be circumvented either by cooling the sample (which was not possible in the present experiments) or by coadsorbing another species which can lead to a phase separation of the competing adsorbates. The latter has been shown e.g. for

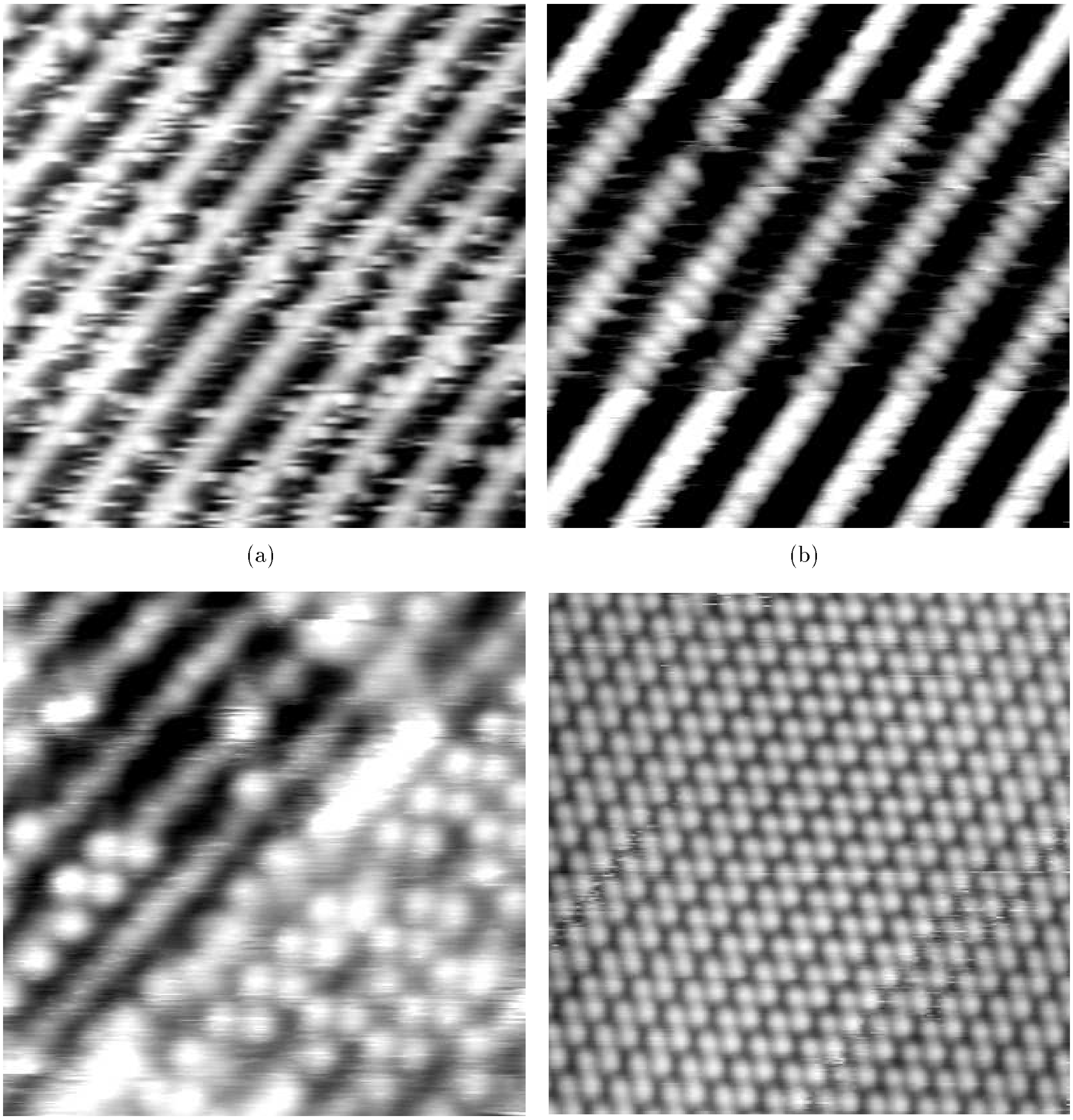

(a) (b)

(c) (d)

Figure 8.4: STM images of the missing-row reconstructed surface with varying sulfur coverage. (a) Noisy image, possibly due to mobile sulfur. Some sulfur atoms are visible, (65 Å)^2 U_t=-50 mV, I_t=15 nA. (b) Clean part of the surface with resolved missing-row structure. Two tip changes during the image acquisition led to the appearance and disappearance of (clear) atomic resolution, (50 Å)^2, U_t=-20 mV, I_t=15 nA. (c) Coalesced S-domains after coadsorption of O_2, (60 Å)^2, U_t=-100 mV, I_t=2 nA. The S atoms apparently adsorb at the sides of the [$\bar{1}$10]-rows (see text). (d) p(2×2)-2S structure, compare model 'A' in Fig. 8.1. (90 Å)^2, U_t=900 mV, I_t=1 nA.

CO/S/Ni(110) and CO/O/Ni(110) [136]. Also CO is known to compress adsorbed sulfur into structures of higher local coverage on Pt(111) and Re(0001) [137, 138].

Coadsorption of O_2 with S is also investigated in the present study, and will be detailed in chapter 9. Oxygen coadsorption leads to a compression of the S-layer and the sulfur atoms coalesce to larger domains. A representative STM image obtained after exposing a S-precovered surface (H_2S exposure approx. 2L) to several L of O_2 is shown in Fig.8.4(c). Small sulfur clusters can be resolved which exhibit a zig-zag arrangement. The regions between the S-domains are mostly free of oxygen, which at low coverages adopts a p(2×2) configuration with no glide-plane symmetry on a missing-row reconstructed Ir(110) surface [2] (see also section 9). The sulfur adsorption site, although it cannot be exactly determined because of the lack of resolution of the substrate rows, is compatible with the LEED results [7] which found an adsorption over the fcc sites of the (111) microfacets of the missing-rows, i.e. at the "sides" of the rows as seen in the figure. Adsorption on top of the [$\bar{1}$10]-rows or in the troughs between them can be excluded from the STM images.

At higher coverages the sulfur domains coalesce to form a closed overlayer of p(2×2) symmetry [Fig. 8.4(d)]. The zig-zag arrangement indicates a glide-plane parallel to the [$\bar{1}$10]-direction, in agreement with the systematic extinctions of the [$\frac{1}{2}$(2n+1), 0] beams in the LEED pattern. In a LEED study several possible models with p2mg symmetry or a model with p1g1 symmetry with equal domain sizes leading to this extinctions were proposed [134]. In the STM images only one domain-type is found, so that the p1g1 model can be ruled out. Of the three possible p2mg models (see Fig. 8.1), only model 'A' is compatible with the data, judging from the separation of the sulfur atoms in [001] direction in the STM image. In model 'B' the S-atoms are nearer to the troughs of the missing-rows, which is clearly not the case as seen in the low-coverage image of Fig. 8.4(c). Model 'C' can be ruled out for the same reasons, and moreover the width of the zig-zag rows in [001] direction in this model is smaller than seen by STM. In the LEED study [7] a slight improvement in the fit was found when the sulfur atoms are allowed to relax toward the troughs in model 'A'. Judging from high-resolution STM measurements like the one in Fig. 8.4(d), this statement seems questionable, as will be discussed in detail in the next section (chap. 8.2.2).

According to the model the sulfur coverage is 0.5 ML for the p(2×2) structure. At higher coverages a c(2×4) LEED pattern is observed [see Fig. 8.3(c)], for which no structural model was proposed so far. STM images of that structure, prepared by adsorbing additional sulfur on the p(2×2)-2S structure and subsequent annealing to 900 K for several minutes are shown in Fig. 8.5. In Fig. 8.5(a) a small area is seen with zig-zag rows as for the p(2×2) structure, but now they are in antiphase, so that the neighboring sulfur atoms of two adjacent zig-zag rows form a square-shaped arrangement. Closer inspection of the topography reveals that the atoms in these squares are not always equivalent, since some seem to protude above the others, as is seen in the lower right part of the image. Sections along the [$\bar{1}$10] direction reveal a height difference of approx. 0.4 Å. The protruding atoms form dimers at every four lattice spacings in [$\bar{1}$10] direction. At saturation coverage the surface is completely covered by these protruding dimers [Fig. 8.5(b),(c)], which give rise to the additional streaks in the LEED pattern.

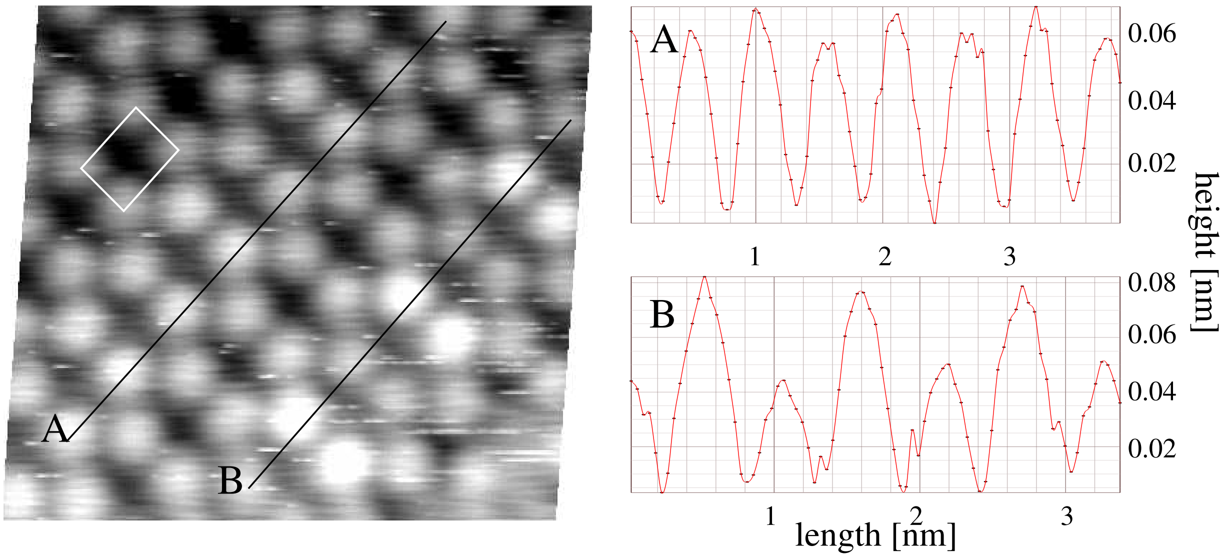

(a)

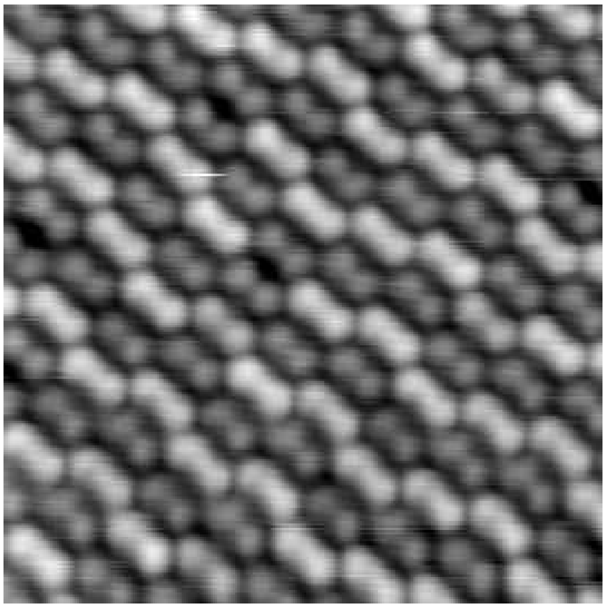

(b)

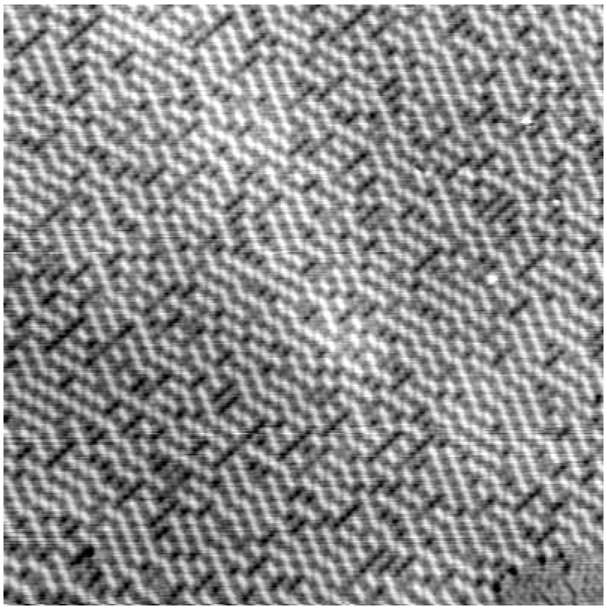

(c)

Figure 8.5: STM images of the c(2×4) structure. (a) Small area at subsaturation coverage. Zig-zag rows in out-of-phase condition are seen. Note that the protruding dimers in the lower right corner are absent in the upper left area (compare also the sections A and B: the height difference in B is approx. 0.4 Å). (37×35 Å)^2, U_t=-900 mV, I_t=0.1 nA. (b) The surface at saturation coverage. The protruding dimers now cover the whole area. (67 Å)^2, U_t=-10 mV, I_t=3 nA. (c) Overview image of the surface near saturation showing the long-range ordering of the dimers. (389 Å)^2, U_t=-900 mV, I_t=0.5 nA.

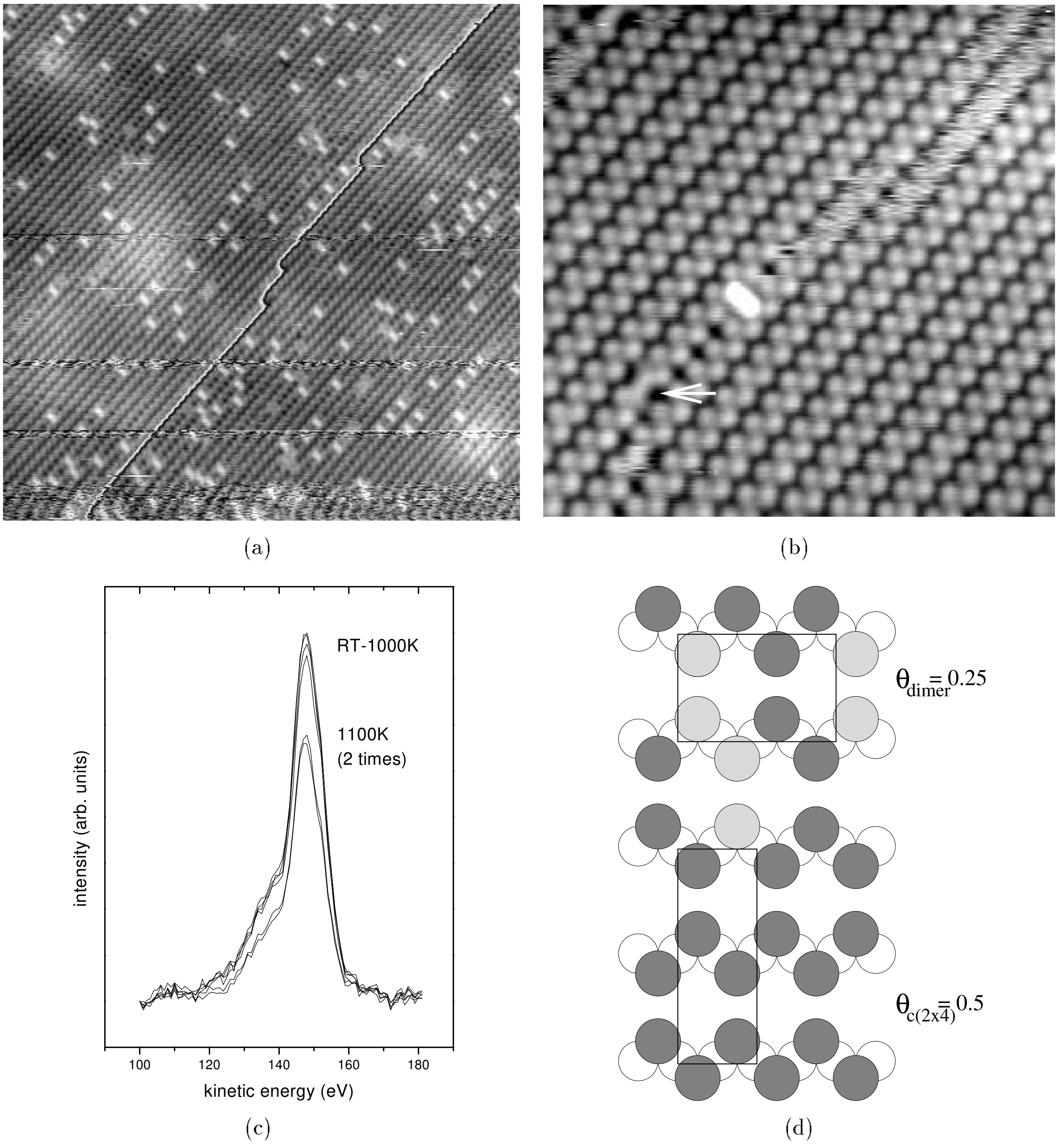

Figure 8.6: The c(2×4) structure after annealing to 1100 K. (a) Overview STM image, (382 Å)^2, U_t=900 mV, I_t=1 nA. The greyscale is adjusted for better contrast of the two terraces. Only a few dimers are left, and most of the zig-zag rows are in phase again in a p(2×2) configuration. (b) A single dimer on a local c(2×4) domain. The arrow mark a position where an additional sulfur atom is incorporated, (100 Å)^2, U_t=-900 mV, I_t=1 nA. (c) AE-spectra of the sulfur peak after annealing the saturated c(2×4) structure at different temperatures. A spectrum of the clean surface was subtracted from each of the orignial N(E)-spectra to yield the sulfur signal only. No significant sulfur loss is seen below 1000 K. At 1100 K the signal decreases markedly, and the LEED pattern changes to p(2×2). A second anneal at 1100 K leads to no further decrease. The ratio of the areas under the curves is 1.5, consistent with a coverage of 0.5 ML and 0.75 ML for the p(2×2) and c(2×4) structure, respectively. (d) Resulting model of the c(2×4) structure. Only the topmost substrate rows (white) and the sulfur atoms (light and dark grey) are shown. A second adsorbate layer composed of sulfur dimers (light grey) is depicted in the upper half. Due to the on-top adsorption over first layer sulfur atoms, the dimers show long-range order in the $[\bar{1}10]$ direction only. The total sulfur coverage of the c(2×4) structure with a complete dimer overlayer is 0.75 ML at saturation.

Heating the c(2×4) structure to 1100 K results in a p(2×2) LEED pattern and a significant decrease in the number of the protruding dimers in the STM images (Fig. 8.6). The sulfur signal in the AE-spectrum is lower, too, indicating desorption of sulfur [Fig. 8.6(c)]. One can conclude that the dimers actually reside in a second layer in on-top positions over sulfur atoms of the first adsorbate layer. The apparent height of approx. 0.4 Å of the dimers seen in Fig. 8.5(b) is clearly less than an atomic step height (approx. 1.4 Å), but is in good agreement with experimental findings for S on Ni(100), where the S atoms appeared to be approximately 0.4 Å high [47]. This further corroborates the assumption that the protruding dimers are indeed due to additional second layer sulfur and not due to a buckling or an electronic effect of the first layer sulfur. The on-top position of the dimer atoms also explains the lack of long-range order in the [001] direction: Along this direction, two adjacent dimers must shift by a nearest-neighbor distance in the $[\bar{1}10]$ direction to be located in on-top positions. Apparently, the next-nearest dimer in the [001] direction has no influence on the position in this direction, so that the dimer positions in $[\bar{1}10]$ shift randomly by a lattice spacing, resulting in 'meandering' bands of dimers as seen in Fig. 8.5(c).

The proposed model for the c(2×4) structure is depicted in Fig. 8.6(d). When the surface is covered by the additional dimers, the coverage is 0.75 ML at saturation. This is in good agreement with the AE signal of Fig. 8.6(c): Comparing the area under the sulfur peaks of the c(2×4) structure (before annealing) and of the p(2×2) structure (after annealing at 1100 K), one finds a ratio of 1.5, which is in very good agreement with the models of the two structures. Strictly speaking, the ratio should be a little lower, since the c(2×4) structure is a bilayer structure, and a part of the sulfur signal from the first layer is attenuated due to the dimer atoms. However, as will be shown in section 8.2.4, the deviation is only small here, and so the c(2×4) structure can be used as a standard for calibrating sulfur coverages. The advantage over the p(2×2) structure may be that saturation coverages can easily and safely be reproduced with virtually no uncertainty, which is not so for the p(2×2) structure, because a sharp LEED pattern may already be observed below a coverage of 0.5 ML, and STM probes the surface on a far too local scale to give an accurate estimate of the total coverage.

The fact that the c(2×4) structure is stabilized by the dimers (large domains are never observed without dimers being present) also explains why the dimers have a minimum separation of four lattice spacings in $[\bar{1}10]$ direction. If they were closer, the second layer sulfur would locally have the same structure as the first layer sulfur, i.e. a c(2×4). Since the sulfur atoms in the center squares of this structure approach quite closely, this situation may not be stable without further stabilizing atoms in a third layer. Apparently a third sulfur layer is also not favorable, maybe because the bonding to the metal is too weak, and sulfur-sulfur bonds are not formed.

The conversion mechanism between the p(2×2) and the c(2×4) structure can either be a shift of a zig-zag row by a nearest neighbor distance in the $[\bar{1}10]$ direction, possibly accomplished by the additional sulfur atoms occasionally seen at positions where such a shift can directly be observed (see marks in Fig. 8.7), or by a mechanism that involves no mass transport along $[\bar{1}10]$ at all: A 'flip' of every other row around the $[\bar{1}10]$ axis along the ridges of the missing-row structure (i.e. the row - not the whole surface - is mirrored at a plane normal to the surface and along this axis). This requires an intermediate adsorption site above the ridges, possibly a short-bridge site, so that the sulfur atoms 'climb' the ridges to descend to fcc positions on the other side again.

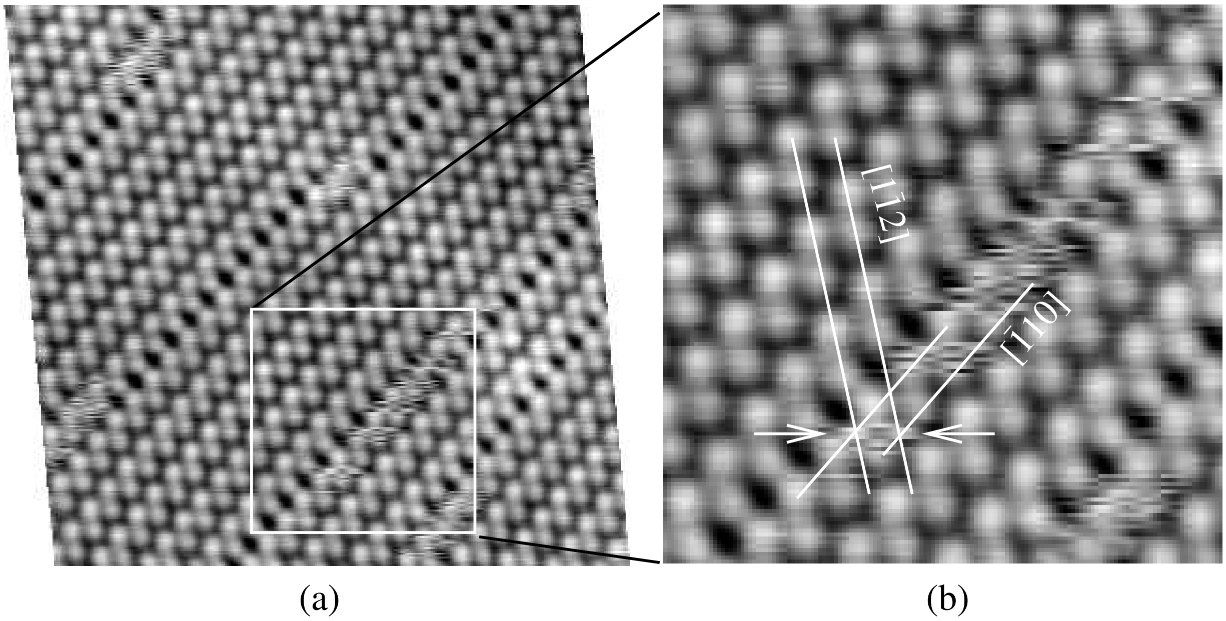

Figure 8.7: STM image of the onset of the c(2×4) formation, (120 Å)^2, U_t=500 mV, I_t=1 nA. Only a few c(2×4) domains are seen. Note the noise at the indicated positions where a p(2×2) → c(2×4) conversion is located. The magnified part in (b) shows that the noise is due to mobile sulfur atoms which can be imaged at intermediate positions (arrow) for a few line scans. The positions can be identified as fcc sites indicated by the lines along [1$\bar{1}$2] and the fact that they are aligned with the other atoms in [$\bar{1}$10].

In this respect it is interesting to look at the 'flicker noise' that is observed in STM images along the rows at positions where a domain shift is present. This flicker noise is always observed at such positions, and can be quite clearly seen in Fig. 8.7 [but also in the region in [$\bar{1}$10] direction above the single dimer in Fig. 8.6(b)]. The figure corresponds to the onset of a c(2×4) structure, since the sulfur coverage is higher than 0.5 ML but well below saturation. On other parts of the surface (not shown) already some dimers exist on the c(2×4) parts, but the overall surface still shows a p(2×2) symmetry, indicated by the LEED pattern. In the figure, most clearly in the magnified part, sulfur atoms in intermediate positions are imaged, which are seen only for a few line scans. Such flicker noise can be attributed to mobile atoms diffusing under the tip. If diffusion is fast, the noise at first sight is distributed randomly, and atoms are imaged for one or two line scans only. But as was shown for S on Re(0001), the noise can be correlated and a local ordering can be observed [139]. In the present case, the noisy domains are too small to allow a correlation, but it is not necessary to do this anyway: The intermediate positions are sometimes imaged for more than two subsequent line scans and thus can be identified directly. They are aligned in the [$\bar{1}$10] direction with the other atoms in the row, which indicates an adsorption at the sides of the ridges. Drawing lines along the [$1\bar{1}2$] direction across the S atoms of the surrounding p(2×2) domain then shows that the intermediate positions lie exactly on these lines (see the magnified part of Fig. 8.7 for clarity). This means that the intermediate positions are lattice positions, namely fcc sites. They represent the positions where the S atoms normally would be located if no c(2×4) domain was present and if the p(2×2) part extended over the whole image. So it seems that the S atoms switch between two adjacent fcc sites without crossing the ridges.

What does this imply for the conversion mechanism? Since the intermediate positions are fcc sites and not on-top or bridge sites, one may tentatively assume that the conversion mechanism does not involve such sites, but rather is accomplished by motion of S atoms along [$\bar{1}10$]. This can also be regarded as more favorable in terms of coordination number: A diffusion from one fcc site to another may be facilitated via an intermediate hcp site (i.e., at the side of the facets but with a bond to only one first layer Ir atom and two second layer Ir atoms, compare model 'B' in Fig. 8.1), which means that the coordination number for the S atoms with respect to the Ir substrate is always three, whereas a crossing of the ridges would involve lower coordinated sites. However, no final conclusion can be drawn here, since one would need a theoretical modelling of the possible conversion pathways to compare the energies. Also the situation may be much more complicated than assumed so far, since obviously second layer sulfur is needed to stabilize larger c(2×4) domains. In how far this sulfur is involved in the conversion mechanism is not clear. Also the fact that clear a c(2×4) LEED pattern is only observed after moderate annealing indicates an activated process, possibly with a complex intermediate structure.

8.2.2 The Ir(110)-p(2×2)-2S Structure: STM vs. LEED

In this section, the possible relaxations of S found in a previous LEED study will be discussed from the standpoint of STM. Regarding the model and adsorption site, STM and LEED agree nicely, as shown in the preceding section. In the LEED study of the p(2×2)-2S structure a (slight) improvement of the experiment/theory agreement was found by allowing the sulfur atoms to relax toward the troughs while keeping the mirror symmetry [7]. This is depicted in Fig. 8.8(a). The short arrows at the atoms S1 and S3 indicate the direction of the relaxations, when moving from a site directly centered over the threefold fcc hollow site toward an off-center position. Thereby, the sulfur-sulfur spacing across the ridges [the distance $\overline{S3S5}$ in Fig. 8.8(a)] is increased, while the sulfur-sulfur spacing across the troughs ($\overline{S1S3}$) is reduced. The local directions $\overrightarrow{S1S3}$ and $\overrightarrow{S3S5}$, which 'zig-zag' around the [$\bar{1}12$] direction [long arrows in Fig. 8.8(a)], are thus slightly more aligned along that direction.

In principle, high-resolution STM images should allow to detect these differences, if they are not too small. Of course, care has to be taken when doing so: Since STM does not image the atom cores, it is not capable of assigning three-dimensional coordinates to the atoms in a unit cell as is possible by LEED. But, given that no interference effects are present that could give rise to 'artifacts' like contrast reversal (see chap. 3.3), i.e. if it can be assumed that the simplifying rule 'bump=atom' holds, STM *is* capable of assigning in-

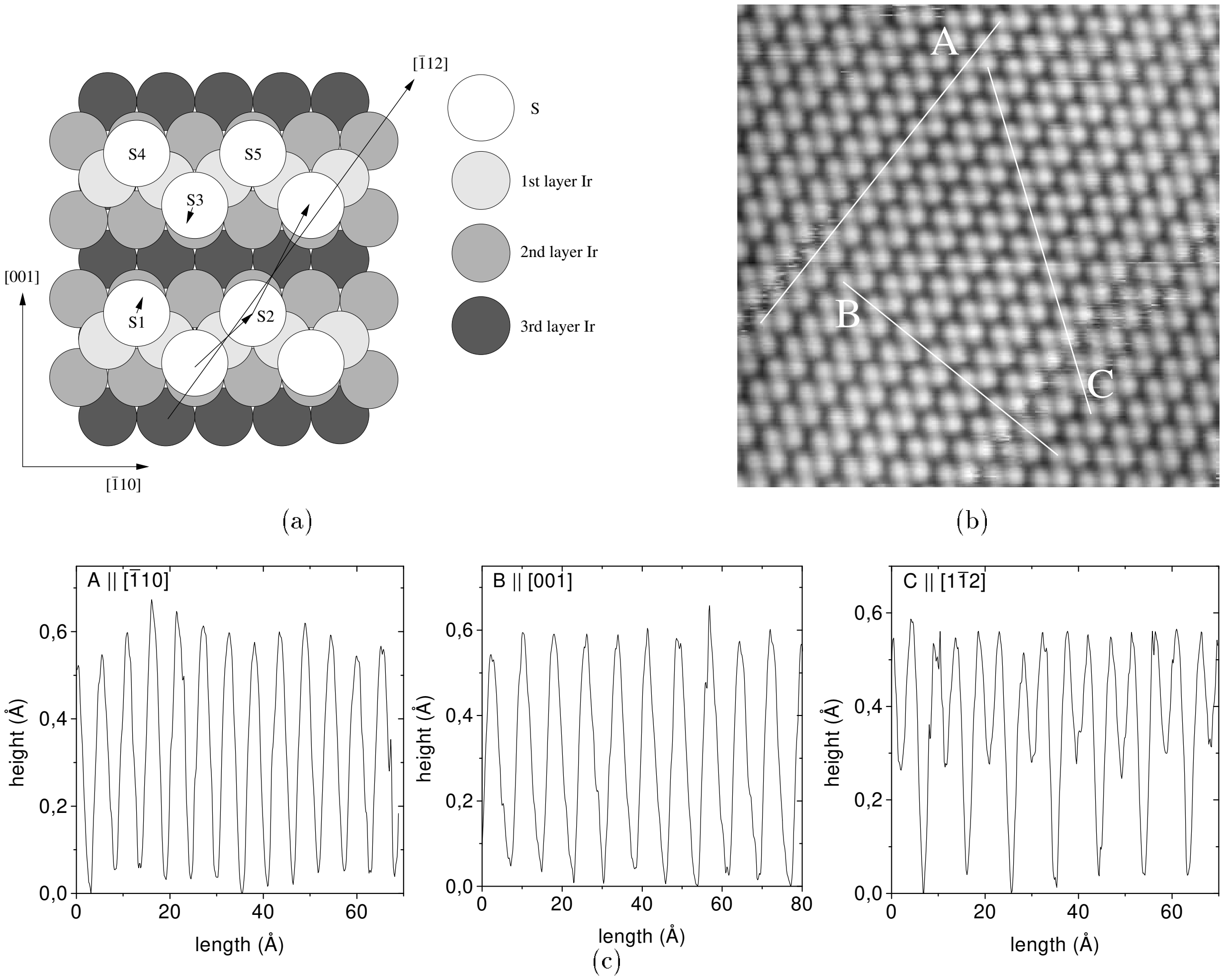

Figure 8.8: (a) Model of the p(2×2)-2S structure. The short arrows at the atoms S1 and S3 indicate the off-center relaxation toward the troughs found by LEED [7]. Note that the local directions from one sulfur atom to another (long arrows) are alternately tilted against the [$\bar{1}$12] direction, which is the mean direction of the sulfur atoms across the ridges/troughs [compare also (b)]. (b) STM image of the p(2×2)-2S structure, (95 Å)^2, U_t=900 mV, I_t=1 nA. Typical sections along the indicated directions ('A' corresponds to [$\bar{1}$10], 'B' to [001], and 'C' is along [1$\bar{1}$2]) are shown in (c). For the measured atom spacings along these directions see table 8.2 below.

plane coordinates to the atoms. By in-plane coordinates is meant the coordinates projected onto the substrate plane. Using the coordinates and bond lengths determined by LEED [7], the sulfur-sulfur spacings for the unrelaxed configuration are calculated to 5.19 Å and 4.21 Å for $\overline{S1S3}$ and $\overline{S3S5}$, respectively. For the relaxed structure, the spacings are $\overline{S1S3}$=5.00 Å and $\overline{S3S5}$=4.40 Å. In the present case, the projected spacings are the same as the three-dimensional distances, since all sulfur atoms are equivalent, i.e. they have the same height above the substrate for the p(2×2) structure. Since the sulfur atoms are not exactly aligned along the [1$\bar{1}$2] direction, a projection onto this direction is necessary since the STM height sections are parallel to [1$\bar{1}$2]. However, since the tilt angle with respect to $[1\bar{1}2]$ is only a few degrees, the correction is very small (0.01–0.02 Å) and practically unimportant. Nevertheless, it has been included in the analysis, and the quoted values are already projected on the $[1\bar{1}2]$ direction.

section	number of values	exp. mean [Å]	stdev [Å]	LEED (unrel.) [Å]	LEED (rel.) [Å]
$\overline{S3S5}$	833	4.25	0.22	4.21	4.40
$\overline{S1S3}$	833	5.27	0.22	5.19	5.00
$\overline{S1S2}$	365	5.47	0.23	5.43	5.43
$\overline{S1S4}$	160	7.70	0.40	7.68	7.68

Table 8.2: Experimental values for several sulfur-sulfur spacings (projected onto the (110) plane) obtained by LEED and STM [see the model in Fig. 8.8(a)]. For the STM values the number of evaluated spacings, the mean value and the standard deviation is given. The LEED values correspond to the unrelaxed position with sulfur atoms centered over the fcc-sites of the missing-row facets (calculated using a bond length of 2.3085 Å of the S atom to the nearest Ir atom [7]), and to the relaxed position where the atoms are allowed to move off-center toward the troughs (the 3-dimensional coordinates are given in table 8.1).

To obtain the sulfur-sulfur spacings along the $[1\bar{1}2]$ direction, several height sections like the one shown in Fig. 8.8(c) (section 'C') are taken and evaluated. The section in the figure seems to show two different separations, judging from the alternating deep and shallow minima. However, this could also be due to the fact that the shallow minima are observed across the ridges [$\overline{S3S5}$ in Fig. 8.8(a)], and the deep minima are observed between the atoms across the troughs ($\overline{S1S3}$). The alternating presence and absence of a substrate row between the sulfur atoms could also be the reason for alternating minima, without the sulfur-sulfur spacings being different. A quantitative evaluation of a number of sections is therefore necessary to obtain a reliable measure. About forty sections along the $[\bar{1}12]$ and the $[1\bar{1}2]$ directions have been evaluated, and another twenty sections along the $[\bar{1}10]$ and the [001] directions, respectively, are taken to assure the correct calibration of the image. The results are listed in table 8.2. The procedure is repeated with an independent set of data, which nearly exactly (within 0.03 Å) reproduces the mean values found for the first set. The two sulfur-sulfur separations are 5.27±0.22 Å and 4.25±0.22 Å, respectively (the error limits correspond to the standard deviation; using interpolated splines instead of raw data for the evaluation may reduce the error bars, since the noise in the raw data leads to fluctuations of the separation of two maxima in the height sections, hence increasing the standard deviation). This is in good agreement with the values expected for the unrelaxed structure. Regarding the error limits and a small deviation of the mean values in $[\bar{1}10]$ and [001] direction from the expected ones, the relaxations found by LEED cannot be safely excluded. But the fact that the mean values of two independent data sets are nearly identical and agree well with the calculated values for the unrelaxed structure, justifies the assumption that the LEED result can be questioned.

It is not claimed, however, that STM is superior to LEED in determining the (lateral) atomic coordinates within a unit cell, which is clearly not the case for several reasons, one of them (and maybe the least) being the comparably large error bars for the STM values. But when, as in the present case, the improvement in the fit between two different structures is only marginal in a LEED study, STM can aid to test its significance. For suitable systems like the one studied here, this could be a way of avoiding a 'numerical trap', where a structure is believed to be superior to another just because the r-factor is lower in the third digit.

8.2.3 Image Artifacts

As already mentioned in section 3.3, several 'artifacts' can be observed in STM images of dense adsorbate layers. The observed phenomena like, for example, contrast inversion, can be explained by special tip configurations and interference effects between tunneling contributions from different adsorbate atoms.

In the case of sulfur on Ir(110), two such effects have been repeatedly observed, and are thus believed to represent tip configurations that occur often in the experiment. The first 'artifact' is the non-equivalence of the sulfur atoms in the p(2×2)-2S structure [Fig. 8.9(a)]. The image, if taken for granted, would imply a p(2×2) unit cell *without* a glide-plane, since the heights of the two sulfur atoms in the unit cell are different and they cannot be considered as equivalent. Such an effect has also been observed for CO on Ni(110), which exhibits a (2×1) unit cell with glide-plane symmetry [140].

The second effect is the appearance of sulfur trimers instead of dimers for the c(2×4) structure [Fig. 8.9(b)]. In this image an apparent third atom is located between the atoms of the dimer, and this protrusion is usually imaged slightly lower than the dimer atoms. Also, the sulfur atoms are imaged much smaller in these images. That the additional protrusions do not represent sulfur atoms is clear from the AES results [Fig. 8.6(c)], since the saturation coverage would then be 0.875 ML for the c(2×4) structure, which is inconsistent with the p(2×2) model regarding the intensity ratios of the c(2×4) and p(2×2) spectra. Furthermore it can be clearly seen in other images like Fig. 8.5(a), that the bright protrusions in this structure are formed by dimers, not trimers. Regarding the apparent complex structure, also of the zig-zag rows in the first adsorbate layer, it must be concluded that images like Fig. 8.9(b) contain a high degree of non-topographical information, and are not suited for a straightforward interpretation.

The origin of these artifacts is not clear. The first effect, the apparent breaking of the glide-plane symmetry, is often observed when coadsorbing oxygen on the surface, and may be attributed to an oxygen tip. The second effect is in most cases observed for low tunneling resistances (16–100 MΩ), but sometimes also for high resistances of 900 MΩ. An effect of the tunneling polarity could not be detected. It is therefore not clear if the observed contrast is due to electronic effects or a different tip configuration. A double tip may be ruled out as cause, since the atoms do not appear to be doubled. Electronic effects may play a role, since at different gap resistances different electronic states of the surface may be imaged. But these assumptions must remain speculative at the present stage.

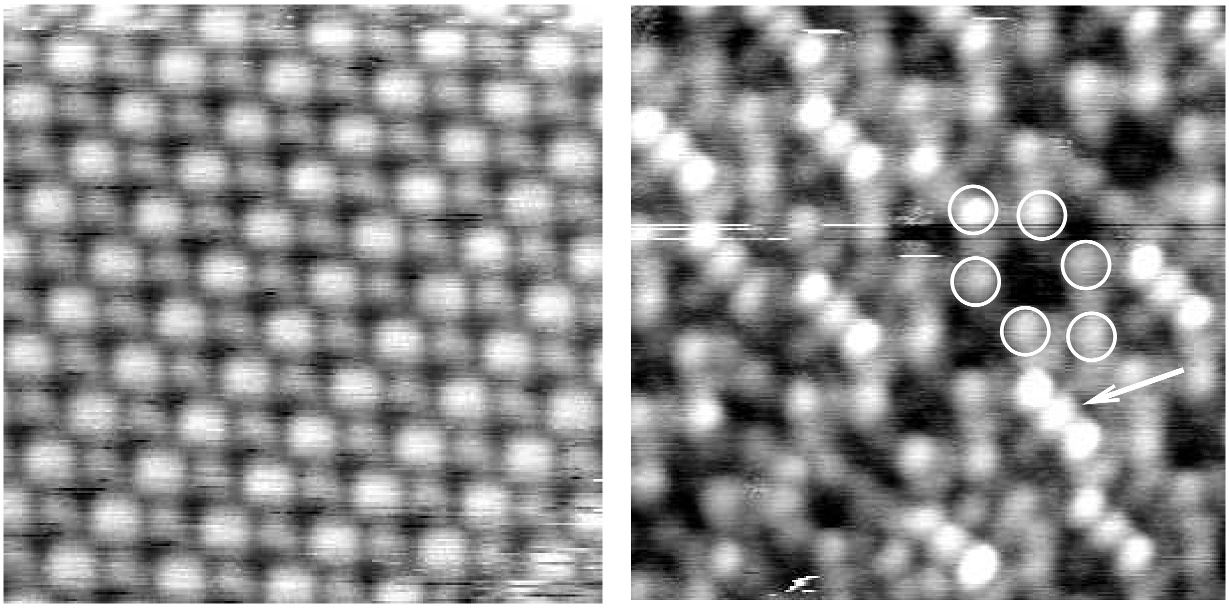

Figure 8.9: (a) The Ir(110)-p(2×2)-2S structure with apparently non-equivalent sulfur atoms, inconsistent with the glide-plane symmetry. (53 Å)^2, U_t=-1.5 V, I_t=0.5 nA. (b) Apparent trimers instead of dimers for the c(2×4) structure. The protrusion (arrow) between the bright dimer atoms does not represent an additional atom. Some sulfur atoms in the zig-zag rows are marked for clarity. (39 Å)^2, U_t=-500 mV, I_t=1 nA.

8.2.4 AES Results: Lineshape and Sulfur Coverage

As already mentioned in section 8.2, the c(2×4)-6S structure may be used as a calibration standard for sulfur coverages on Ir(110). It is therefore interesting to compare the coverages derived by this model with the coverages derived by equations 5.10 and 5.12. To be a suitable calibration standard also in the usual derivative mode, it must be assured that the AES lineshape remains constant for all coverages, since otherwise the area under the sulfur peak in the N(E) spectrum changes in a different way than the peak-to-peak ratio in the dN(E)/dE spectrum.

A series of Auger spectra with increasing coverage can be seen in Fig. 8.10. The spectra show the sulfur signal only, i.e. a spectrum of the clean surface has been subtracted from all spectra after normalization to the Ir(230 eV) peak. It can be seen that after approximately 10 L exposure the surface is saturated. Further exposure to 90 L does not significantly increase the intensity of the sulfur signal. For low coverages, the spectrum of the clean surface is shown for comparison in Fig.8.12. In that figure, also the differentiated dN(E)/dE signals are given. Note that there are two features arising in the spectrum upon sulfur adsorption: A shoulder at the low-energy side of the Ir(154 eV) peak and an increase in intensity of the latter. This can be seen more clearly in the differentiated signal, where a second peak at 149 eV is clearly resolved. The question is, if the two peaks associated with sulfur are due to different bonding or some other mechanism. Closer inspection of the

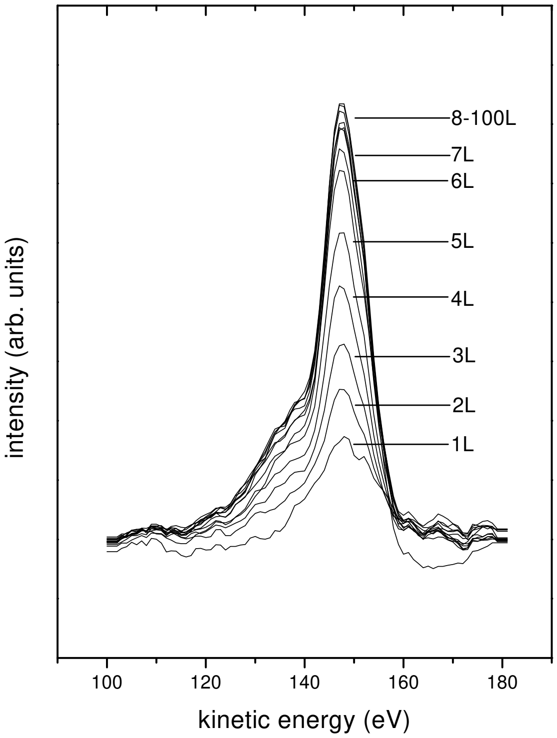

Figure 8.10: Sulfur AE spectra for increasing H_2S exposure. A spectrum from clean Ir(110) was subtracted from each of the curves to obtain the sulfur signal only. The surface saturates at approximately 10 L.

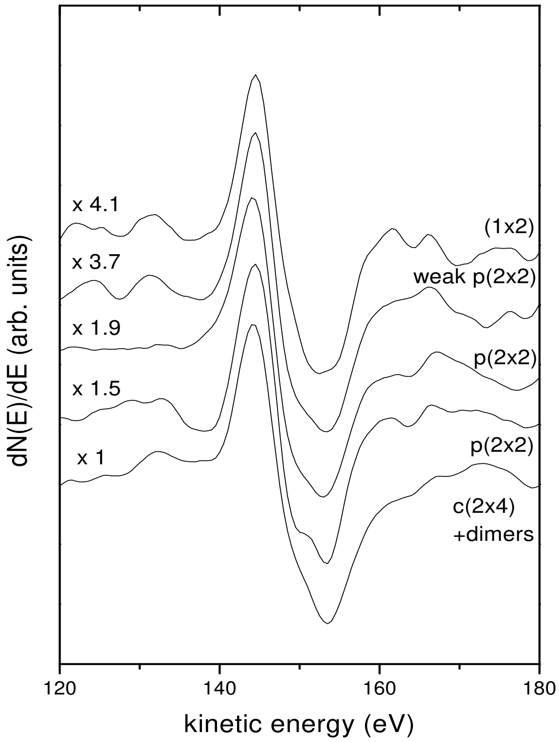

Figure 8.11: Differentiated AE spectra at different sulfur coverages. All spectra have been normalized to the same peak-to-peak height, the scaling factors are given on the left. On the right, the corresponding LEED pattern are indicated. For the p(2×2) structure two spectra (at slightly different coverage) are given to show the variation of spectral resolution.

sulfur signals in Fig.8.10 reveals a slight asymmetry of the peaks, i.e. they show a slight shoulder at high kinetic energy, which causes the 154 eV peak in the dN(E)/dE spectra.

To investigate a possible change in the peak shape at different coverages, several spectra corresponding to different structures and coverages have been acquired with half the step size (0.5 eV). After subtraction of a spectrum from the clean surface and normalization to the same sulfur coverage, the changes (or their absence) can be readily seen in the dN(E)/dE spectra (Fig. 8.11): The peak shapes, although not identical, are essentially the same. Only the spectrum with the lowest coverage seems to show only a more or less broad peak with no internal structure, whereas the other spectra show an asymmetric peak with a low-energy shoulder. This is most clearly resolved for one of the p(2×2) spectra at approx. 0.5 ML coverage. That it is less clear for the second p(2×2) spectrum (which corresponds to an only slightly different coverage) indicates that the differences arise mainly from the different signal to noise ratios of the original spectra, which can lead to a loss of resolution in the smoothed derivative spectra. This different signal to noise ratio comes from the

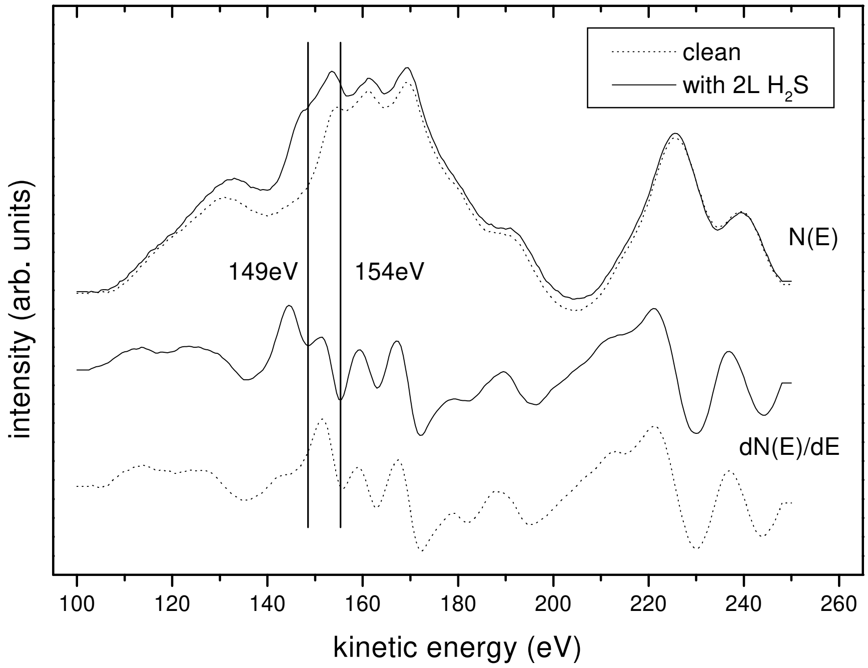

Figure 8.12: AE spectra at a low sulfur coverage and for the clean surface shown for comparison. The N(E) and dN(E)/dE spectra are given. The sulfur coverage in the corresponding spectra is 0.15±0.05 ML compared to the saturated surface at 0.75 ML.

instability of the electron gun, which shows increasing target currents even after a 'warm up' time of one hour, resulting in a different absolute intensity of the recorded spectra.

That the Auger lineshape is apparently not dependent on the sulfur coverage is on the one hand reasonable, on the other hand, however, surprising. It is reasonable in the low coverage regime up to 0.5 ML, since from the STM data [and also from the previous LEED I(V) analysis] there is no evidence for two different binding sites for the sulfur atoms. Near saturation, however, the dimers in the on-top position apparently exhibit a different bond than the first layer sulfur atoms. Judging from STM, a constant lineshape would be expected up to 0.5 ML, with a possible change occurring above this coverage due to the dimers.

Such a situation, a change in the lineshape at higher coverages, has been observed for sulfur on W(001) [141, 142], accompanied by additional peaks in the XP spectra and a change in the LEED pattern. In those studies a different binding site at high sulfur coverages was proposed, explaining the LEED pattern and the XPS data. In how far the change in Auger lineshape reflects the change in bonding geometry or is caused by a different deexcitation mechanism, could not be resolved. The latter has been proposed as the cause for various high-energy satellites for C, N, O, S, and Cl on Ni, Fe, and the (001) and (110) surfaces of Cu [143]. It was found that the position of the high-energy satellites depends on the nature of the substrate rather than on the adsorbate, while the intensity of the peaks depends on the adsorbed species. Also, for the case of copper, which was the only single crystal substrate used in that study, no dependence of the peak position nor intensity on the substrate orientation or overlayer structure was found.

The proposed mechanism for these high-energy satellites is a deexcitation of the initial core hole in the adsorbate atom via an electron coming from the substrate valence band and not from the higher levels of the adsorbate atom itself. The main contribution is proposed to arise from a deexcitation via the metal d-band, and the following relation is given:

$$\frac{1}{2}[E(j) - E_{X_1}] = E_d \tag{8.1}$$

where E_{X_1} is the position of the high-energy satellite, $E(j)$ is the energy of the corresponding principal transition (as measured by XPS), and E_d is the binding energy of the metal d-band. In the case of sulfur on iridium, E_{X_1} = 154 eV, $E(j)$ = 164 eV (S 2p emission) [144] and the binding energy of the Ir 5d electrons is 4.0 eV [144], which is in reasonable agreement with equation 8.1, regarding a possible chemical shift for the (S 2p) signal upon adsorption on iridium and the uncertainty in the energy calibration of the AE signal. One can conclude that the proposed mechanism indeed could be responsible for the S(154 eV) signal in our case. Of course, a final answer can only be supplied by inverse Auger emission experiments, which would reveal the present deexcitation channels. A different binding site at least is not indicated here, since neither the LEED calculations nor the STM show any evidence for two different sites in the p(2×2) case. Since the 154 eV signal is observed over the whole coverage range, changes in bonding geometry can be ruled out as origin.

As shown above, the lineshape does not change (significantly) for different coverages, and thus the peak-to-peak height of the sulfur signal can be used as a measure for relative sulfur coverages. At saturation, the ratio of the peak-to-peak amplitudes in the dN(E)/dE spectra is 2.8±0.1 for the S(154 eV)/Ir(230 eV) signals, and for the p(2×2) structure a ratio of approx. 1.6±0.1 is found (for evaluation of the sulfur peak-to-peak amplitude the pure sulfur spectrum is used, i.e., a spectrum from clean Ir(110) has been subtracted after appropriate normalization).

Inserting these values in equation 5.2 (using the sensitivity factors from [73]) one obtains a sulfur concentration of only 10 at. % for the c(2×4) structure. This clearly demonstrates that this equation is not applicable for heterogeneous samples. Equation 5.10, where the adsorbate is assumed to stay on top of the substrate, should be used instead. But again, there are several difficulties in doing so:

First, the IMFP for electrons in sulfur obtained by the 'universal' equation 5.9 is questionable, since this equation is simply a fit to measured IMFPs, and the experimental data are known to scatter by 30% around this fit. A second uncertainty are the backscattering terms derived from equation 5.5, since the equation again relies on a fit to experimental data corresponding to different elements than sulfur and iridium. A third parameter that is uncertain is the thickness of the adsorbate layer. Since the substrate is reconstructed, only the difference in z-coordinates along the surface normal can be used as a meaningful thickness in the framework of equation 5.10. The detailed structure of the substrate and the overlayer is thus discarded, and they are seen simply as a flat, homogeneous layers separated by a certain thickness. For the p(2×2) structure a thickness of 0.936 Å may be taken, which is the height of the sulfur atoms above the iridium atoms of the first layer (in the [110] direction) according to LEED [7]. Doing so, and using 1.63 and 2.14 for the backscattering factors for 154 eV electrons in sulfur and iridium, respectively, one obtains $\theta_{p(2x2)}$=0.48 ML and $\theta_{c(2x4)}$=0.79 ML for the p(2×2) and c(2×4) structure, respectively. Regarding the uncertainties in the parameters, the result compares surprisingly well with the expected values of 0.5 ML and 0.75 ML for the 'ideal' structures. It must be noted, however, that the same layer thickness has been used for both structures, which is incorrect because of the bilayer nature of the c(2×4) overlayer. The signal from a bilayer structure is different from a monolayer signal corresponding to the same sulfur amount, since attenuation effects have to be taken into account. However, the difference between the S(154 eV)/Ir(230 eV) peak-to-peak *ratios* of a monolayer and a bilayer structure may be small. For the bilayer structure not only the overlayer signal is attenuated due to sulfur atoms in a second layer above first layer sulfur atoms, but also the substrate signal under the bilayer patches is attenuated more strongly than under the monolayer patches. But at the same time the signal from the uncovered substrate is higher in the bilayer case. Since these effects partly counteract, it is not clear *a priori* whether the peak ratio for the bilayer structure is higher or lower than for the monolayer case. But as will be shown in the following, the resulting differences may indeed be small:

If we assume a monolayer structure with a thickness of a_1 and a coverage of θ, then the Auger intensities in normal emission would be

$$I_A^1 = S_A \frac{R_B(E_A)}{R_A(E_A)} \theta \{1 - \exp[-a_1/\lambda_A(E_A)]\} \tag{8.2}$$

$$I_B^1 = S_B\{(1-\theta) + \theta \exp[-a_1/\lambda_A(E_B)]\} \tag{8.3}$$

for the adsorbate and substrate layer, respectively. Here, again $\lambda_A(E_{A,B})$ is the IMFP for electrons of energy E_A, E_B in the adsorbate material, and S_A, S_B are the intensities of the pure adsorbate and substrate materials, respectively (i.e. the sensitivity factors). The terms $R_A(E_A)$ and $R_B(E_A)$ are the backscattering factors for electrons of energy E_A in the adsorbate and substrate material, respectively.

For a bilayer structure composed of patches of thickness a_1 and $a_1 + a_2$ each covering an area corresponding to $\frac{1}{3} \times \theta$ as depicted in Fig. 8.13, the contributions would be

$$I_A^2 = S_A \left\{ \frac{2}{3}\frac{I_A^1}{S_A} + \frac{1}{3}\frac{I_A^1}{S_A} \exp(-a_2/\lambda_A(E_A))] \right\} \tag{8.4}$$

$$I_B^2 = S_B \left\{ 1 - \frac{2}{3}\theta + \frac{1}{3}\theta[\exp(-a_1/\lambda_A(E_B)) + \exp(-(a_1+a_2)/\lambda_A(E_B))] \right\}. \tag{8.5}$$

In equation 8.4, the adsorbate signal of 2/3 of the total coverage is not attenuated and corresponds to the respective fraction of the monolayer signal I_A. But the signal from

1/3 of the adsorbate atoms is attenuated by the presence of the second adsorbate layer of thickness a_2, so a corresponding exponential damping term is included. The bilayer adsorbate signal I_A^2 is hence smaller than the monolayer signal I_A^1. But depending on the thickness of the second adsorbate layer, the substrate signal I_B^2 may also be smaller compared to I_B^1. For a total coverage of $\theta = 0.75$ ML, the ratio of the adsorbate/substrate signals for the two models is

$$\frac{I_A^1/S_A}{I_B^1/S_B} \Big/ \frac{I_A^2/S_A}{I_B^1/S_B} = \frac{I_A^1/I_B^1}{I_A^2/I_B^2} = 1.05 \tag{8.6}$$

if we use $\lambda_A(E_A)$=8.4 Å, $\lambda_A(E_B)$=10.2 Å derived from equation 5.9 for energies E_A=154 eV, E_B=230 eV in sulfur, and for the thicknesses a_1=0.936 Å (LEED, see above) and a_2=2.05 Å (S-S distance in solid sulfur [145]). The latter can be regarded as a reasonable estimate for the second layer thickness, since from LEED measurements it is known that adsorbate-substrate bond lengths are usually within about 0.1 Å of the sum of the covalent radii [146]. For these parameters the coverage obtained by equation 5.10, or equivalently equations 8.2 and 8.3, is slightly underestimated, and the actual coverage would be 1.05 times larger, i.e. 0.83 ML (as a first order approximation it is assumed that the peak ratio I_A/I_B is proportional to the coverage). Hence the corrected coverage for the bilayer structure deviates even more from the expected 0.75 ML than the uncorrected value. But regarding the uncertainties in the parameters the deviation still is acceptable, and there is no need to question the model of the c(2×4) structure.

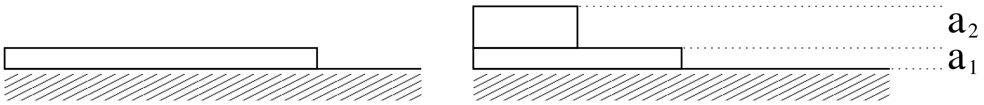

Figure 8.13: Models for the coverage correction in a bilayer structure. A total coverage of 0.75 ML (boxes) is dispersed on the substrate (hatched) as a monolayer (left) or a bilayer structure (right) according to the c(2×4) model. The different heights of the monolayer and bilayer patches are indicated (note that the area of the overlayer boxes does not scale with the amount of sulfur that they represent).

In conclusion, equation 5.10 is suitable for the coverage determination if the 'correct' thickness of the adsorbate layer is inserted. But regarding the uncertainties in the parameters involved, a direct calibration via a known structure (measured with the same experimental setup) is to be preferred. The results obtained with equation 5.10 are highly sensitive to the layer thickness, and using bond lengths as an approximation yield a far too low coverage for the case of sulfur on Ir(110). If the difference in z-coordinates (along the surface normal) of the sulfur atoms and the iridium atoms in the first layer are taken as the layer thickness, a good agreement with the model is obtained. This problem should not occur if unreconstructed surfaces are under consideration, and the surface and the adsorbate atoms lie in two well-defined parallel planes where the layer thickness is obvious.

For the c(2×4) structure the situation is even more complicated, since according to the model a third of the sulfur atoms lie in a second layer above sulfur atoms of the first layer. Since equation 5.10 is only applicable to overlayer structures of a homogeneous layer thickness, the coverage obtained by this equation has to be corrected. The correction again implies knowledge of the first and second layer thickness and the correct IMFPs, and hence may be wrong if incorrect values are used. In the stated example the results are in reasonable agreement with the expected values of 0.5 ML and 0.75 ML for the p(2×2) and the c(2×4) structure, respectively. For the latter, the calculated coverage is 0.08 ML higher than the theoretical saturation coverage, a deviation that can be regarded as acceptable considering the uncertainties of the parameters (especially the IMFPs and the sensitivity factors).

In principal, sensitivity factors can be discarded when using the Pd(111)-($\sqrt{7}\times\sqrt{7}$ $R30°$)-S structure for comparison, that was previously investigated in our own lab with the very same analyzer [147, 11]. However, this has not been considered here, since the corresponding structural model is still under debate. The Pd(111)-p(2×2)-S and the Pd(111)-($\sqrt{3}\times\sqrt{3}$) R30°-S structures, which are considered as simple overlayer structures, are not suitable either, since they could not be prepared with sufficient perfection (the structures never covered the whole sample surface).

8.3 Comparison with other Sulfur-Metal Systems

Several structural investigations of sulfur adsorption on metal surfaces exist (for reviews of adsorbate structures on metal surfaces see [131, 132, 97, 133, 47]), but most of them deal with (001) or (111) surfaces of fcc metals, and the (0001) surface of hcp metals. Studies on fcc(110) metal surfaces are quite limited, possibly because some of these surfaces exhibit reconstructions in the clean state and are hence deemed to be more complicated systems. A list of some of these studies is compiled in table 8.3. Quantitative studies are available only for the c(2×2) phases of Cu(110), Ni(110), and Rh(110), for the p(3×2) phase of Rh(110), the p(4×1) structure of Ni(110) (here a structural model was derived qualitatively by STM [148] and quantitatively by X-ray diffraction [149]) and for the p(2×2) phase of Ir(110). The models proposed for the many phases of sulfur on Pd(110) are only qualitative assumptions, as is the model for sulfur on Ag(110). We note that for the p(3×2) structure of Ni(110) no model has been proposed so far, but nevertheless it has been included in the list since by comparing the STM images of [148] with the LEED analysis of the Rh(110)-p(3×2)-S structure [150], the qualitative agreement is striking, and very likely the structure on Ni(110) is virtually the same as on the Rh surface [this may also apply to Pd(110) and Ag(110)]. The intermediate structures observed for the Ni(110)-S system, i.e. the p(5×2) and the c(8×2) structures, are also believed to be simple overlayer structures with no major substrate rearrangements [151, 148], but since no models were proposed so far they are not included in the list.

Comparing the known overlayer structures and substrate reconstructions, the present data suggest that for low and intermediate sulfur coverages on Ni, Cu and Rh only simple overlayer structures develop, without major substrate rearrangements. As shown, Ir(110) behaves different in that it adopts a (1×2) missing-row reconstruction upon postannealing the S-covered surface. Without annealing, however, no apparent substrate rearrangements

substrate	method	structure	substrate reconstruction	reference
Cu(110)	SEXAFS	c(2×2) + complex	no	[152]
Ni(110)	LEED	c(2×2)	no	[153]
Ni(110)	STM	p(3×2)	no	[148]
Ni(110)	STM	p(4×1)	yes	[148]
Pd(110)	LEED	p(2×3)	no	[154]
Pd(110)	LEED	c(2×2)	no	[154]
Pd(110)	LEED	c(8×2)	no	[154]
Pd(110)	LEED	p(3×2)	no	[154]
Ag(110)	LEED	p(3×2)	no	[155]
Rh(110)	LEED	c(2×2)	no	[156]
Rh(110)	LEED	p(3×2)	no	[150]
Ir(110)	LEED	p(2×2)	yes	[7]

Table 8.3: List of reported structures for sulfur adsorption on fcc(110) metals. Only reports that propose a structural model or assign binding sites are included (for multiple, uncontroversial reports on the same system, only the most recent is listed). Qualitative LEED works (pattern, but no proposed model) are not considered. SEXAFS = surface extended X-ray adsorption fine structure. By a complex structure is meant that no simple overlayer notation for the LEED pattern can be given, since beam multiplets are present or several beams are missing. For the substrate reconstruction, no distinction is made between clean surface reconstructions and adsorbate induced reconstructions (i.e., both are termed 'reconstructed').

are observed, as for the other systems. Substrate reconstructions upon annealing were also reported for the Ni(110)-p(3×2)-S surface, which then converts to a p(4×1)-S structure [151, 148, 149]. This phase seems to correspond to a sulfur saturated surface, since it did not convert to other phases upon heating in an H_2S atmosphere [151].

On Cu, Ni, and Rh sulfur adsorbs in fourfold coordinated hollow-sites with twofold symmetry, whereas on Ir it prefers the threefold coordinated fcc hollow site, which has threefold symmetry. Interestingly, sulfur does not induce a bulk-truncated structure as does oxygen, although the fourfold coordinated hollow sites as for the Cu, Ni, and Rh system would be accessible on the bulk truncated Ir surface. This indicates that the energy cost for inducing a bulk-truncated structure is too high to be overcompensated by a (possible) energy gain upon sulfur adsorption in a fourfold coordinated site. In this respect it is interesting to compare the electronegativities of O, S, and Ir. In Pauling units, the values are 3.44, 2.58, and 2.20, respectively [145]. Hence, S is only slightly more electronegative than Ir, whereas for O the value is much higher. In a qualitative way, one may argue that O shifts the charge density of the substrate more towards the adsorbate atoms than does S, and hence the charge density at the position of the substrate atoms is more bulklike in the case of O as adsorbate. Consequently, with chemisorbed O, there is no large driving force for relaxations or reconstructions, and the surface adopts a bulk truncated structure. Following this argumentational line, the charge density would be less affected by S, and the surface does not adopt a bulk truncated structure, but the (1×2) missing-row reconstruction.

It would be interesting to compare the Ir(110)-S system with sulfur structures on Pt(110), since the latter is known to exhibit a (1×2) missing-row reconstruction in the clean state [93], the same structure that Ir(110) adopts upon sulfur adsorption and subsequent heating. Indeed Berthier *et al.* observed several sulfur induced structures on Pt(110), but no conclusive structural models were proposed [157]. The observed patterns exhibited, in the sequence of increasing coverage, a c(2×6), p(2×3), p(4×3) and finally a c(2×4) structure. In some instances, after very long sulfur dosing and extended annealing, the latter converted into a poorly ordered p(4×4) pattern. It is remarkable that the c(2×4) structure also exhibited diffuse streaks at the same positions as observed for Ir(110). The coverage for that structure was determined to 0.75 ML, the same value as found for Ir(110) in the present work. The coverage determination by Berthier *et al.* can be regarded as correct, since they used radioactive tracer methods, i.e. radioactive sulfur was used for the adsorption experiments, and the mass of the adsorbed sulfur was determined *ex situ* by the emitted radiation.

Although in the experiments of Berthier *et al.* apparently a contaminated Pt(110) sample was used, judging from the (1×3) pattern of the surface prior to sulfur adsorption, the same sequence of LEED pattern was reported for sulfur adsorbed on the (1×2) reconstructed Pt(110) by Bonzel and Ku, except the p(4×4) structure [158]. The same characteristic streaking for the c(2×4) structure was observed, and the same saturation coverage was assigned to that structure, on the basis of CO titration experiments. Since at the time of those studies the structure of the clean Pt(110) surface was still unknown, it was nearly impossible to imagine a qualitatively correct structure corresponding to the several observed LEED patterns. Interestingly, none of the observed sub-saturation structures is a p(2×2), suggesting substantial differences between sulfur adsorption on Pt(110) and Ir(110), despite their similar (1×2) missing-row reconstruction for the clean (Pt) and sulfided surface (Ir). However, it is tempting to assume that the c(2×4) structure at saturation is very similar for Ir(110) and Pt(110). Hence, a proper quantitative reinvestigation of the Pt(110)-S system would be very interesting.

9 The Coadsorption of O and S on the (1×2)-Reconstructed Ir(110) Surface

The coadsorption of oxygen on a surface that is precovered with sulfur was investigated to study the effects of a typical catalytic poison, sulfur, on the adsorption of reactants in a catalytic oxidation process.

Two coverage regimes have been investigated, i.e. a low-coverage regime with less than 0.5 ML of sulfur and the saturated surface in the c(2×4)-6S structure. In the following, each regime will be treated in detail in a separate section.

9.1 The Coadsorption of Oxygen and Sulfur at Low Sulfur Coverages

For the low-coverage regime the clean iridium surface has been preexposed to approx. 2.5 L of H_2S at room temperature, followed by an anneal to 900 K. The LEED pattern is (1×2) with a higher background [Fig. 9.1(a)], as expected for sulfur coverages well below 0.5 ML. After cooling to room temperature again, O_2 is admitted to the chamber while monitoring the LEED pattern. After an exposure of approx. 1 L a sharp p(2×2) pattern develops, exhibiting the typical beam extinctions characteristic for the glide-plane symmetry [Fig. 9.1(b)]. STM images of this surface are shown in Fig. 9.2(a)–(c).

As can be seen in the overview image [Fig. 9.2(a)], darker patches exist on the surface which can be identified as a p(2×2) structure (without glide-plane symmetry, i.e. no zig-zag rows) on the small scale images [Fig. 9.2(c)]. Increasing the oxygen exposure further, the p(2×2) domains vanish and (1×2) rows can be seen that coexist with the sulfur domains. The LEED pattern corresponding to Fig. 9.2(d) also shows a (1×2) symmetry, with only very faint remnants of the (1/2,1/2) beams above the background [Fig. 9.1(c)].

Assuming that the darker p(2×2) patches correspond to oxygen domains, it is possible to determine the oxygen binding site from the registry between the oxygen and sulfur atoms. In Fig. 9.3 the underlying grid of the unreconstructed (1×1) structure is drawn, derived from the p(2×2)-2S domains. The corners of the grid indicate the positions where substrate atoms of the unreconstructed surface would be located. It follows that the protrusions of the p(2×2)-O domains correspond to short-bridge sites. If one assumes that oxygen is imaged as a protrusion as was found for the c(2×2)-O structure (section 7.4), the oxygen

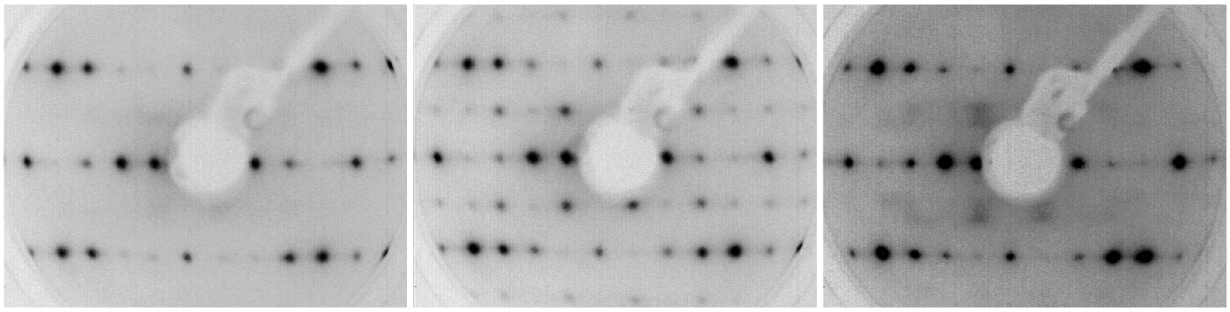

(a) (b) (c)

Figure 9.1: LEED pattern during coadsorbtion of oxygen on the sulfur-precovered surface, electron energy 146 eV. (a) Before oxygen adsorption. A (1×2) pattern with slightly higher background is seen. (b) After an exposure to approx. 1 L O_2 a p(2×2) pattern with systematic extinctions appears. (c) After further exposure to approx. 10 L O_2 the pattern converts back to a (1×2) symmetry. The contrast in the images has been adjusted to show diffuse features in the background.

binding site can be assigned to this site (note that even if the depressions would be assigned to the oxygen atoms, the corresponding binding site would be the same). This is consistent with the oxygen site found for the c(2×2)-O structure, which is also a short-bridge site according to LEED [123]. Apparently only the local adsorption geometry is important, and not the substrate reconstruction. Adsorbate-adsorbate interactions may be responsible for the ×2 periodicity along the rows, whereas interaction perpendicular to the rows (along [001]) seems to be weaker. This is indicated by occasionally occurring shifts between the oxygen [$\bar{1}$10] rows, leading to a (locally) centered geometry (see the five marked atoms on the left of Fig. 9.3). The weak interaction is reasonable since the oxygen atoms are far apart in the [001] direction due to the substrate reconstruction, compared to the dense c(2×2) structure on the unreconstructed surface. It is also worth noting that oxygen stays above twofold coordinated sites, although threefold coordinated sites are available (e.g., the sulfur adsorption sites) on the reconstructed substrate. On Ir(111), on the contrary, oxygen adsorbs over the threefold fcc hollow site [90]. Hence oxygen in this respect behaves different than sulfur, which adsorbs over fcc sites on both Ir(111) and Ir(110) [135, 7].

Upon further oxygen exposure, a compression of the oxygen domains into a (1×2) structure is observed [Fig. 9.2(d)]. Due to the missing long-range ordering of the oxygen and sulfur domains, an accurate recalibration of the image to eliminate thermal drift effects is not possible for this image. Therefore, a binding-site assignment cannot be made without ambiguity. It is clear that the oxygen site can be either a short-bridge or on-top site or a mixture of both (if only high-symmetry sites are considered). That the (1×2) rows seen in the image indeed are covered by oxygen atoms and are not the pure substrate rows, can be concluded from the following observations: Besides the bright protrusions along the rows sometimes darker patches are imaged which may be attributed to the substrate. Furthermore defects along the rows are mobile as is seen on subsequent images (Fig. 9.4), which would not be expected for substrate atoms at room temperature. The defects therefore represent missing oxygen atoms rather than missing iridium atoms.

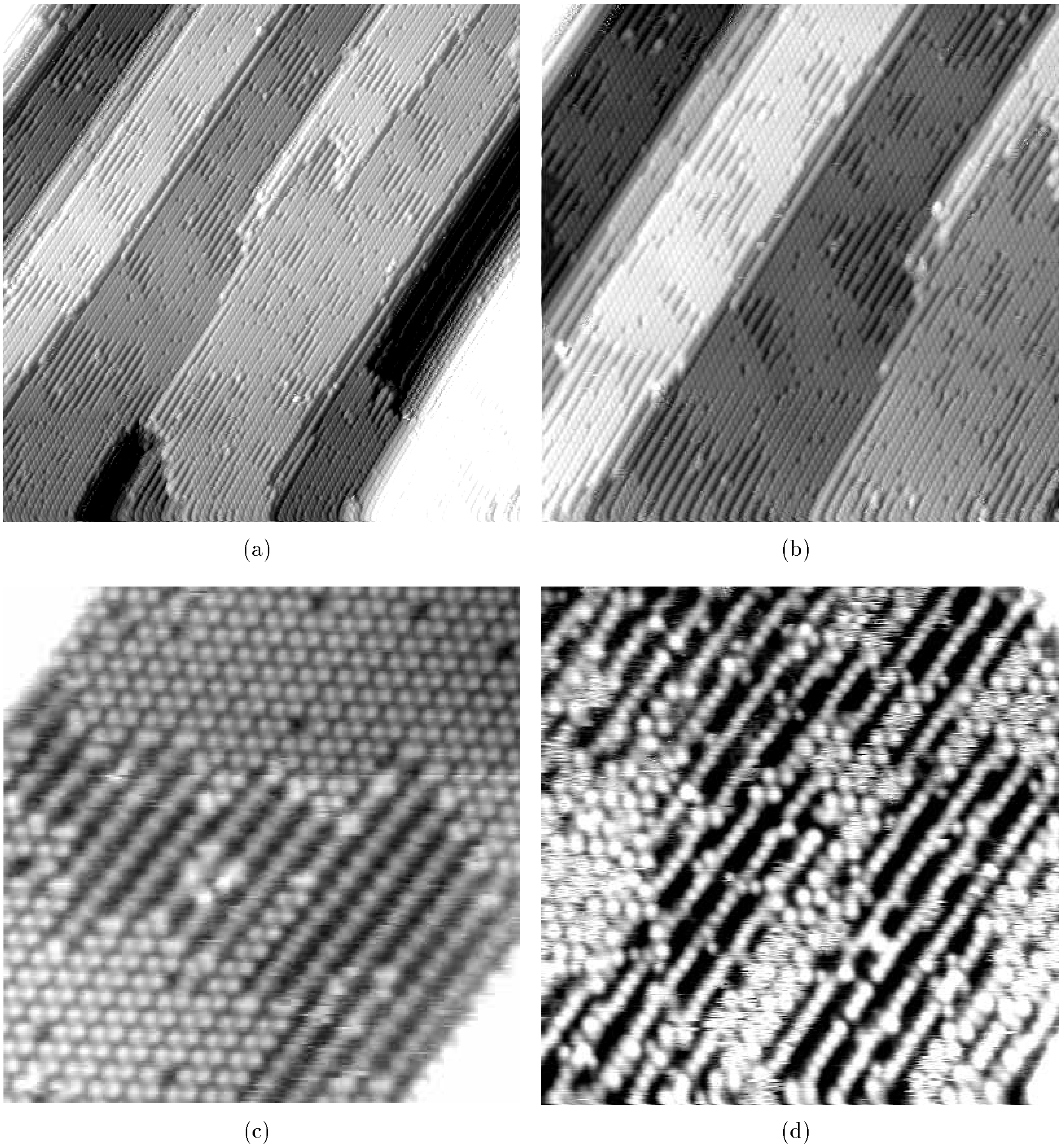

Figure 9.2: Coadsorption of oxygen on the sulfur-precovered surface. (a)–(c) After an exposure to approx. 1 L of O_2. The sulfur atoms have coalesced to form p(2×2)-2S domains, separated by p(2×2) domains formed by oxygen atoms. U_t=900 mV (a,b)/ -50 mV (c), I_t=1 nA, image sizes (550 Å)^2,(360 Å)^2, and (125 Å)^2 for panels (a), (b), and (c), respectively. (d) After further exposure to approx. 10 L O_2. No larger domains of p(2×2) or c(2×4) symmetry are found. The oxygen atoms are arranged in a (1×2) configuration on top of the substrate rows, U_t=-50 mV, I_t=2 nA, (120 Å)^2.

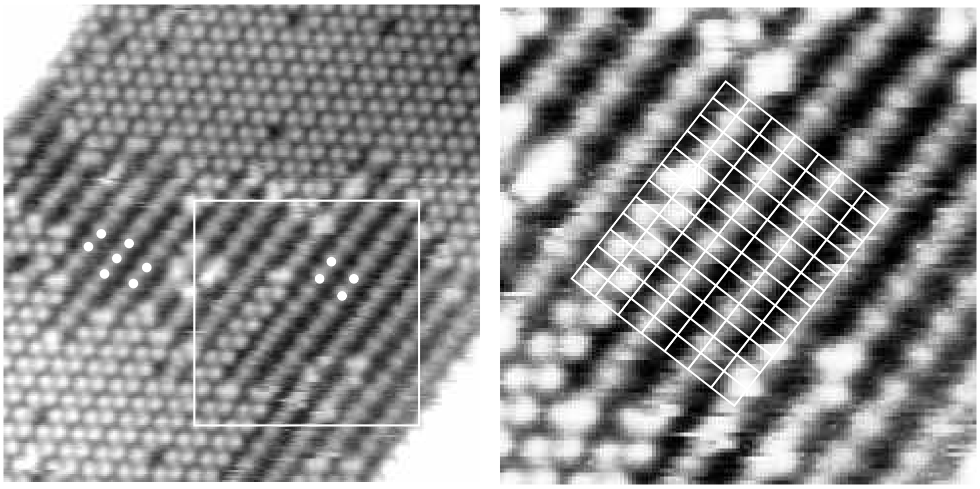

Figure 9.3: Identification of the oxygen binding site. A magnification of the marked area (left panel) is shown on the right. A (1×1) grid is superimposed, derived from the registry of the sulfur domains. The corners of the grid indicate the positions of substrate atoms for the unreconstructed surface. The oxygen atoms (protrusions) reside over short-bridge sites. Note that the oxygen atoms are occasionally shifted along [$\bar{1}$10] (along the rows), leading to a centered arrangement (left marks in the left panel), whereas the square shaped arrangement indicates the usual (2×2)-O unit cell (right marks in the left panel). The shift indicates a weak O–O interaction across the rows (in [001]).

Besides the oxygen atoms on the rows and the sulfur atoms at fcc sites there are several other features in the images of Figs. 9.2(d) and 9.4: Occasionally protrusions between the rows are imaged [see mark 'A' in Fig. 9.4(a)], and numerous small protrusions at the sides of the rows are seen [mark 'B' in Fig. 9.4(a)]. It is not clear whether these protrusions are sulfur atoms in a different chemical state or oxygen atoms. Also the nature of the protrusions between the rows is unknown.

Looking at images like Fig. 9.2(d), the local sulfur coverage seems to decrease. However, no change in the sulfur AES signal could be detected before and after oxygen adsorption, not even after an oxygen exposure of 100 L, indicating that the total sulfur coverage stays constant and no sulfur is removed from the surface. The apparent low sulfur coverage in some STM images is thus only a local effect and is not representative for the surface on average. To check if a reaction between the adsorbed oxygen and sulfur atoms occurs at elevated temperatures, the sample is postannealed at approx. 600 K in vacuum for several minutes. After the annealing, no oxygen can be detected anymore and the sulfur signal is reduced significantly. After cooling to room-temperature, 'noisy' STM images are obtained typical for low sulfur-coverages [compare Fig. 8.4(a)] and the LEED pattern remains (1×2). So it can be concluded that indeed a reaction occurs, but only after moderate annealing. In the reaction, sulfur is removed from the surface, possibly in the form of some oxide, i.e., some SO_x compound. Exactly which products are formed in the reaction cannot be revealed by the experiments done so far. Thermal desorption spectroscopy would be a way to elucidate the reaction mechanism, but these experiments cannot be performed with the

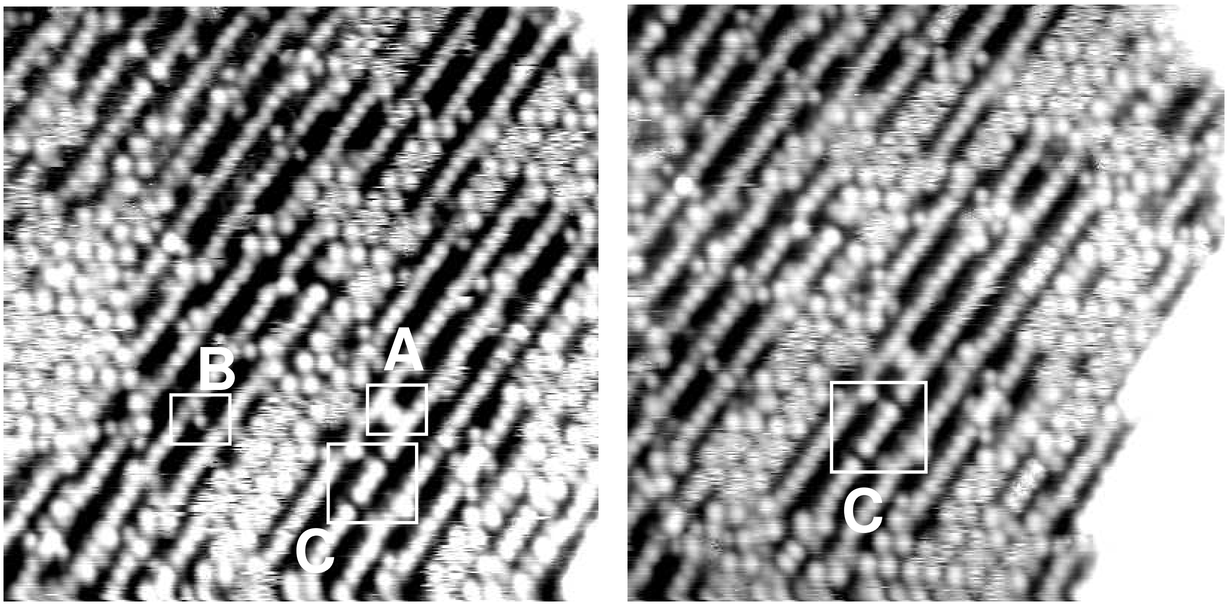

(a) (b)

Figure 9.4: The high-coverage (1×2)-O phase in the O/S coadsorption. In (a) several features are marked (see text). Atoms can move along [$\bar{1}$10] as indicated by mark 'C' in (a) and (b), suggesting that the protrusions along the rows represent oxygen atoms rather than substrate atoms. (120 Å)^2, U_t=-50 mV, I_t=2 nA.

present setup (the distance between the sample and the QUAD in our system is too large to detect the reaction products, and furthermore the achievable heating rate is too low).

Since oxygen is present in two different configurations, it is interesting to investigate the reaction between oxygen and sulfur for these two different structures. In other words: Does the reaction occur for both structures, or only for the high-coverage (1×2) phase? In order to answer that question, the S-precovered surface is exposed to only approx. 1 L of O_2, so that the sulfur domains coalesce as in Fig. 9.2(a)–(c), and the sulfur and oxygen p(2×2) domains are separated. The surface is then postannealed in vacuum at 600 K for 15 minutes before acquiring an AE spectrum. Then the surface is exposed to a further 1 L O_2, and postannealed again. The procedure is repeated ten times, so that a total oxygen exposure of about 10 L is achieved. By repeating the exposure/annealing cycle several times it should be assured that a reaction, if present, can be detected. Since the oxygen and sulfur domains are separated, the possible reaction can only occur at the domains boundaries, provided that the phase separation also prevails at the annealing temperature. Due to the limited number of reaction sites (the boundary sites) the loss of sulfur observed in one adsorption/annealing cycle may be quite small. Repeating the procedure several times should accumulate the losses and lead to a significant decrease in the sulfur signal after the last cycle. However, as is seen in Fig. 9.5, this seems not to be the case. Regarding the noise level of the spectra and the corresponding fluctuation of the peak heights, the sulfur signal after the tenth cycle is still approximately the same as directly after the initial sulfur adsorption. But, if the surface is exposed to 10 L O_2 *in one cycle* to obtain the (1×2) oxygen phase as in Fig. 9.2(d), the sulfur is completely removed from the surface after annealing.

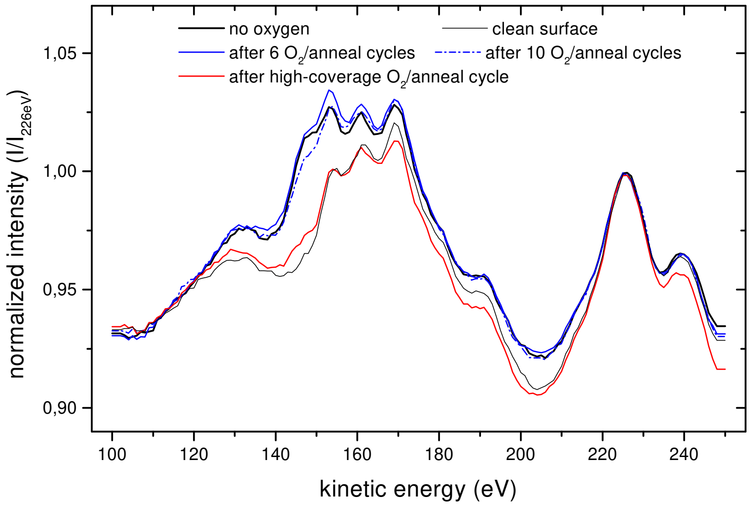

Figure 9.5: AE spectra of the clean and sulfur-preexposed surface at different stages of sulfur oxidation. All curves are normalized to the Ir peak at 226 eV. The blue curves have been acquired after an O_2 exposure of approx. 1 L and postannealing the surface at 600 K in vacuum. Ten of these adsorption/anneal cycles have been performed, but no significant decrease in the sulfur signal is observed. The red curve was acquired after exposing the surface to 10 L O_2 and postannealing at 600 K. The sulfur signal has decreased significantly, the spectrum being essentially the same as the one for the clean surface.

Thus, judging from the AES measurements, the reaction occurs (at a significant rate) only for the high-coverage phase of oxygen, where the oxygen and sulfur domains are not clearly separated anymore. It is tempting to assume that the (1×2) oxygen phase is a necessary precursor state for the reaction. However, before drawing such conclusions, further experiments are necessary to corroborate the AES results. The insignificant decrease in the sulfur signal for the low-coverage structure may still be due to insufficient accumulation, because if the reaction occurs only at the boundaries of the oxygen and sulfur domains, the reaction rate is of course proportional to the length of these boundaries, as it was found for the CO oxidation on Pt(111) [159]. If the two reactants mix almost completely as in the (1×2)-O phase, the reaction is not limited to domain boundaries and may proceed at a much higher rate, leading to a significant decrease of the sulfur signal in AES, as observed. Although the total amount of adsorbed oxygen was similar for both phases, this may not be the limiting factor, but rather the number of possible reaction sites. To observe the reaction directly by STM at 600 K could reveal the mechanism, at least in principle. But such experiments are extremely difficult and it is questionable if they are feasible at all. So far only only very few reactions have been studied by STM [160], and those were mostly limited to room-temperature or below, where the diffusion of the reactants is sufficiently slow to be studied with atomic resolution.

One further conclusion can be drawn regarding the phase separation between the p(2×2)-2S and the low-coverage p(2×2)-O structure: Since no significant loss of sulfur can be detected even after several adsorption/annealing cycles, it can be concluded that the phases are still separated at 600 K. If they were not, the reaction would not be limited to domain boundaries, and there would be no reason why the reaction should not proceed. The total amount of oxygen adsorbed on the surface would then be the limiting factor, which is not the case as shown above.

In summary, a reaction occurs between coadsorbed oxygen and sulfur at elevated temperatures, resulting in a decrease in the sulfur coverage. At room temperature the reaction does not occur at a significant rate, according to the unchanged sulfur signal in the AE spectra before and after oxygen adsorption. The reaction mechanism cannot be revealed by the STM results so far, but the formation of a (1×2) high-coverage oxygen phase may play a crucial role. A precursor of this structure is the low-coverage p(2×2)-O phase, in which oxygen is located over short-bridge sites on the [$\bar{1}$10] rows. The interaction between oxygen and sulfur is repulsive, leading to a segregation of the competing adsorbates into separated domains of either S or O at low oxygen coverages [Fig. 9.2(a)–(c)]. This phase separation is present at least up to temperatures of 600 K, judging from AES measurements. In a simple picture of locally pairwise interaction the sum of the O–O and S–S interaction energies is lower than twice the O–S interaction energy:

$$E_{\mathrm{O-O}} + E_{\mathrm{S-S}} < 2E_{\mathrm{O-S}} \quad \text{for} \quad \Theta_{\mathrm{O,local}} \leq 0.25. \tag{9.1}$$

At high local coverages ($\Theta_{\mathrm{O,local}} > 0.25$), when oxygen is compressed into a (1×2) structure, an intermediate situation between competitive and cooperative adsorption is present, since the sulfur domains decrease in size and both adsorbates tend to mix [Fig. 9.2(d)]. It can be concluded that the additional energy needed to compress the oxygen from a '×2' periodicity along [$\bar{1}$10] to a '×1' periodicity shifts the energy balance in the above equation more to the right. The $E_{\mathrm{O-O}}$ repulsion becomes larger and the resulting relation would be

$$E_{\mathrm{O-O}} + E_{\mathrm{S-S}} \approx 2E_{\mathrm{O-S}} \quad \text{for} \quad \Theta_{\mathrm{O,local}} > 0.25. \tag{9.2}$$

A phase separation is no longer energetically favorable, but neither is a pure cooperative adsorption with a complete mixing of the adsorbates. As mentioned, the (1×2)-O phase may be a necessary precursor state for the sulfur oxidation. A significant reduction of the surface sulfur concentration is only observed when heating the (1×2)-O structure to approx. 600 K. Heating the low-coverage p(2×2)-O phase does not lead to a significant sulfur oxidation, not even after several progressive adsorption/anneal cycles. One reason for this observation may be the higher energy of the (1×2)-O phase, compared to the p(2×2)-O phase. The repulsive O–O interaction is stronger for the former, hence it may be regarded as a kind of 'activated' structure, which reacts readily upon moderate annealing. This conclusion, however, should be regarded as tentative, since it remains to be shown if the reaction for the p(2×2)-O phase occurs only at the sulfur/oxygen domain boundaries (and thus may have been undetectable by the experiments so far) or if it does not occur at all. Thermal desorption spectroscopy could be a way to answer this question.

9.2 The Coadsorption of Oxygen and Sulfur at High Sulfur Coverages

Exposing the saturated c(2×4)-6S structure to 1500 L O_2 (total pressure 2×10^{-7} mbar) at room temperature has no influence on the LEED pattern. The surface seemed completely passivated by the sulfur overlayer. Even under ambient conditions the passivation is good: The sulfur saturated surface still exhibits a good c(2×4) LEED pattern with only slightly higher background after exposing it to air for several hours, with no further preparation. STM images of the surface after oxygen exposure exhibit the c(2×4)-6S structure with some defects only [Fig. 9.8)(a),(b)]. Again, as for low sulfur coverages, the situation changes when the surface is annealed to higher temperatures. Because the surface seemed quite insensitive to the oxygen atmosphere at room-temperature, the sample is now annealed to 470 K *during* the oxygen exposure, to ensure a saturation of the surface with oxygen. Hence, a distinction in terms of oxygen coverage is not intended here. At 470 K it was possible to monitor possible structural changes by LEED with no difficulties due to background light coming from the heating filament or the hot sample. A series of LEED pattern (Fig. 9.6) recorded during the coadsorption shows the gradual change from a clear c(2×4)-6S pattern to a p(2×2)-2S and finally a mixed (1×2) and c(2×2)-O pattern. AE spectra recorded at the different stages of the coadsorption indicated a gradual desorption of the sulfur until the surface is mostly covered by oxygen, with only a small shoulder at 149 eV indicating residual sulfur (Fig. 9.7).

STM images taken at the corresponding intermediate steps (after cooling to room temperature in vacuum, i.e. with no oxygen atmosphere) reveal the structural changes on a nanoscopic scale: The dimer atoms in the second layer apparently are 'pushed together' to form adatom islands of p(2×2) structure [Fig. 9.8(c)–(f)]. The area of the adatom islands should cover half the STM images if the dimer atoms were just compressed into the p(2×2) islands, with no sulfur desorption. Obviously the area covered by the islands is much smaller [it corresponds to approx. 5% of the area in Fig. 9.8(e)], consistent with the decreasing sulfur signal in the AE spectra. Interestingly, the parts of the surface where the dimer atoms are removed, immediately convert back to the p(2×2) structure, as seen in Fig. 9.8(d). Only very small c(2×4) domains with no dimers are found, and at the stage where the LEED pattern is a sharp p(2×2) pattern, no sulfur dimers are left, and the whole surface has adopted the p(2×2) configuration, including the adatom islands. It is quite surprising that the adatom islands also form the p(2×2) arrangement, since this usually requires a (1×2) missing-row substrate. If one assumes that the area underneath the adatom islands also exhibits a p(2×2)-2S structure, as does the rest of the surface, it is not clear how the island structure is formed. The adsorption site must definitely be different from the one of the 'normal' p(2×2) structure, where the S atoms adsorb over fcc sites of the missing-row (111) facets.

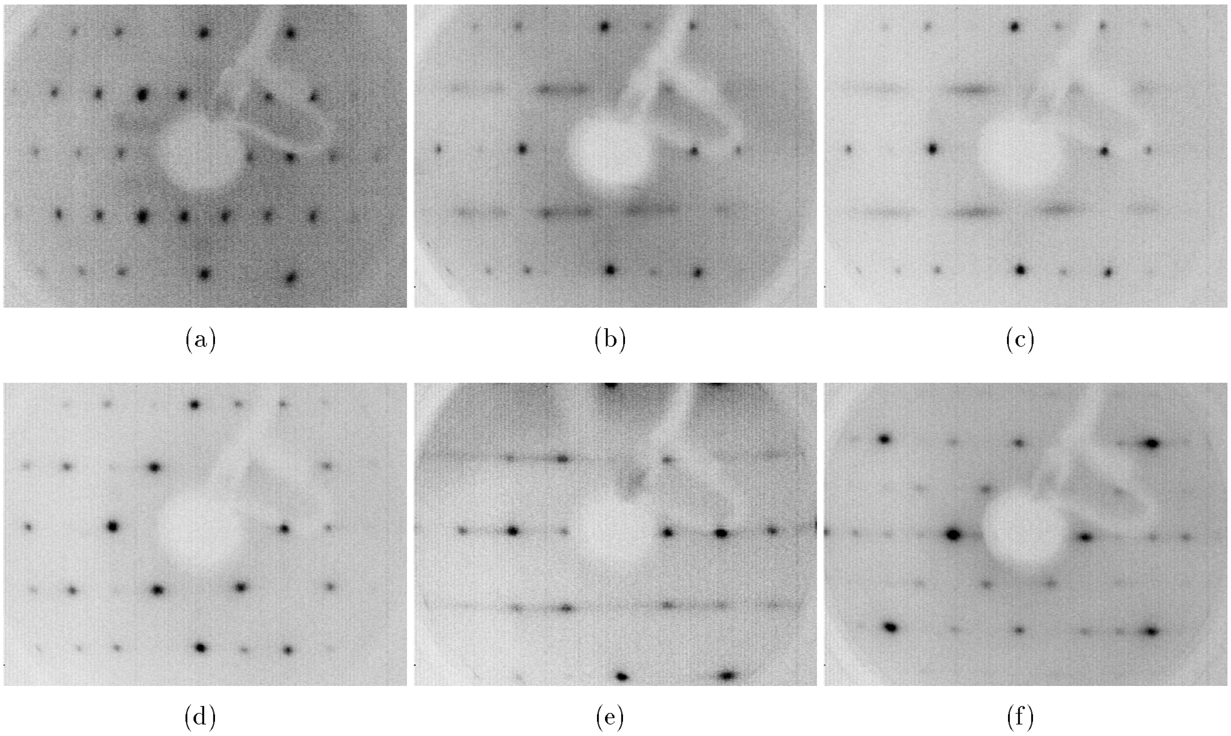

Figure 9.6: LEED pattern of the Ir(110)-c(2×4)-6S structure during oxygen exposure ($p \approx 10^{-8}$ mbar) at 470 K. (a) Unchanged c(2×4) pattern at the beginning of the exposure (also seen after exposure to 1500 L O_2 at room-temperature). Electron energy is 146 eV. (b) The centered spots become streaky after 45 min (146 eV). (c) The centered spots have completely turned to streaks (60 min, 146 eV). (d) A well ordered p(2×2) pattern develops (90 min, 146 eV). (e) The half-order spots become streaky (100 min, 61 eV). (f) Finally a mixed (1×2) and c(2×2) oxygen overlayer is seen (110 min, 150 eV).

Another possible substrate configuration below the adatom islands is a (1×2) missing-row reconstructed iridium island. This would also explain the height of the adatom islands of approximately 1.4 Å, which corresponds to a monoatomic step. A sulfur island on a sulfur substrate would very likely appear more shallow, of the order of 0.4 Å, as it is found for the dimer atoms. The registry of the p(2×2) domains on the adatom islands and the terrace is also consistent with the '(1×2) island model' (Fig. 9.9). So there is some evidence that the adatom islands are indeed monoatomic (1×2) missing-row reconstructed iridium islands, on top of which sulfur adsorbs in a p(2×2)-2S structure.

But where does the iridium come from? This question cannot be answered on the basis of the present data. The islands are certainly not preexisting, since they have never been observed under similar preparation conditions for the Ir(110) c(2×4)-6S structure [compare also Fig. 9.8(a), where no such islands are seen]. Hence they must form during the coadsorption of oxygen at elevated temperatures. Most likely seems the diffusion of iridium atoms originating from steps, possibly under the influence of the adsorbed oxygen.

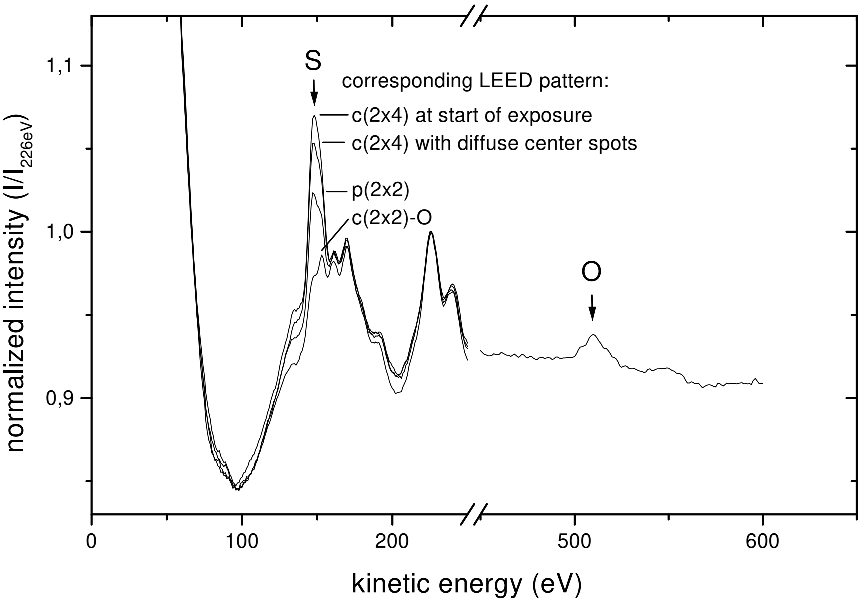

Figure 9.7: Integral N(E) AE spectra recorded at intermediate steps of the oxygen exposure, corresponding to the LEED pattern of Fig. 9.6. The sulfur signal gradually decreases. All spectra are normalized to the iridium peak at 226 eV. For the spectrum corresponding to the c(2×2)-O structure also the oxygen signal is shown (note the axis break). In the other spectra no oxygen can be detected. All non-labeled peaks correspond to Ir.

The diffusing iridium atoms could then be ‘trapped’ in vacancies of the sulfur overlayer, i.e., at positions where the sulfur has already desorbed and the underlying iridium substrate is exposed. Such vacancies can occasionally be seen in the STM images. The iridium atoms from the steps could then form islands on these exposed parts, which are then again decorated by diffusing sulfur atoms. However, at the present stage this remains speculation, and further experiments are necessary to reveal the true mechanism. High-temperature STM would certainly be a way to solve this problem.

The final stage of the sulfur desorption is shown in Fig. 9.8(g), where round shaped adatom and vacancy islands have formed, together with some ‘striped’ patches of residual (1×2) reconstructed iridium. The round shaped adatom and vacancy islands are unreconstructed parts of the surface with a c(2×2) oxygen overlayer. The shape of these unreconstructed parts indicates that the surface diffusion is no longer preferentially one-dimensional, as it is for the faceted and the (1×2) reconstructed surface. Very similar island forms are usually observed on sputtered surfaces after incomplete annealing [161]. In the sputter experiments, the shape of the islands and the adatom and vacancy island distribution was found to depend on the amount of removed material during the sputtering process. If approximately half a monolayer was removed, the observed island structures were very similar to the structures shown in Fig. 9.8(g). In this sense, the oxygen induced deconstruction from the (1×2) missing-row reconstructed Ir(110) surface to the unreconstructed surface also corresponds to such a sputter/anneal experiment. In the (1×2) phase, *exactly* half a monolayer is missing compared to the unreconstructed surface, and the observed shape of the islands in Fig. 9.8(g) is a consequence of the (1×2)→(1×1) deconstruction.

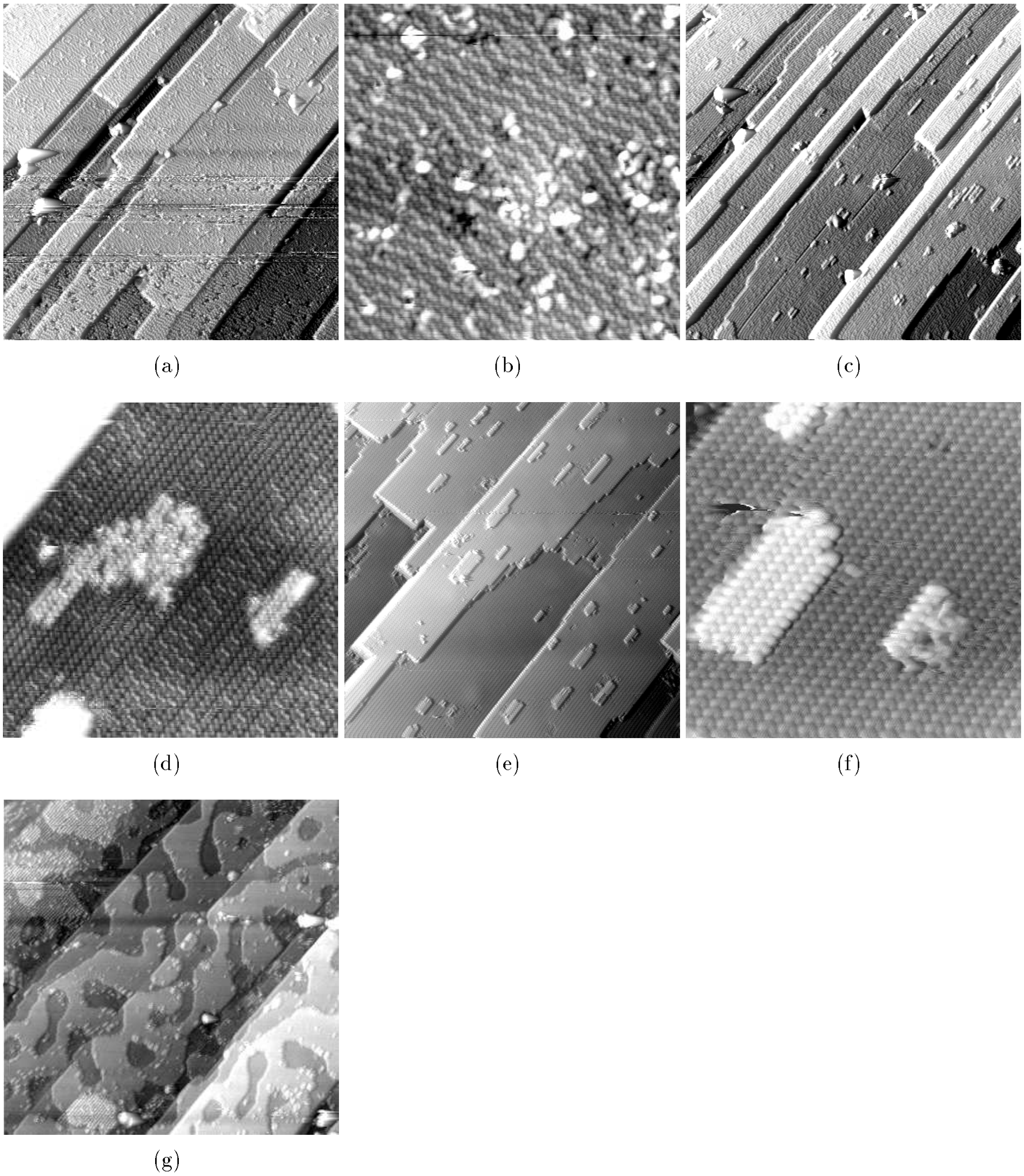

Figure 9.8: STM images corresponding to different stages of the oxygen exposure. All images are slightly differentiated to enhance contrast. (a)–(b) After exposure to 1500 L O_2 at room-temperature [compare Fig. 9.6(a)]. Some defects are seen, but the overlayer structure is essentially intact. (c)–(d) Adatom islands begin to form and p(2×2) domains with no sulfur dimers develop [compare Fig. 9.6(b)]. The height of the adatom islands is 1.4 Å, which corresponds to a monoatomic step. (e)–(f) All sulfur dimers are gone and the whole surface exhibits a p(2×2) structure, which is also found on the adatom islands [compare Fig. 9.6(d)]. The non-equivalence of the sulfur atoms in (f) is an artifact, as discussed in section 8.9. (g) The final stage after (nearly) complete desorption of sulfur. Round shaped adatom and vacancy islands of an unreconstructed (1×1) structure have formed, covered by a c(2×2)-O overlayer. The 'striped' patches (lower and upper left corner) correspond to residual (1×2) domains [compare Fig. 9.6(f)]. U_t=-0.9 V, I_t=1.0 nA for all images, sizes: (a) (1160 Å)^2, (b) (200 Å)^2, (c) (1160 Å)^2, (d) (235 Å)^2, (e) (770 Å)^2, (f) (150 Å)^2, (g) (960 Å)^2.

This also explains why such island formations have not been observed in the low-coverage regime (preceding section): In the low-coverage experiments, the sample was annealed in vacuum, not in an oxygen atmosphere, and the preadsorbed oxygen was reacted away before the (1×2)→(1×1) deconstruction could start, for which the presence of oxygen is necessary.

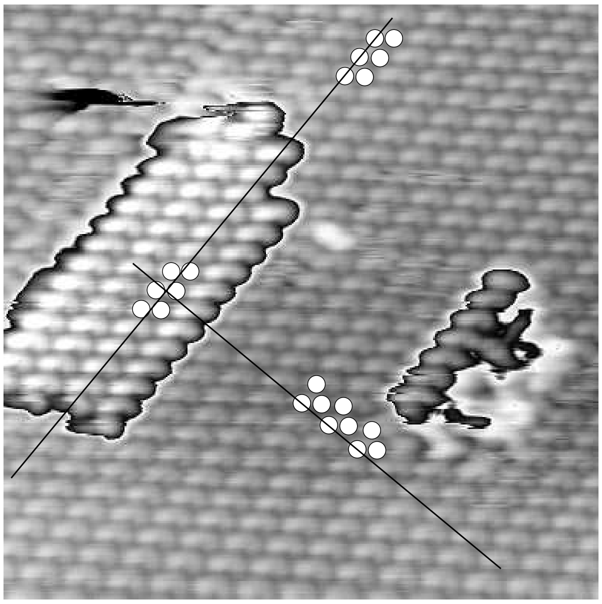

(a)

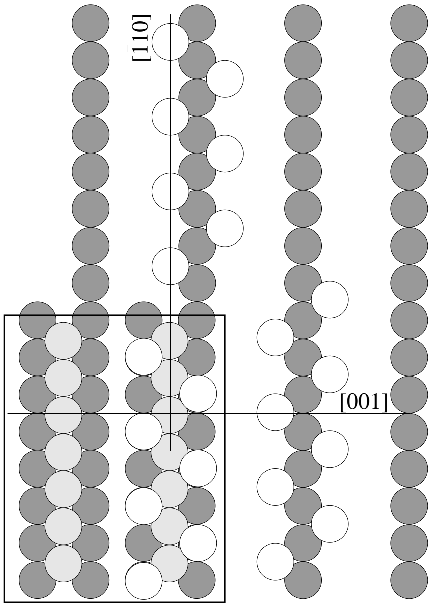

(b)

Figure 9.9: (a) STM image of an adatom island [compare Fig. 9.8(f)], (127 Å)^2, U_t=-0.9 V, I_t=1 nA. The greyscale has been adjusted for better visibility of the adatom and terrace structure. Due to an imperfect tip the atoms are not fully resolved (some atoms are indicated for clarity). The lines drawn along [$\bar{1}$10] and [001] direction across sulfur atoms of the p(2×2) structure visualize the registry of the island and terrace structures. For clarification, the structure is schematically depicted in (b). For the terrace, only the first layer iridium atoms are shown. The sulfur atoms are shown in white, the adatom island is in the box in the lower left corner. The island is a (1×2) reconstructed monoatomic iridium island, covered by the sulfur atoms in the p(2×2) structure. The registry of (a) agrees well with this model. Note that the step facet on the right side of the adatom island is of (111) type. Correspondingly, the left step facet has to be a (331) type, since no domain boundaries are present on the terrace or the island. But due to the limited resolution in this image, the registry near the left step facet is difficult to determine.

To summarize, also for the c(2×4)-6S structure a decrease in the sulfur concentration is found when heating the surface at 470 K in an oxygen atmosphere. Note that the temperature used here is lower than the one for the low-coverage regime, and therefore the sulfur desorption is slower in this case. Several structural changes in the sulfur overlayer occur during the process: The second layer dimer atoms of the c(2×4)-6S structure are 'compressed' into adatom islands of p(2×2)-2S structure, and the remaining sulfur overlayer also converts to a p(2×2)-2S structure. This again shows that a c(2×4) sulfur layer is not stable in itself on Ir(110)-(1×2), but needs sulfur dimers for stabilization.

When the sulfur concentration has decreased further, the iridium substrate converts to the unreconstructed (1×1) structure under the influence of the adsorbed oxygen. The oxygen forms a c(2×2) overlayer on these unreconstructed parts. The reaction is complete when all sulfur is desorbed and the surface has adopted an Ir(110)-c(2×2)-O structure. We note that the formation mechanism for the adatom islands is not known so far. The height and registry of these islands indicate that they are monoatomic iridium islands of (1×2) structure as are the terraces, and are also covered by sulfur atoms in a p(2×2)-2S overlayer.

A further open question is the reaction mechanism in the high-coverage regime. While for the low-coverage regime the reaction is of the Langmuir-Hinshelwood (LH) type, i.e., both reactants are chemisorbed on the surface, this mechanism is questionable in the high-coverage regime. In the early stages of the reaction, i.e., when the sulfur concentration is still 0.5 ML or higher, the surface seems to exhibit only a quite small number of defects. Oxygen islands or larger domains that are not covered by sulfur are not observed. Furthermore, there is no indication for oxygen in all but the final AE spectra (Fig. 9.7). Also after exposing the sulfur saturated surface to 200 L O_2 at room temperature, no oxygen signal can be detected in the AE spectra. So it is questionable if oxygen chemisorbs on the surface at this sulfur coverage (i.e. the surface seems to be completely poisoned with regard to oxygen adsorption), hence the reaction may rather proceed via the Eley-Rideal (ER) mechanism (where only one of the two reactants is chemisorbed) at high sulfur coverages. Measuring the dependence of the product formation rate on the oxygen partial pressure would reveal the mechanism [162]: If, for constant sulfur concentration at the beginning of the reaction, the product formation rate saturates for increasing oxygen partial pressures at a given reaction temperature, an ER mechanism is indicated. If the oxidation rate exhibits a maximum at a certain oxygen partial pressure and slows down at higher pressures, a LH mechanism is present.

9.3 Reaction between O and S on Other Metal Surfaces

The oxidation of sulfur has been observed previously on several metal surfaces like Cu(110) [163], Ni(110) [164], Ni(111) [165], Pt(111) [166], and Pt(110) [167]. In all cases where a identification of the reaction products was done, SO_2 was the only species observed, and the reaction was identified as the LH type on all surfaces.

It is worth noting that on Pt(111) the coadsorption of oxygen caused no compression of the sulfur islands into higher coverage structures [166]. Both oxygen and sulfur adsorb in p(2×2) phases at coverages up to 0.25 ML, whereas the saturation coverage of sulfur is 0.33 ML in the $(\sqrt{3}\times\sqrt{3})$ R30° structure. The latter phase was not observed during the coadsorption process, the LEED pattern exhibited a p(2×2) symmetry during the whole course of the reaction. This indicates that the interaction between oxygen and sulfur is not or only slightly repulsive, compared to the interaction of CO and S, which has been shown to cause a compression of sulfur into $(\sqrt{3}\times\sqrt{3})$ R30° islands on Pt(111) [137, 138].

The amount of SO_2 that was formed during the reaction on Pt(111) strongly depended on the distribution of sulfur over the surface. If the surface was prepared in a way that many small p(2×2)-S islands were formed, the SO_2 formation was much higher than with fewer, but larger sulfur domains [166]. This indicates that the reaction primarily proceeds at the domain boundaries, as is also assumed for the Ir(110) surface. The island distribution was strongly influenced by the adsorption sequence, i.e., whether sulfur or oxygen was first adsorbed. In the latter case a much higher SO_2 yield was observed, indicating the presence of many small sulfur domains. It must be noted that in those experiments sulfur was not adsorbed in the form of H_2S as in most of the other works, but was deposited as a beam of S_2 molecules produced by an electrochemical cell [166]. Only then the adsorption sequence has no major influence on the reaction, apart from differing distributions of the reactants.

If an oxygen precovered surface is exposed to H_2S gas as the sulfur source, a completely different reaction occurs. Due to the dissociation of H_2S a third reactant, hydrogen, is present at the surface, and a reduction of the oxygen atoms is observed which finally leads to water formation. Hence sulfur is not removed from the surface in this reaction, but rather deposited. This reaction was observed on several metal surfaces, e.g. on Pt(111) [168] and *in situ* by STM on Ni(110) [169].

For Pt(110), which may be comparable to (sulfurized) Ir(110) because of its (1×2) missing-row reconstruction (see remarks in section 8.3), Bonzel and Ku found that the rate of sulfur oxidation was only weakly temperature dependent, with a slower reaction at 670 K compared to 435–570 K, possibly due to a lower sticking coefficient for oxygen at higher temperatures [158, 167]. They also reported that the reaction primarily proceeded along the $[\bar{1}10]$ direction, as judged from scanning AES measurements. It must be noted that the lateral resolution of the scanning AES was only 0.2 mm, and hence the apparent one-dimensionality of the reaction was rather macroscopic and may be strongly influenced by a possible miscut of the sample and the resulting step distribution. The reaction rate was found to depend strongly on the sulfur coverage, and was relatively fast at coverages below approx. 0.28 ML, but slowed down markedly at higher coverages. For the poisoning effect with respect to CO oxidation, the coverage of adsorbed oxygen seemed to be the crucible parameter, leading to a complete suppression of the CO oxidation at sulfur coverages above 0.28 ML. Thus for the oxidation of both S and CO, the oxygen coverage was the rate determining parameter, and the poisoning of sulfur was mainly through a geometric (short-range) site blocking effect.

10 Summary

In the present work, the structure of the clean Ir(110) surface and adsorbate induced reconstructions and deconstructions due to oxygen and sulfur have been investigated using STM, LEED, and AES. The coverage dependent oxygen and sulfur overlayer structures have been characterized by STM for the first time, and a comparison with existing structural models, derived from LEED experiments, was presented. A novel sulfur overlayer structure was found at saturation coverage, for which a structural model was developed. Finally, the O/S coadsorption system has been studied for the first time on an atomic scale. In the following, the results for each of the systems will be briefly summarized.

The clean Ir(110) surface The clean Ir(110) surface exhibits a mesoscopic "rippling" due to alternating, extended (331) and ($33\bar{1}$) facets (chapter 6.2). The facets are terminated by two close-packed rows forming a small (1×1) "terrace" on top of the resulting ridges, which have an average width of approximately 40 Å. The STM topographs are in good agreement with the model proposed by Koch *et al.* [87]. Compared to their work, the quality of the STM topographs could be significantly enhanced, and atomic resolution on the Ir(110) surface was achieved for the first time. Taking into account the He-atom diffraction studies by Avrin and Merill, the faceted Ir(110) surface has now been reported by three independent groups, and hence can be regarded as established. Previous LEED experiments by Van Hove and coworkers favored a (1×2) missing-row model as for Pt(110) and Au(110) [84], but this structure seems to be stabilized by impurities in the Ir(110) case. Hetterich *et al.* associated a (1×2) LEED and RHEED pattern with Si impurities [96]. However, if the Si-induced (1×2) pattern is caused by a missing-row reconstruction or by other rearrangements leading to the same superstructure, remains to be explored. As found in the course of this work, a missing-row (1×2) reconstruction is indeed induced by S adsorption (see below).

Several factors that may play a role in the formation of the faceted structure have been discussed. Energetic reasons may be responsible for the preference for (331) facets compared to (111) facets, a reversal of the situation for Pt(110) and Au(110). Stress relaxation is also believed to play a key role, which was proposed as origin for the large-scale hill and valley structures found on Pt(110) [99], which resemble the rippling of Ir(110), but with a much larger wavelength of 1480 Å. Whether or not such a large-scale superstructure is also present on Ir(110), should be addressed by further experiments with an STM capable of much larger scan frames than the one used in the present study. Theoretical investigations are certainly needed to clarify the driving forces of the faceted reconstruction.

The oxygen stabilized Ir(110)-(1×1) and the Ir(110)-c(2×2)-O structure The oxygen induced lifting of the faceted reconstruction could be verified by STM (chapter 7.2). An unreconstructed (1×1) surface has been atomically resolved, in agreement with a previous STM work of Koch *et al.* [100] and an early LEED study by Van Hove and coworkers [122]. It may be mentioned that the LEED study started out with the (impurity stabilized) (1×2) reconstructed surface, whereas in the present study and in the STM work by Koch *et al.* a clean surface with the faceted reconstruction was used. We find no indications of oxide formation under the present experimental conditions, contrary to early reports by Weinberg and coworkers [121]. The reported oxide should exhibit a (1×4) LEED pattern, which has never been observed during the present work, and was suggested to be caused by oxidized Si impurities by Hetterich [125]. It is interesting to note that both oxygen and sulfur lift the faceted reconstruction, but lead to different substrate terminations. Differences in electronegativity of both adsorbates may play a role in this respect (the Pauling electronegativity is 3.44, 2.58, and 2.20 for O, S, and Ir, respectively [145]).

The c(2×2)-O overlayer on the unreconstructed Ir(110) surface has been investigated by STM for the first time. The overlayer unit cell in the STM images is in agreement with a previous LEED study by Van Hove and coworkers [123]. Contrary to theoretical calculations by Lang [50] and Sautet [54], oxygen atoms are imaged as protrusions in the present work. The origin of the reversed contrast is not clear, an oxygen terminated tip may be the most likely explanation. Strong tip-sample interactions are unlikely as origin, since the gap-resistances where high (> 100 MΩ) in the present case.

Ir(110)-p(2×2)-2S The Ir(110)-p(2×2)-2S structure has been investigated by STM for the first time (chapter 8.2). As found in the course of this work, annealing the S-covered surface lifts the faceted reconstruction and leads to a (1×2) missing-row reconstruction of the substrate. A minimum sulfur coverage of 0.15±0.05 ML is necessary to induce the reconstruction. The sulfur atoms are imaged as protrusions by STM, in agreement with theoretical calculations [50, 54]. At low coverage, the S atoms are mobile and no large sulfur domains are found, indicating repulsive S–S interaction. When the coverage approaches 0.5 ML, large domains are formed, with S atoms arranged in zig-zag rows with glide-plane symmetry along the (non-missing) $[\bar{1}10]$ rows. The overlayer is complete at 0.5 ML sulfur coverage, and converts to a c(2×4) structure at higher coverage (see below).

The STM results confirm the model proposed in a previous LEED study [7], with the exception that small relaxations of the sulfur atoms towards the troughs of the missing-row structure could not be verified by STM. Since the improvement of the theory/experiment agreement in the LEED work was only marginal for the relaxed structure (the improvement was well below the accepted limits for significant changes in the Pendry r-factor), it may be of numerical rather than physical origin. These findings demonstrate the capability of STM to obtain quantitative data on the atomic scale.

A further difference between the previous LEED study and the present work is the structure of the surface prior to sulfur adsorption. In this work, a clean surface with (331) facets has been exposed to sulfur, whereas the LEED study started out with a (1×2) missing-row reconstructed surface, possibly stabilized by impurities. In the LEED study it was deemed surprising that the sulfur apparently had little effect on the substrate reconstruction. Judging from the results of the present work, this is not surprising anymore since sulfur indeed *induces* the missing-row reconstruction.

For the sulfur stabilized, (1×2) missing-row reconstructed Ir(110) surface, no mesoscopic step structures like the fish-scale pattern on Pt(110) [108] and Au(110) [98] have been found. Since this structure is mainly caused by the avoidance of (331) faceted steps, the finding that the fish-scale pattern is not formed in the Ir case is consistent with the fact that such steps are indeed frequently observed on Ir(110)-(1×2), contrary to the situation for Au(110) and Pt(110). This seems reasonable, since the clean Ir(110) surface exhibits extended (331) facets, so a preference for (111) step facets on the (1×2) reconstructed surface would have been surprising.

Ir(110)-c(2×4)-6S A structural model for the Ir(110)-c(2×4)-6S structure has been proposed for the fist time (chapter 8.2). The 'building blocks' of the structure are the same zig-zag rows of sulfur atoms that have been found for the p(2×2)-2S structure, but now they are in antiphase leading to a c(2×4) configuration. The structure is stabilized by sulfur dimers in a second adsorbate layer, sitting in on-top sites over sulfur atoms of the first layer. The dimers are separated by four nearest neighbor distances in [$\bar{1}$10] direction, leading to diffuse streaks halfway between the half-order beams in the LEED pattern along the [$\bar{1}$10] azimuth. Due to the on-top adsorption site, the sulfur dimers exhibit no long-range order in the perpendicular [001] direction across the substrate rows, which explains the streakiness of the extra spots in the LEED pattern. At saturation, the dimers in the second layer contribute 0.25 ML to the coverage, resulting in a saturation coverage of 0.75 ML for the c(2×4)-6S structure. Upon heating the surface above 1000 K for several minutes, the sulfur dimers gradually desorb, and the remaining sulfur overlayer converts back to the p(2×2)-2S structure, which is stable to at least 1100 K, the maximum achievable annealing temperature in our system.

The LEED pattern of the Ir(110)-c(2×4)-6S structure has been reported previously [134], but without proposing a structural model or assigning a coverage. The same LEED pattern (including the additional streaks) was observed previously for the sulfur saturated Pt(110) surface [158, 157]. Again no structural model was proposed in these early studies, but the saturation coverage was determined to 0.75 ML in both reports. Since the clean Pt(110) surface is also (1×2) missing-row reconstructed as the sulfurized Ir(110) surface, it is suggested, based on the LEED pattern and the total coverage, that the saturation structure of sulfur on this surface is essentially the same as on Ir(110), on the assumption that sulfur does not lift the missing-row reconstruction of the Pt substrate. This should be addressed by future research.

An interesting question that could not be conclusively answered in the present work is the detailed conversion mechanism between the p(2×2)-2S and the c(2×4)-6S structure. Every other zig-zag row has to rearrange to form the c(2×4) configuration. In which way this rearrangement is accomplished is not entirely clear at the present stage. Investigation of small local c(2×4) domains formed at a coverage slightly larger than 0.5 ML suggest a shift of the sulfur atoms in $[\bar{1}10]$ direction by a nearest neighbor distance. A possible second conversion mechanism, a 'flip' around the substrate rows with sulfur atoms crossing the ridges of these rows, seems unlikely on the basis of the present results. However, other mechanisms may be possible that involve complex intermediate situations, possibly involving second layer sulfur for stabilization. To observe a conversion *directly* is a very difficult task, which may only be achieved by high-speed STMs capable of atomic resolution at a scan speed of several frames per second (such STMs are not commercially available and only very few of those machines exist worldwide). But even then it is not clear if such a conversion can be tracked at all, since atomic processes usually occur on much shorter time scales. Field ion microscopy may be a second possibility to observe such atomic rearrangements *in situ*, although this method is limited to very small terraces and long-range or many-body effects may be altered on such small planes.

Coadsorption and reaction of O and S on Ir(110)-(1×2) The coadsorption of oxygen on a sulfur precovered, (1×2) missing-row reconstructed Ir(110) surface has been investigated for the first time (chapter 9). At a sulfur coverage below 0.5 ML, low exposures of O_2 lead to a phase separation between the adsorbates (competitive adsorption) due to short-range repulsive interactions. The sulfur atoms coalesce to form p(2×2)-2S domains with the known zig-zag rows, whereas the oxygen atoms adopt a p(2×2)-O structure with no glide plane. The oxygen adsorption site could be identified as the short-bridge site, judging from the registry between adjacent oxygen and sulfur domains in atomically resolved STM images. Hence, the oxygen site is the same as for the Ir(110)-c(2×2)-O structure on the unreconstructed surface. The p(2×2) LEED pattern after oxygen adsorption on the (1×2) reconstructed Ir(110) surface was previously reported in two LEED studies [2, 121], and Weinberg and coworkers proposed a qualitative model on the basis of the LEED pattern and a suggested short-bridge adsorption site [121], in agreement with the present observations. However, no quantitative structural investigation of the p(2×2)-O phase was previously available.

After high O_2 exposures, the phase separation between the oxygen and sulfur domains is lost and a mixed phase with no long-range order develops. Oxygen is compressed into a high-coverage (1×2) structure, and the sum of the repulsive O–O and S–S interaction energies becomes comparable to twice the O–S interaction energy, leading to a mixing of the adsorbate phases. However, the adsorption is still competitive in the sense that no long-range superstructure involving both O and S develops. From the coadsorption experiments it can be concluded that sulfur poisons the surface with respect to oxygen adsorption, and that the poisoning effect is of geometrical nature (site blocking) in the investigated coverage ranges.

Heating the surface to 600 K after coadsorption of O and S leads to a reduction of the S coverage, probably due to sulfur oxidation. An identification of the reaction products was not possible in the present work, since flash-desorption spectra could not be acquired. In analogy to previous reports on the reaction between O and adsorbed S on other metal surfaces (see section 8.3), the formation of SO_2 is suggested.

The reaction seems to proceed only for high oxygen coverage, i.e., when the adsorbed oxygen is in the (1×2) phase. Due to the larger O–O repulsion for this phase, it may be regarded as a kind of activated 'precursor' state for the sulfur oxidation. At low oxygen coverage [with oxygen in the p(2×2) phase] the annealing does not result in a significant loss of sulfur, not even after repeating the adsorption/annealing cycle several times. Since the O and S domains are separated at low O coverage (see above), the reaction would be limited to the domain boundaries, and hence may have been undetectable by the present experiments. Further research should clarify whether or not sulfur oxidation occurs also for the low-coverage oxygen phase.

The previous statements referred to sulfur coverages below 0.5 ML. At or near the saturation coverage of 0.75 ML [Ir(110)-c(2×4)-6S structure], the surface seems to be completely poisoned with respect to oxygen adsorption, according to AES. Exposure to O_2 at room temperature has little effect on the c(2×4)-6S structure, and even exposure to air at ambient pressures leaves the structure basically unchanged. However, annealing the sulfur saturated surface at 470 K in an O_2 atmosphere (total pressure approx 10^{-8} mbar) results in sulfur reduction, presumably due to SO_2 formation, as mentioned above. The LEED pattern during the oxidation process changes from the initial c(2×4) structure of the sulfur saturated surface to a p(2×2) structure near 0.5 ML S coverage, changing further to (1×2) at low S coverage, and finally the substrate reconstruction is lifted due to the oxygen and a c(2×2)-O overlayer remains.

At the present stage it is not clear if the reaction (for high sulfur coverage) involves chemisorbed or physisorbed oxygen. If chemisorbed oxygen is needed, the reaction would be limited to defects in the sulfur overlayer (since oxygen does not chemisorb on the sulfur patches according to AES), and the reaction rate would depend on the defect density. However, STM images taken at the different stages corresponding to the observed LEED pattern (after the reaction had been stopped and the sample had cooled to room temperature) reveal that only very few defects are found as long as the sulfur coverage is 0.5 ML or above. That means, in the initial stage the oxidation apparently does *not* proceed via the growth of oxygen covered vacancies in the sulfur overlayer, provided that the room temperature STM images are representative for the surface under reaction conditions. Instead, the sulfur dimers are oxidized first, and those parts of the sulfur overlayer on which the dimers are reacted off, convert to the p(2×2)-2S structure. At the same time islands are formed that exhibit the same p(2×2)-2S structure as the terraces. The registry and height of the islands indicate that they are (1×2) missing-row reconstructed Ir islands, covered by S in the p(2×2)-2S structure. So far it is not clear where the Ir atoms needed to form the islands originate. A *direct* observation under reaction conditions would provide better insight into the processes, an experiment that is not possible with the STM used in this work.

For a sulfur coverage below 0.5 ML, the reaction should proceed in the same manner as described above, via the reaction of chemisorbed oxygen and sulfur. Increasing parts of the surface are covered by oxygen, which then convert to the bulk truncated (1×1) structure with a c(2×2)-O overlayer.

The manifold changes in overlayer and substrate structure involved in the adsorption, coadsorption, and reaction of O and S on the Ir(110) surface illustrate the complexity even of such 'simple' model systems. As shown in the present work, STM can provide valuable information on the atomic scale, and hence can shed some light on the elementary steps involved in such processes.

Bibliography

[1] F. Besenbacher, I. Chorkendorff, B. S. Clausen, B. Hammer, A. M. Molenbroek, J. K. Nørskov, and I. Stensgaard.
Design of a surface alloy catalyst for steam reforming.
Science, 279:1913, 1998.

[2] K. Christmann and G. Ertl.
Interaction of CO and O_2 with Ir(110) surfaces.
Zeitschrift für Naturforschung, 28a:1144, 1973.

[3] J. L. Taylor, D. E. Ibbotson, and W. H. Weinberg.
A transient study of the CO-adsorption and reaction of CO and oxygen on Ir(110).
Surf. Sci., 90:37, 1979.

[4] U. Burghaus, J. Ding, and W. H. Weinberg.
Carbon monoxide oxidation on Ir(110).
J. of Vac. Sci. and Technol. A, 16:1010, 1998.

[5] J. A. Rodriguez and D. W. Goodman.
High-pressure catalytic reactions over single-crystal metal surfaces.
Surf. Sci. Rep., 14:1, 1991.

[6] M. P. Kiskinova.
Electronegative additives and poisoning in catalysis.
Surf. Sci. Rep., 8:359, 1988.

[7] C.-M. Chan and M. A. Van Hove.
The structure of a (2×2) sulfur overlayer on the Ir(110)-(1×2) reconstructed surface.
Surf. Sci., 183:303, 1987.

[8] Omicron Vakuumphysik, Taunusstein, Germany.
Instruction manual UHV STM lab, 0.2 edition.

[9] C. Röthig.
Untersuchungen zur Struktur und Dynamik von Silizium(111)- und Gold(110)-Oberflächen.
PhD thesis, Universität Osnabrück, 1995.

[10] S. Speller.
Die Struktur von Metall-Einkristall-Oberflächen auf atomarer Ebene- eine Untersuchung mit Rastertunnelmikroskopie an den Beispielen Au und Pb.
PhD thesis, Universität Osnabrück, 1995.

[11] T. Rauch.
Schwefelinduzierte Strukturen auf der Palladium (111)-Oberfläche nach Segregation bzw. Adsorption von Schwefel.
PhD thesis, Universität Osnabrück, March 1999.

[12] Omicron Vakuumphysik, Taunusstein, Germany.
Getting started with Omicron UHV STM, 1.0 edition.

[13] Omicron Vakuumphysik, Taunusstein, Germany.
Spectaleed Optics and Electron Gun User's Guide, 3.3 edition.

[14] STAIB Instruments, D-85354 Freising, Germany.
Instruction manual (rheed electron source), 4.4.1 edition.

[15] Perkin Elmer, Physical Electronics Division, Eden Prairie, MN 55344, USA.
Instruction Manual (Model 10-360 Precision Energy Analyzer), 4.4.3 edition.

[16] H. P. Bonzel, A. M. Franken, and G. Pirug.
The segregation and oxidation of silicon on Pt(111).
Surf. Sci., 104:625, 1981.

[17] H. Niehus and G. Comsa.
Bulk dissolved Si as a cause of the "oxide" formation on Pt(111) surfaces.
Surf. Sci., 102:L14, 1981.

[18] M. Mundschau and R. Vanselow.
Difficulties in the detection of surface impurities on platinum using Auger electron spectroscopy.
Surf. Sci., 157:87, 1985.

[19] T. Michely and G. Comsa.
Temperature dependence of the sputtering morphology of Pt(111).
Surf. Sci., 256:217, 1991.

[20] L. C. Feldman and J. W. Mayer.
Fundamentals of surface and thin film analysis.
North-Holland, 1986.

[21] W. Eckstein, C. García-Rosales, J. Roth, and W. Ottenberger.
Sputtering Data.
Max-Planck-Institut für Plasmaphysik, Garching bei München, 1993.

[22] R. G. Musket, W. McLean, C. A. Colmenares, D. M. Makowiecki, and W. J. Siekhaus. Preparation of atomically clean surfaces of selected elements: A review. *Applications of Surface Science*, 10:143, 1982.

[23] C. Cohen-Tannoudji, B. Diu, and F. Laloë. *Quantum Mechanics.* Hermann, Paris, and John Wiley & Sons, New York, 1977.

[24] G. Binnig and H. Rohrer. Scanning tunneling microscopy - from birth to adolescence. *Rev. Mod. Phys.*, 59:615, 1987.

[25] G. Binnig and H. Rohrer. The scanning tunneling microscope. *Sci. Am.*, 253(2):40, 1985.

[26] R. J. Behm, N. Garcia, and H. Rohrer, editors. *Scanning Tunneling Microscopy and Related Methods.* Kluwer Academic Publishers, Dordrecht, The Netherlands, 1990.

[27] R. Wiesendanger and H.-J. Güntherodt, editors. *Scanning Tunneling Microscopy III.* Springer-Verlag, Berlin, 1993.

[28] Sergei N. Magonov and Myung-Hwan Whangbo. *Surface Analysis with STM and AFM.* VCH, Weinheim, 1996.

[29] J. Tersoff and D. R. Hamann. Theory and application for the scanning tunneling microscope. *Phys. Rev. Lett.*, 50:1998, 1983.

[30] J. Tersoff and D. R. Hamann. Theory of the scanning tunneling microscope. *Phys. Rev. B*, 31:805, 1985.

[31] J. Bardeen. Tunneling from a many particle point of view. *Phys. Rev. Lett.*, 6:57, 1961.

[32] N. D. Lang. Theory of single-atom imaging in the scanning tunneling microscope. *Phys. Rev. Lett.*, 56:1164, 1986.

[33] K. Mednick and L. Kleinman. Self-consistent Al(111) film calculations. *Phys. Rev. B*, 22:5768, 1980.

[34] J. Wintterlin, J. Wiechers, H. Brune, T. Gritsch, H. Höfer, and R. J. Behm.
Atomic-resolution imaging of close-packed metal surfaces by scanning tunneling microscopy.
Phys. Rev. Lett., 62:59, 1989.

[35] A. R. H. Clarke, J. B. Pethica, J. A. Nieminen, F. Besenbacher, E. Lægsgaard, and I. Stensgaard.
Quantitative scanning tunneling microscopy at atomic resolution: Influence of forces and tip configuration.
Phys. Rev. Lett., 76:1276, 1996.

[36] C. J. Chen.
Origin of atomic resolution on metal surfaces in scanning tunneling microscopy.
Phys. Rev. Lett., 65:448, 1990.

[37] C. J. Chen.
Effects of m$\neq$0 tip states in scanning tunneling microscopy: The explanations of corrugation reversal.
Phys. Rev. Lett., 69:1656, 1992.

[38] M. Tsukada, K. Kobayashi, N. Isshiki, and H. Kageshima.
Effect of tip atomic and electronic structure on STM/STS.
Surf. Sci., 242:12, 1991.

[39] M. Tsukada, K. Kobayashi, N. Isshiki, and H. Kageshima.
First-principles theory of scanning tunneling microscopy.
Surf. Sci. Rep., 13:265, 1991.

[40] M. Tsukada, T. Schimizu, S. Watanabe, N. Isshiki, and K. Kobayashi.
Theory of scanning tunneling microscopy/spectroscopy for adsorbed surfaces and layer crystal surfaces.
Japan. J. Appl. Phys., 32:1352, 1993.

[41] G. Doyen, D. Drakova, and M. Scheffler.
Green-function theory of scanning tunneling microscopy: Tunnel current and current density for clean metal surfaces.
Phys. Rev. B, 47:9778, 1993.

[42] G. Doyen, D. Drakova, J. V. Barth, R. Schuster, T. Gritsch, R. J. Behm, and G. Ertl.
Scanning-tunneling-microscope imaging of clean and alkali-metal-covered Cu(110) and Au(110) surfaces.
Phys. Rev. B, 48:1738, 1993.

[43] P. Sautet and C. Joachim.
Electronic transmission coefficient fo the single-impurity problem in the scattering-matrix approach.
Phys. Rev. B, 38:12238, 1988.

[44] P. Sautet, J. Dunphy, D. F. Ogletree, and M. Salmeron.
The role of electronic interferences in determining the appearance of STM images: application to the S(2×2)/Re(0001) system.
Surf. Sci., 295:347, 1993.

[45] N. D. Lang.
Apparent barrier height in scanning tunneling microscopy.
Phys. Rev. B, 37:10395, 1988.

[46] R. J. Behm.
Scanning tunneling microscopy: Metal surfaces, adsorption and surface reactions, pages 173–209.
Kluwer Academic Publishers, Dordrecht, The Netherlands, 1990.

[47] F. Besenbacher.
Scanning tunneling microscopy studies of metal surfaces.
Rep. Prog. Phys., 59:1737, 1996.

[48] N. D. Lang.
Vacuum tunneling current from an adsorbed atom.
Phys. Rev. Lett., 55:230, 1985.

[49] N. D. Lang.
Apparent size of an atom in the scanning tunneling microscope as a function of bias.
Phys. Rev. Lett., 58:45, 1987.

[50] N. D. Lang.
Theory of single-atom imaging in the scanning tunneling microscope.
Comments Cond. Mat. Phys., 14:253, 1989.

[51] P. Sautet, J. C. Dunphy, D. F. Ogletree, C. Joachim, and M. Salmeron.
Imaging a p(2×2) layer of sulfur on Re(0001) with the scanning tunneling microscope: an experimental and theoretical study of the effect of adsorption site and tip structure.
Surf. Sci., 315:127, 1994.

[52] J. C. Dunphy, P. Sautet, D. F. Ogletree, and M. Salmeron.
Approach to surface structure determination with the scanning tunneling microscope: Multiple-gap imaging and electron-scattering quantum-chemistry theory.
Phys. Rev. B, 52:11446, 1995.

[53] M.-L. Bocquet and P. Sautet.
STM and chemistry: a qualitative molecular orbital understanding of the image of CO on a Pt surface.
Surf. Sci., 360:128, 1996.

[54] P. Sautet.
Atomic adsorbate identification with the STM: a theoretical approach.
Surf. Sci., 374:406, 1997.

[55] J. Cerdá, M. A. Van Hove, P. Sautet, and M. Salmeron.
The role of surface relaxations in determining the STM images of sulfur adatoms and clusters on Re(0001): theory versus experiment.
Surf. Sci., 409:145, 1998.

[56] I. S. Tilinin, M. K. Rose, J. C. Dunphy, M. Salmeron, and M. A. Van Hove.
Identification of adatoms on metal surfaces by STM: experiment and theory.
Surf. Sci., 418:511, 1998.

[57] M. Ø. Pedersen, M.-L. Bocquet, P. Sautet, E. Lægsgaard, I. Stensgaard, and F. Besenbacher.
CO on Pt(111): binding site assignment from the interplay between measured and calculated STM images.
Chem. Phys. Lett., 299:403, 1999.

[58] H. Brune, J. Wintterlin, R. J. Behm, and G. Ertl.
Surface migration of 'hot' adatoms in the course of dissociative chemisorption of oxygen on Al(111).
Phys. Rev. Lett., 68:624, 1992.

[59] Omicron Vakuumphysik.
Technical Reference Manual STM Control Unit, 1.2 edition.

[60] Omicron Vakuumphysik, Taunusstein, Germany.
The SPM S0 V2.1 Software Manual, 2.1 edition.

[61] G. Piaszenski.
Strukturuntersuchungen an der $Au_3Pd(110)$-Oberfläche.
Master's thesis, Universität Osnabrück, Jan. 1997.

[62] C. J. Davisson and L. H. Germer.
Diffraction of electrons by a crystal of nickel.
Phys. Rev., 30:705, 1927.

[63] L. de Broglie.
The London, Edinburgh, and Dublin Phil. Mag. and J. of Sci., 47:446, 1924.

[64] M. A. Van Hove, W. H. Weinberg, and C.-M. Chan.
Low-Energy Electron Diffraction.
Springer Series in Surface Sciences 6. Springer Verlag, 1986.

[65] J. B. Pendry.
Low energy electron diffraction.
Academic Press, London, 1974.

[66] M. Henzler and W. Göpel.
Oberflächenphysik des Festkörpers.
Verlag B. G. Teubner, Stuttgart, 1994.

[67] M. A. Van Hove, W. Moritz, H. Over, P. J. Rous, A. Wander, A. Barbieri, N. Materer, U. Starke, and G. A. Somorjai.
Automated determination of complex surface structures by LEED.
Surf. Sci. Rep., 19:191, 1993.

[68] J. B. Pendry.
Reliability factors for LEED calculations.
J.Phys.C:Solid St. Phys., 13:937, 1980.

[69] E. A. Wood.
Vocabulary of surface crystallography.
J. Appl. Phys., 35:1306, 1964.

[70] P. Auger.
Sur l'effet photoélectrique composé.
Journ. Phys. Radium, 6:205, 1925.

[71] H. Haken and H. C. Wolf.
Atom- und Quantenphysik.
Springer Verlag, 1990.

[72] L. E. Davis, N. C. MacDonald, P. W. Palmberg, G. E. Riach, and R. E. Weber.
Handbook of Auger Electron Spectroscopy.
Physical Electronics Industries, Eden Prairie, MN, 1976.

[73] C. L. Hedberg, editor.
Handbook of Auger electron spectroscopy.
Physical Electronics, Inc., Eden Prairie, MN, 1995.

[74] A. Savitzky and J.E. Golay.
Smoothing and differentiation of data by simplified least squares procedures.
Analytical Chemistry, 36:1627, 1964.

[75] S. Ichimura and R. Shimizu.
Backscattering correction for quantitative Auger analysis: I. Monte Carlo calculations of backscattering factors for standard materials.
Surf. Sci., 112:386, 1981.

[76] S. Ichimura and R. Shimizu.
Backscattering corrections for quantitative Auger analysis: III. A simple functional representation of electron backscattering factors.
Surf. Sci., 124:L49, 1983.

[77] M. P. Seah and W. A. Dench.
Surf. Interface Anal., 1:2, 1979.

[78] S. Tanuma, C. J. Powell, and D. E. Penn.
Electron inelastic mean free paths in solids at low energies.
J. Electron Spectrosc. Relat. Phen., 52:285, 1990.

[79] C. J. Powell.
The quest for universal curves to describe the surface sensitivity of electron spectroscopies.
J. Electron Spectrosc. Relat. Phen., 47:197, 1988.

[80] S. Tougaard.
Quantitative analysis of the inelastic background in surface electron spectroscopy.
Surf. Interface Anal., 11:453, 1988.

[81] D. Briggs and M. P. Seah, editors.
Practical surface analysis by Auger and X-ray photoelectron spectroscopy.
John Wiley & Sons Ltd., New York, 1983.

[82] S. Tanuma, C. J. Powell, and D. R. Penn.
Calculations of electron inelastic mean free paths for 31 materials.
Surf. Interface Anal., 11:577, 1988.

[83] S. Mróz.
Physical foundations of quantitative Auger analysis.
Prog. in Surf. Sci., 46:377, 1994.

[84] C.-M. Chan and M. A. Van Hove.
Confirmation of the missing-row model with three-layer relaxations for the reconstructed Ir(110)-(1×2) surface.
Surf. Sci., 171:226, 1986.

[85] W. Hetterich and W. Heiland.
Low energy ion scattering from the Ir(110) surface: a quest for the (1×2) structure.
Surf. Sci., 210:129, 1989.

[86] H. Bu, M. Shi, F. Masson, and J. W. Rabalais.
Reconstruction of the Ir(110) surface: a mixed faceted (1×3) and (1×1) structure.
Surf. Sci. Lett., 230:L140, 1990.

[87] R. Koch, M. Borbonus, O. Haase, and K. H. Rieder.
New aspects on the Ir(110) reconstruction: surface stabilization on mesoscopic scale via (331) facets.
Phys. Rev. Lett., 67:3416, 1991.

[88] W. F. Avrin and R. P. Merrill.
Helium diffraction analysis of the microfaceted Ir(110) surface.
Surf. Sci., 274:231, 1992.

[89] J. Kuntze, S. Speller, and W. Heiland.
The Ir(110) surface studied by STM.
Surf. Sci., 402:764, 1998.

[90] C.-M. Chan and W. H. Weinberg.
Low-energy electron diffraction structural analysis of the (2×2) oxygen overlayer on the iridium (111) surface.
J. Chem. Phys., 71:2788, 1979.

[91] C.-M. Chan, M. A. Van Hove, W. H. Weinberg, and E. D. Williams.
Structural study of the reconstructed Ir(110)-(1×2) surface by low-energy electron diffraction.
Solid State Commun., 30:47, 1979.

[92] C.-M. Chan, M. A. Van Hove, W. H. Weinberg, and E. D. Williams.
An r-factor analysis of several models of the reconstructed Ir(110)-(1×2) surface.
Surf. Sci., 91:440, 1980.

[93] P. Fery, W. Moritz, and D. Wolf.
Structure determination of the (1×2) and (1×3) reconstruction of Pt(110) by low-energy electron diffraction.
Phys. Rev. B, 38:7275, 1988.

[94] W. Moritz and D. Wolf.
Multilayer distortions in the reconstructed (110) surface of Au.
Surf. Sci., 163:L655, 1985.

[95] H. Bu, M. Shi, and J. W. Rabalais.
Coexisting (1×3) and (1×1) structures in the O_2 induced phase change of Ir(110).
Surf. Sci., 236:135, 1990.

[96] W. Hetterich, U. Korte, G. Meyer-Ehmsen, and W. Heiland.
A contribution to the (1×n) reconstructions of the Ir(110) surface.
Surf. Sci. Lett., 254:L487, 1991.

[97] D. A. King and D. P. Woodruff, editors.
Adsorbate induced reconstruction of fcc(110) surfaces (by C. J. Barnes), chapter 13.
The chemical physics of solid surfaces (vol. 7). Elsevier, Amsterdam, 1994.

[98] J. K. Gimzewski, R. Berndt, and R. R. Schlittler.
Scanning-tunneling-microscope study of antiphase domain boundaries, dislocations, and local mass transport on Au(110) surfaces.
Phys. Rev. B, 45:6844, 1992.

[99] P. Hanesch and E. Bertel.
Mesoscopic Self-Organization by Intrinsic Surface Stess on Pt(110).
Phys. Rev. Lett., 79:1523, 1997.

[100] R. Koch, M. Borbonus, O. Haase, and K. H. Rieder.
Reconstruction behaviour of fcc(110) transition metal surfaces and their vicinals.
Appl. Phys. A, 55:417, 1992.

[101] L. D. Roelofs, S. M. Foiles, M. S. Daw, and M. I. Baskes.
The (1×2) missing-row phase of Au(110): Energetics determined from an extended embedded atom method.
Surf. Sci., 234:63, 1990.

[102] S. M. Foiles.
Reconstruction of fcc(110) surfaces.
Surf. Sci., 191:L779, 1987.

[103] M. Stock, J. Risse, U. Korte, and G. Meyer-Ehmsen.
RHEED study of (1×n) reconstructions of the Pt(110) surface.
Surf. Sci., 233:L243, 1990.

[104] T. Gritsch, D. Coulman, R. J. Behm, and G. Ertl.
A scanning tunneling microscopy investigation of the structure of the Pt(110) and Au(110) surfaces.
Surf. Sci., 257:297, 1991.

[105] I. K. Robinson, P. J. Eng, C. Romainczyk, and K. Kern.
X-ray determination of the (1×3) reconstruction of Pt(110).
Phys. Rev. B, 47:10700, 1993.

[106] J. V. Barth, R. Schuster, J. Wintterlin, R. J. Behm, and G. Ertl.
Scanning-tunneling-microscopy observation of k-induced reconstructions on Au(110).
Phys. Rev. B, 51:4402, 1995.

[107] I. Vilfan.
Step patterns on vicinal reconstructed surfaces.
Surf. Sci., 350:329, 1996.

[108] S. Speller, J. Kuntze, T. Rauch, J. Bömermann, M. Huck, M. Aschoff, and W. Heiland.
The (1×2) and (1×4) structure on clean Pt(110) studied by STM, AES and LEED.
Surf. Sci., 366:251, 1996.

[109] J. Kuntze.
Rastertunnelmikroskopie und Elektronenbeugung an den (110)-Oberflächen von Platin und Iridium.
Master's thesis, Universität Osnabrück, Feb. 1996.

[110] J. Tersoff.
Surface stress and self-organization of steps, comment.
Phys. Rev. Lett., 80:2018, 1998.

[111] E. Bertel, K. Swamy, and P. Hanesch.
Reply on 'surface stress and self-organization of steps' by J. Tersoff.
Phys. Rev. Lett., 80:2019, 1998.

[112] K. Swamy, E. Bertel, and I. Vilfan.
Step interaction and relaxation at steps: Pt(110).
Surf. Sci., 425:L369, 1999.

[113] V. Fiorentini, M. Methfessel, and M. Scheffler.
Reconstruction mechanism of fcc transition metal (001) surfaces.
Phys. Rev. Lett., 71:1051, 1993.

[114] C. E. Bach, M. Giesen, and H. Ibach.
Stress relief in reconstruction.
Phys. Rev. Lett., 78:4225, 1997.

[115] D. Wolf.
Should all surfaces be reconstructed?
Phys. Rev. Lett., 70:627, 1993.

[116] B. W. Dodson.
Many-body surface strain and surface reconstruction in fcc transition metals.
Phys. Rev. Lett., 60:2288, 1988.

[117] R. J. Needs, M. J. Godfrey, and M. Mansfield.
Theory of surface stress and surface reconstructions.
Surf. Sci., 242:215, 1991.

[118] A. Filippetti and V. Fiorentini.
Reconstructions of Ir(110) and (100): an ab initio study.
Surf. Sci., 377/379:112, 1997.

[119] H. Ibach.
The role of surface stress in reconstruction, epitaxial growth and stabilization of mesoscopic structures.
Surf. Sci. Rep., 29:193, 1997.

[120] S. Müller, A. Kinne, M. Kottcke, R. Metzler, P. Bayer, L. Hammer, and K. Heinz.
In-plane lattice reconstruction of Cu(100).
Phys. Rev. Lett., 75:2859, 1995.

[121] J. L. Taylor and W. H. Weinberg.
The cemisorption of oxygen on the (110) surface of iridium.
Surf. Sci., 79:349, 1979.

[122] C.-M. Chan, S. L. Cunningham, K. L. Luke, W. H. Weinberg, and S. P. Withrow.
Determination of the atomic arrangement of the unreconstructed Ir(110) surface by low-energy electron diffraction.
Surf. Sci., 78:15, 1978.

[123] C.-M. Chan, K. L. Luke, M. A. Van Hove, W. H. Weinberg, and S. P. Withrow.
The structure of the c(2×2) oxygen overlayer on the unreconstructed (110) surface of iridium.
Surf. Sci., 78:386, 1978.

[124] H. Bu, M. Shi, and J. W. Rabalais.
Surface periodicity of Ir(110) from time-of-flight scattering and recoiling spectrometry (TOF-SARS).
Surf. Sci., 244:96, 1991.

[125] W. Hetterich.
Struktur und Strukturumwandlungen der Ir(110)-Oberfläche.
PhD thesis, Universität Osnabrück, 1991.

[126] W. Hetterich, C. Höfner, and W. Heiland.
An ion scattering study of the surface structure and thermal vibrations on Ir(110).
Surf. Sci., 251/252:731, 1991.

[127] D. I. Hagen, B. E. Nieuwenhuys, G. Rovida, and G. A. Somorjai.
Low-energy electron diffraction, Auger electron spectroscopy, and thermal desorption studies of chemisorbed CO and O_2 on the (111) and stepped [6(111)×(100)] iridium surfaces.
Surf. Sci., 57:632, 1976.

[128] M. Peuckert.
XPS study on thermally and electrochemically prepared oxidic adlayers on iridium.
Surf. Sci., 144:451, 1984.

[129] F. Besenbacher and J. K. Nørskov.
Oxygen chemisorption on metal surfaces: general trends for Cu, Ni and Ag.
Prog. in Surf. Sci., 44:5, 1993.

[130] L. Ruan, F. Besenbacher, I. Stensgaard, and E. Lægsgaard.
Atom resolved discrimination of chemically different elements on metal surfaces.
Phys. Rev. Lett., 70:4079, 1993.

[131] G. A. Somorjai and M. A. Van Hove.
Adsorbate-induced restructuring of surfaces.
Prog. in Surf. Sci., 30:201, 1989.

[132] U. Starke, M. A. Van Hove, and G. A. Somorjai.
Adsorbate-induced relaxations of close-packed fcc and hcp metal surfaces.
Prog. in Surf. Sci., 46:305, 1994.

[133] D. A. King and D. P. Woodruff, editors.
Microscopic studies of adsorbate restructuring at metal surfaces (by F. Besenbacher and I. Stensgaard), chapter 14.
The chemical physics of solid surfaces (vol. 7). Elsevier, Amsterdam, 1994.

[134] E. D. Williams, C.-M. Chan, and W. H. Weinberg.
The adsorption of sulfur on the reconstructed Ir(110)-(1×2) surface.
Surf. Sci., 81:L309, 1979.

[135] C.-M. Chan and W. H. Weinberg.
The structure of the ($\sqrt{3}\times\sqrt{3}$) R30° sulfur overlayer on the iridium (111) surface.
J. Chem. Phys., 71:3988, 1979.

[136] P. Sprunger, F. Besenbacher, I. Stensgaard, and E. Lægsgaard.
STM investigations of CO coadsorption with O and with S on Ni(110).
Surf. Sci., 320:271, 1994.

[137] J. C. Dunphy, B. J. McIntyre, J. Gomez, D. F. Ogletree, G. A. Somorjai, and M. B. Salmeron.
Coadsorbate induced compression of sulfur overlayers on Re(0001) and Pt(111) by CO.
J. Chem. Phys., 100:6092, 1994.

[138] B. J. McIntyre, M. Salmeron, and G. A. Somorjai.
An in situ STM determination of a kinetic pathway for the coadsorbate-induced compression of sulfur by CO on Pt(111).
Surf. Sci., 323:189, 1995.

[139] J. C. Dunphy, P. Sautet, D. F. Ogletree, O. Dabbousi, and M. B. Salmeron.
Scanning-tunneling microscopy study of the diffusion of sulfur on Re(0001).
Phys. Rev. B, 47:2320, 1993.

[140] P. Sprunger, F. Besenbacher, and I. Stensgaard.
STM study of the Ni(110)-(2×1)-2CO system: structure and bonding-site determination.
Surf. Sci., 324:L321, 1995.

[141] C. Park, H. M. Kramer, and E. Bauer.
The chemisorption of sulphur on W(100).
Surf. Sci., 116:467, 1982.

[142] D. R. Mullins, P. F. Lyman, and S. H. Overbury.
Interaction of S with W(001).
Surf. Sci., 277:64, 1992.

[143] M. Salmerón, A. M. Baró, and J. M. Rojo.
Interatomic transitions and relaxation effects in Auger spectra of several gas adsorbates on transition metals.
Phys. Rev. B, 13:4348, 1976.

[144] Binding energy lookup table.
XPS International, http://www.xpsdata.com, 1999.

[145] WebElements: The periodic table on the WWW.
http://www.webelements.com, 1999.

[146] M. A. Van Hove and G. A. Somorjai.
Adsorption and adsorbate-induced restructuring: a LEED perspective.
Surf. Sci., 299/300:487, 1994.

[147] J. Bömermann.
Rastertunnelmikroskopie an einer sauberen und einer mit Schwefel adsorbierten Palladium(111)-Oberfläche.
PhD thesis, Universität Osnabrück, March 1998.

[148] L. Ruan, I. Stensgaard, E. Lægsgaard, and F. Besenbacher.
A scanning tunneling microscopy investigation of the Ni(110)-p(4×1)S phase.
Surf. Sci., 296:275, 1993.

[149] M. Foss, R. Feidenhans'l, M. Nielsen, E. Findeisen, T. Buslaps, R. L. Johnson, F. Besenbacher, and I. Stensgaard.
X-ray diffraction investigation of the sulfur induced 4×1 reconstruction of Ni(110).
Surf. Sci., 296:283, 1993.

[150] K. C. Wong, W. Liu, and K. A. R. Mitchell.
Tensor LEED analysis for the Rh(110)-(3×2)-S surface structure.
Surf. Sci., 344:258, 1995.

[151] M. Perdereau and J. Oudar.
Structure, méchanisme de formation et stabilité de la couche d'adsorption du soufre sur le nickel.
Surf. Sci., 20:80, 1970.

[152] A. Atrei, A. L. Johnson, and D. A. King.
Sulphur adsorption on Cu(110): a SEXAFS study.
Surf. Sci., 254:65, 1991.

[153] R. Baudoing, Y. Gauthier, and Y. Joly.
Chemisorption-induced multilayer relaxation changes: LEED study of Ni(110)-c(2×2)-S.
J. Phys. C: Solid State Phys., 18:4061, 1985.

[154] L. Peralta, Y. Berthier, and M. Huber.
Study of the sulphur adsorption on a palladium (110) surface by LEED and AES.
Surf. Sci., 104:435, 1981.

[155] G. Rovida and F. Pratesi.
Sulfur overlayers on the low-index faces of silver.
Surf. Sci., 104:609, 1981.

[156] K. C. Wong and K. A. R. Mitchell.
Bond length inequalities and relaxations at the Rh(110)-c(2×2)-2S surface structure studied by LEED crystallography.
Surf. Sci., 304:L481, 1994.

[157] Y. Berthier, M. Perdereau, and J. Oudar.
Étude par la diffraction des électrons lents et la spectroscopie Auger de l'adsorption du soufre sur le platine.
Surf. Sci., 36:225, 1973.

[158] H. P. Bonzel and R. Ku.
Adsorbate interactions on a Pt(110) surface. I. Sulfur and carbon monoxide.
J. Chem. Phys., 58:4617, 1973.

[159] J. Wintterlin, S. Völkening, T. V. W. Janssens, T. Zambelli, and G. Ertl.
Atomic and macroscopic reaction rates of a surfac-catalyzed reaction.
Science, 278:1931, 1997.

[160] P. W. Murray, F. Besenbacher, and I. Stensgaard.
Reactions on single-crystal metal surfaces studied with scanning tunneling microscopy.
Israel J. of Chem., 36:25, 1996.

[161] M. S. Hoogeman, M. A. J. Klik, R. van Gastel, and J. W. M. Frenken.
On the smoothing of rough surfaces.
J. Phys.: Condens. Matter, 11:4349, 1999.

[162] K. Christmann.
Introduction to Surface Physical Chemistry.
Steinkopff, Darmstadt and Springer, New York, 1991.

[163] H. P. Bonzel.
Auger electron spectroscopy study of a sulfur-oxygen surface reaction on a Cu(110) crystal.
Surf. Sci., 27:387, 1971.

[164] R. Riwan.
La diffusion du soufre vers la face (110) du nickel.
Surf. Sci., 27:267, 1971.

[165] P. H. Holloway and J. B. Hudson.
The kinetics of the reaction between oxygen and sulfur on a Ni(111) surface.
Surf. Sci., 33:56, 1972.

[166] St. Astegger and E. Bechthold.
Adsorption of sulfur dioxide and the interaction of coadsorbed oxygen and sulfur on Pt(111).
Surf. Sci., 122:491, 1982.

[167] H. P. Bonzel and R. Ku.
Adsorbate interactions on a Pt(110) surface. II. Effect of sulfur on the catalytic CO oxidation.
J. Chem. Phys., 59:1641, 1973.

[168] G. E. Mitchell, M. A. Schulz, and J. M. White.
The reaction of H_2S with adsorbed oxygen atoms on platinum (111).
Surf. Sci., 197:379, 1988.

[169] L. Ruan, F. Besenbacher, I. Stensgaard, and E. Lægsgaard.
Atom-resolved studies of the reaction between H_2S and O on Ni(110).
Phys. Rev. Lett., 69:3523, 1992.

Acknowledgement

This work was performed in the surface science group of the Fachbereich Physik at the Universität Osnabrück.

Thanks are due to

Prof.Dr.W.Heiland for providing the subject of this thesis, for numerous helpful discussions, and for his efforts to find ever new fundings allowing me to visit several conferences, workshops, and the group of Prof. Bardi at the Universitá di Firenze (Italy).

Prof.Dr.U.Bardi for the outstanding hospitality during my several stays in Firenze, his humour and precious advice in preparing publications.

Dr.S.Speller for countless discussions, for critical reading of all manuscripts and her advice on STM, in particular.

Dr.A.Atrei for teaching me the 'art and science' of LEED and his patience to endure (and answer!) my never ending questions.

Dr.M.Aschoff for many discussions concerning our measurements on alloys, and for his special way of closing the lab door.

Dipl.Phys.A.Bachmann for leaving this door open...

Dipl.Phys.M.Hoheisel for the 'manpower' during measurements and especially during maintenance work.

Dr.T.Rauch for providing the most sophisticated STM software ever written.

Dipl.Phys.M.Dirska for answering all Unix questions and for his assistance in printing.

Dr.M.Schleberger for the critical reading of this manuscript.

Dr.I.Spolveri and B.Cortigiani for their assistance during the measurements in Firenze, and for showing me around the countryside.

All present and former members of the group for the good working atmosphere.

The workshop of precision mechanics (especially J.Guth) and the workshop of electronics of the Universität Osnabrück.

And, of course, my wife Sabine for her encouragement and assistance.